HYDRAULIC PERFORMANCE OF LEAKY BARRIERS FOR WATER RESOURCE MANAGEMENT AND CLIMATE CHANGE ADAPTATION USING NATURE-BASED SOLUTIONS

Karthikeyan Murugesan

A thesis submitted in fulfillment of the requirements for the

Degree of Master of Engineering

Main supervisor: Dr Masaya Yoshikai

School of Engineering

The University of Waikato

New Zealand

2026

ABSTRACT

Flooding is one of the most significant natural hazards affecting river systems and urban catchments worldwide, and its impacts are expected to intensify under future climate change conditions. Nature-Based Solutions (NbS), including engineered log jams and leaky barriers, are increasingly being investigated as sustainable alternatives to conventional hard-engineering flood management. These structures have the potential to attenuate flood peaks, increase upstream water storage, and improve ecological resilience while reducing reliance on traditional grey infrastructure.

This research investigated the hydraulic performance of channel-spanning leaky barriers through HEC-RAS 1D steady-state modelling, an energy-slope validation method, and laboratory flume experiments across six barrier configurations at the University of Waikato. Calibration against 46 runs drawn from three published datasets (Muhawenimana et al., 2021; Huang et al., 2022; Schalko, 2018/2019) showed that barrier-induced resistance, rather than bed friction, dominates the hydraulic response of channel-spanning leaky barriers, with calibrated Manning's n values of 0.086–1.426. A backwater rise prediction framework, extended with an effective solid volume fraction correction for barriers with a clear bed gap, achieved a combined Nash–Sutcliffe Efficiency (NSE) of 0.932 across 308 observations from four datasets; the correction proved essential, recovering NSE for the two gapped datasets from strongly negative values to above 0.87.

A piecewise predictive equation for Manning's n was then developed from laboratory observations, expressing n as a power-law function of upstream depth and a cumulative array parameter (CA) for unsubmerged flow, and as a power-law decay from a maximum value with increasing submergence once the barrier is overtopped. The unsubmerged equation achieved an NSE of 0.853 and a mean absolute percentage error of 7.49%, using only geometric and hydraulic parameters known prior to a flood event.

The research demonstrates that this relationship may be incorporated directly into HEC-RAS 1D through an iterative coupling with the backwater rise model, and sets out a physically consistent pathway, proposed but not yet directly tested, for incorporating the same relationship into two-dimensional and catchment-scale morphodynamic frameworks such as CAESAR-Lisflood. The outcomes of this research contribute to sustainable flood management practice and strengthen the evidence base for Nature-Based Solutions in climate change adaptation.

Keywords: Leaky barriers, Nature-Based Solutions, flood attenuation, Manning's roughness, backwater rise, HEC-RAS, engineered log jams, natural flood management.

PREFACE

This thesis is presented to the University of Waikato, New Zealand, in completion of the criteria for obtaining the Master's Degree in Civil Engineering. The research presented in this thesis has not been formerly submitted for a degree or diploma at any other institution of higher learning. To the best of my knowledge and belief, the thesis does not include any significant material that has been published or authored by someone else, unless appropriate acknowledgment is provided.

ACKNOWLEDGEMENTS

First and foremost, I would like to express my sincere gratitude to my principal supervisor, Dr. Masaya Yoshikai, for his invaluable guidance, patience, and continuous support throughout this research. His expertise in hydraulic modelling and constructive feedback at every stage of this work greatly contributed to the quality of this thesis.

I would also like to thank Dr. Deonie Castle, for her thoughtful suggestions and encouragement during the research process. Her broader perspective on Nature-Based Solutions and sustainable water management significantly enriched the direction and depth of this study.

My sincere appreciation is extended to the School of Engineering, University of Waikato, for providing access to the laboratory facilities and technical resources required for the experimental investigations.

I am especially grateful to the technical officers and laboratory staff who contributed to the success of the experimental programme. Special thanks are due to Sam Knox for his expert assistance with laser engraving and precision hole cutting; to Daniel Crowther for his guidance and steady support throughout the flume experiments; and to Cole Dawson for his help with material procurement and laboratory logistics. Their technical expertise and willingness to assist were indispensable throughout the study.

I would also like to thank my colleagues and friends — particularly Gopika and Amir Auckaili — who assisted during the laboratory experiment phases. Their enthusiasm and encouragement made a meaningful difference at every stage of this journey.

Finally, I would like to express my deepest gratitude to my family for their unconditional love, patience, and unwavering motivation during my studies in New Zealand. This thesis is dedicated to them.

NOTATIONS AND ABBREVIATIONS

NbS— Nature-Based Solutions

ELJ— Engineered Log Jam

Q— Discharge (m^3/s)

q— Unit discharge (m^2/s)

B— Channel width (m)

H_1— Upstream water depth (m)

H_2— Downstream water depth (m)

H_0— Unobstructed (normal) flow depth (m)

H_4— Downstream water depth at measurement station (m)

H_s— Barrier height (m)

b_0— Lower-gap height (m)

L_s— Longitudinal barrier length (m)

ΔH— Backwater rise, $H_1 - H_0$ (m)

n— Effective Manning's roughness coefficient ($m^{-1/3}s$)

n_0— Baseline channel Manning's roughness coefficient ($m^{-1/3}s$)

Fr— Froude number

Sf— Friction slope

S_0— Channel bed slope

ϕ— Barrier porosity

af— Frontal area density (m^{-1})

CA— Cumulative array parameter (m^{-1})/Accumulation Factor

V— Mean flow velocity (m/s)

g— Gravitational acceleration (9.81 m/s^2)

R— Hydraulic radius (m)

A— Flow cross-sectional area (m²)

NSE— Nash–Sutcliffe Efficiency

RMSE— Root Mean Square Error

MAPE— Mean Absolute Percentage Error

HEC-RAS— Hydrologic Engineering Center River Analysis System

SWAT— Soil and Water Assessment Tool

DEM— Digital Elevation Model

1D / 2D— One-dimensional / Two-dimensional (hydraulic model)

CAESAR-Lisflood— Catchment-scale morphodynamic and flood routing model

NLJ— Natural Log Jam

LW— Large Wood (naturally forming woody debris)

d— Log or dowel diameter (m)

b— Inter-log gap spacing (m)

W— Barrier plate length used in energy slope calculation (m)

$H_{3,min}$— Minimum critical depth through the barrier (m)

φ (phi) — Solid volume fraction (dimensionless)

a_k— Configuration-specific calibration coefficient (dimensionless)

n_H— Manning's n obtained from HecRAS model(s/m$^{1/3}$)

nmax— Maximum Manning's n at the submergence transition point (s/m$^{1/3}$)

Re— Reynolds number (dimensionless)

FM%— Fine material percentage in large wood accumulations (Schalko et al., 2018)

TABLE OF CONTENTS

LIST OF FIGURES

LIST OF TABLES

CHAPTER 1. INTRODUCTION

1.1 Background

Historically, the traditional methods used for managing the floods includes constructing of physical barriers such as dams, levees, and weirs. Although, these types of structures were successful in preventing flooding in certain locations, they disrupted natural riverine functions, fragmented ecosystems and created larger-than-expected concentrations of flood waters downstream. Moreover, these structural solutions are very expensive to construct and needs ongoing maintenance. These limitations have led to the growing interest in using Nature-Based Solutions (NbS) to manage flood risk while maintaining natural ecosystem functioning.

NbS use natural hydrological and geomorphic processes to mitigate flood risk while creating additional benefits for biodiversity, water quality, carbon sequestration and community resilience. Examples of NbS include restoring wetlands, planting vegetation along streams, reconnecting floodplains, allowing rivers to meander naturally again, placing wood debris in streams, beaver dam analogues and "leaky" barriers. Among all NbS examples leaky barriers and ELJs are particularly interesting due to their potential to slow flow velocities, create temporary water storage upstream, and allow for the attenuation of floods at relevant scales for practical implementation.

A leaky barrier is a partially permeable, longitudinal structure spanning a river channel. It typically consists of a series of stacked logs or dowels placed across the river, spaced in some way to create small gaps for water to pass through. During high flow events the structure will allow water to flow through the spaces between the logs and through the lower opening in the bed of the structure. At low flow rates the barrier may have no impact on flow rate; however, as the flow increases it creates resistance to flow, raises the upstream water level, slows the flow rate and delays the arrival of the flood wave downstream. Due to its temporary storage and attenuation functions leaky barriers have become a fundamental part of natural flood management programs and climate change adaptation plans.

The leaky barriers help in mitigating flood damage through natural means of slowing down flood waves and storing the excess water in the floodplain before releasing it back into the river system, but their hydraulic behaviour is quite complex. Water may flow simultaneously through the pores of the log structure, underneath the lower gap in the bed of the barrier, over the top of the barrier and laterally past sections of un-supported edge. The overall hydraulic response depends on many variables which include discharge volume, channel width, bed slope, pre-flood upstream flow depth, barrier height and length, log diameter and spacing, porosity of logs, frontal area density of logs per unit area of channel bed, lower-gap height and arrangement of logs throughout the structure. Each variable interacts in some way to produce backwater rise upstream, water depth downstream, head loss, velocity redistribution and total hydraulic resistance.

Engineers typically depict the leaky barriers in hydraulic models by using an augmented Manning's roughness coefficient. But, choosing an acceptable value of Manning's roughness coefficient continues to be a difficult task, as the prevailing methods predominantly depends on engineering judgment or post-hoc calibration instead of a physically grounded relationship. This contributes to a significant uncertainty into flood inundation forecasts, particularly when upstream and downstream water levels are indeterminate before a flood event.

To address this void, the current study assesses the hydraulic performance of leaky barriers through numerical simulation, hydraulic analysis, and laboratory flume testing using scale models of wooden dowels and laser-cut side plates. Backwater rise, head loss, and hydraulic resistance were quantified from upstream and downstream water depth measurements. A piecewise Manning's roughness relationship was then developed and validated against the laboratory data and three previously published datasets. Finally, the suitability of this approach for representing leaky barriers in one-dimensional models such as HEC-RAS was evaluated, with potential extension to catchment-scale models such as CAESAR-Lisflood discussed as future work.

1.2 Aim and Objectives

The principal aim of this research is to investigate the hydraulic performance of leaky barriers and to develop a practical method for representing their resistance effects in hydraulic models for flood management and climate change adaptation.

The specific objectives of this research are:

- To investigate the hydraulic behaviour of channel-spanning leaky barriers under controlled laboratory flume conditions.
- To measure upstream and downstream water depths for a range of discharge conditions and leaky barrier configurations.
- To analyse the influence of key barrier geometric parameters — including barrier height, longitudinal length, porosity, frontal area density, and lower-gap height — on backwater rise and flow resistance.
- To evaluate the relationship between leaky barrier hydraulic response and effective Manning's roughness coefficient.
- To develop a practical expression for estimating leaky-barrier-induced Manning's roughness from measurable hydraulic and geometric parameters.

- To compare the derived roughness relationship with experimental data and available datasets from previous studies on engineered leaky barriers and large woody debris jams.
- To assess the suitability of HEC-RAS 1D for representing leaky barrier resistance through modified Manning's n values.
- To explore the potential integration of the derived resistance relationship into broader hydraulic and morphodynamic models such as CAESAR-Lisflood.
- To contribute to the design and implementation of Nature-Based Solutions for sustainable flood mitigation and climate change adaptation.

1.3 Research Gaps

There are numerous recognized NbS (Nature-Based Solutions) for reducing peak flows and attenuating flooding; however, there are also several key limitations with regards to their hydraulic representation and their application in modelling practices. Leaky barriers and engineered logjams are two examples of the most well-recognized types of NbS; however, with respect to the first limitation noted above, there may not be universally accepted design equation that has been established for determining the hydraulic resistance of leaky barriers. While individual studies have examined backwater rise, flow attenuation and hydraulic behaviour in a variety of laboratory and field settings using different combinations of barrier geometry and flow rates, each study was conducted in isolation. Therefore, while some useful hydraulic relationships were developed, they were primarily limited to the experimental conditions tested. Consequently, there is little opportunity for transferring these findings to other river systems with different geometric characteristics and operating conditions.

A second major limitation is the lack of practical guidelines for establishing an effective Manning's roughness coefficient (n) for leaky barriers. Leaky barriers are commonly modelled in HEC-RAS as a localized elevation in Manning's n value. Unfortunately, this method relies on calibration procedures that do not account for the physical processes involved. Therefore, it is difficult to establish a reliable estimate of how a proposed installation will affect water levels in a river system when calibrated measurements of those water levels are not available.

Many of the previous studies referenced in the literature utilized either the downstream water depth or the downstream Froude number as input variables. These are often unknown quantities at the time of running a model. Hence, there is a significant practical need for new equations that express the effect of leaky barriers in terms of parameters which are known or measurable prior to model execution – i.e., discharge, channel

width, bed slope, barrier height, lower gap height, porosity and barrier length.
Finally, the role of lower gap height has received inadequate attention in many previously described leaky barrier models. Lower gaps play a fundamental role in determining discharge partitioning between the porous component and the underflow path. If a model does not properly simulate lower gap hydraulics, then the model output can contain large errors relative to actual barrier performance depending upon the configuration of openings used in the barrier.

Therefore, there is a need to develop new methods that can translate laboratory scale experimental results into forms suitable for use in common engineering modelling software (e.g., HEC-RAS and CAESAR-Lisflood). Ultimately, this requires a consistent relationship that describes observed backwater effects, energy losses and corresponding changes to Manning's n. Improved consistency and accuracy in hydraulic representations should ultimately lead to better predictions of future hydrologic events. This current project addresses all five of the above limitations by providing comprehensive laboratory experiments, hydraulic analyses and evaluations of computational models with the ultimate goal of developing a physically meaningful and practically applicable form of Manning's roughness-based representation for channel spanning leaky barriers.

1.4 Scope of Work

This research focuses mainly on the hydraulic properties as well as the mathematical modelling representations of leaky barriers (as part of nature-based solutions) for flood attenuation. This study includes the integration of experimental laboratory testing, hydraulic data analysis, and interpretations of numerical modelling.

Key Components Include:

Laboratory Flume Investigation: A controlled series of 264 laboratory tests were carried out at a recirculating laboratory flume in order to examine the hydraulic behaviour of leaky barriers at various discharges. Measurements include upstream and downstream water level measurement, change in flow depth and flow resistance resulting from the presence of the barrier.

Preparation of Leaky Barrier Models: Small scale barrier models were built using wooden dowels and laser cut side plates to ascertain that all the barrier models had the same geometry and could be reproduced precisely. Several different barrier model configurations were used to determine backwater rise, head loss, and effective hydraulic resistance.

Manning’s Roughness Coefficient Estimations: The collected hydraulic data, along with established hydraulic principles, were used for the effective estimation of the Manning’s roughness coefficients.

Development of a practical roughness expression: One of the key outcomes of this research is a practical equation that can be used to estimate the leakage-induced flow resistance around a leaky barrier based upon measurable attributes including discharge, channel width, barrier height, gap height below the barrier, porosity, frontal area ratio and length of barrier.

Hydraulic modelling of leaky barriers using HEC-RAS: Hydraulic consequences associated with leaky barriers were modelled using HEC-RAS 1D with modified Manning’s ‘n’ values. Outputs from these simulations were compared with measured hydraulic behaviour to evaluate the accuracy of the methodology adopted to represent roughness.

Application potential for inclusion in catchment-scale modelling: This study also considers how the developed relationships may be integrated into models like CAESAR-Lisflood which would allow for dynamic representation of resistance provided by leaky barriers over time at the catchment scale.

CHAPTER 2. LITERATURE REVIEW

2.1 Introduction

Flooding remains a catastrophic hazard around the globe, causing direct damages of about USD 76 billion in 2020 alone (Zhuang et al., 2025). The frequency and intensity of flood events have increased in many regions due to the combined effects of climate change, rapid urbanisation, deforestation and sustained changes in land use (Munoth & Goyal, 2019; Reddy et al., 2018). Conventional "grey" engineering solutions such as concrete channels, floodwalls and levees modify river dynamics, harm ecological connectivity, and often displace or exacerbate downstream flood risk (Vojinovic et al., 2021; Zhuang et al., 2025).

Nature-Based Solutions (NbS) have emerged as an ecologically adaptive alternative that harnesses natural river processes to mitigate floods (Vojinovic et al., 2021; Webber et al., 2025). Typical methods include wetland creation, floodplain reclamation, riparian restoration, beaver dam analogs, engineered log jams (ELJs) and leaky barriers (Darzikolaei et al., 2024; Muhawenimana et al., 2021; Stout et al., 2016). Leaky barriers and ELJs are especially effective in that they increase in-channel storage, decrease peak flows and are cost-effective, using local organic materials (Huang et al., 2022; Müller et al., 2021; Zhuang et al., 2025).

Leaky barrier hydraulics under different flows have been extensively studied (Altmann et al., 2024; Follett et al., 2021; Follett & Wohl, 2024; Muhawenimana et al., 2021; Schalko et al., 2018). Performance depends on blockage, porosity, gap height, depth, Froude number, geometry, spacing (Follett et al., 2021; Huang et al., 2022; Muhawenimana et al., 2021). However, important gaps exist to represent these barriers in HEC-RAS and CAESAR-Lisflood. In particular, there are no approaches in the frameworks to estimate the Manning roughness coefficients from measurable geometric parameters (Leakey et al., 2020; Wolstenholme et al., 2025; Zhuang et al., 2025).

In this chapter, literature is systematically reviewed on: (2.2) flooding and climate change impacts; (2.3) Nature-Based Solutions for flood management; (2.4) leaky barriers and engineered log jams; (2.5) hydraulic behaviour of leaky barriers; (2.6) hydraulic modelling approaches; and (2.7) research gaps and summary.

2.2 Flooding and Climate Change Impacts

2.2.1 Global Flood Risk and Climate Drivers

Flood risks are amplified globally by climate change and urbanisation, which increase storm intensities and reduce infiltration of soil. [Leakey et al., 2020; Muhawenimana et al., 2021; Webber et al., 2025]. However, traditional grey infrastructure does not have the long-term resilience to cope with these changing hydrological extremes. Hydrodynamic modeling [Vojinovic et al., 2021] demonstrated that small-scale NbS can mitigate the impact of minor storms, but extreme events require a hybrid framework that combines NbS with grey infrastructure. [Vojinovic et al., 2021]. Riverine NbS provide co-benefits such as erosion control and flood attenuation. Uptake of infrastructure is impeded by regulatory barriers and absence of technical standards. [Webber et al., 2025]

2.2.2 Hydrological Modelling of Climate Impacts

Watershed models have the ability to break down the climate effects on stream runoff, but their outputs strongly rely on the quality and resolution of the inputs (Wolstenholme et al., 2025). SWAT reviews over multi-decadal periods show that the model can successfully capture land-use and climate interactions, however, intermittent flows make it difficult to calibrate parameters (Wolstenholme et al., 2025). The results are sensitive to the resolution of the digital elevation model (DEM) as a coarser grid spacing affects the number of sub-basins, surface runoff values and sediment yields (Zhuang et al., 2025). These macroscale frameworks capture broad watershed dynamics but are not hydraulically precise enough to simulate localized backwater pools and cross-sectional drag forces created by in-stream woody barriers (Leakey et al., 2020).

2.3 Nature-Based Solutions for Flood Management

2.3.1 Definition, Principles, and Co-Benefits

Nature-Based Solutions interact with natural geomorphological and hydrological patterns to increase resilience at a systemic level (Webber et al., 2025). They combine natural raw materials with engineered components to decrease peak discharge, reduce runoff velocities, enhance soil infiltration and increase temporary water storage (Altmann et al., 2024; Muhawenimana et al., 2021). Leaky barriers have operational advantages over other designs as they are operational immediately after construction and their discharge paths are easy to design (Altmann et al., 2024). However, the standardized numerical modeling methods for these structures are still vastly under-developed (Leakey et al., 2020).

2.3.2 Leaky Barriers and Woody Structures as NbS

Woody NbS comprise logs, branches or wooden dowels arranged in porous arrays to impede flows and permit baseline water flow (Follett et al., 2021). These structures consist of naturally occurring large woody debris, semi-natural wood dams and engineered log jams built for the specific purpose (Follett & Wohl, 2024). A well-engineered barrier allows baseflows to pass unimpeded under the structure, acting only as a storage device in an emergency when floodwaters rise to the upper log matrix (Follett et al., 2021). Reach-scale modeling shows that leaky dams can reduce peak discharge by up to 31% during 1-in-10-year storms, and dynamic sediment-transport interactions can increase reach storage capacity by an order of magnitude (Leakey et al., 2020).

2.3.3 Beaver Dams as Natural Analogues

Beaver dam hydraulic data can provide fundamental data for the design of engineered leaky barrier systems (Follett & Wohl, 2024). Hydraulic modeling indicates that a series of dams changes the channel profile by increasing depth and width and decreasing average flow velocities (Follett & Wohl, 2024). These changes increase spatial heterogeneity of substrate grain size distributions (Follett & Wohl, 2024). Importantly, even a low frequency of dams per unit length produces significant hydraulic shifts, illustrating that structure spacing and density across a catchment dictate cumulative flood attenuation performance (Follett & Wohl, 2024).

2.4 Leaky Barriers and Engineered Log Jams

2.4.1 Structure, Formation, and Design

Leaky barriers possess open pores and lower gaps that preserve baseline ecological connectivity and sediment passage, unlike solid dams (Follett et al., 2021). Flume experiments on wood-piece transport show that travel distance decreases with increasing log length and decreasing depth, but increases under congested regimes (Huang et al., 2022). Engineered designs are dependent on cross-sectional placement and structural porosity to facilitate sediment movement. To improve equilibrium scour calculations, researchers introduce surface porosity ϕ_s, which is the 2D frontal area blockage, and volumetric porosity ϕ_v, which is the 3D internal void volume (Huang et al., 2022). Scour growth over time results in a saturation growth curve which marks the geomorphic timeline of channel adjustments after installation (Huang et al., 2022).

2.4.2 Backwater Rise and Hydraulic Attenuation

Flood peak attenuation and temporary water storage propagate backwater rise upstream. The experiments of compound channel flume show that the cross-sectional blockage ratio is the main factor for the afflux of the area and head loss and the longitudinal length has little effect (Muhawenimana et al., 2021). Solid barriers provide twice the area afflux than porous designs and the same or more afflux than complicated multi-angled arrangements, provided by consistent log layouts (Muhawenimana et al., 2021). Organic debris that builds up over time reduces the permeability of the barrier and increases the backwater rise. This behaviour is quantified using a design equation mapping approach depth (H0), Froude number (Fr0), compactness (CA) and fine material percentage (FM%) (Schalko et al., 2018)

$$\Delta H/H0 = f(Fr0, CA, FM\%)$$

where ΔH is the backwater rise. Backwater rise can also be predicted as a function of log size, packing density and channel characteristics using analytical models. However, the expressions are more useful in engineering practice by substituting slope and roughness with the Froude number, though the role of porosity on the backwater rise is not yet completely clear (Poppema & Wüthrich, 2024).

2.4.3 Reach-Scale and Catchment-Scale Performance

Field observations of 37 mountain reaches show that effective flow resistance increases with the ratio of upstream jam depth to unjammed depth and with the ratio of backwater length to average jam spacing (Follett & Wohl, 2024). Importantly, randomly distributed jams have a lower effective resistance than uniformly spaced barriers because of backwater truncation from closely spaced structures (Follett & Wohl, 2024).

The implementation of a roughness-based representation of leaky dams in CAESAR-Lisflood at catchment scale shows that the hydraulic performance is most strongly controlled by lower gap size and Manning's roughness (Leakey et al., 2020). Incorporating sediment transport into the barrier hydraulics results in a simulated water storage that is up to ten times greater than the hydraulic-only runs. These findings demonstrate that geomorphic feedbacks increase the storage capacity over time (Leakey et al., 2020).

2.5 Hydraulic Behaviour of Leaky Barriers

2.5.1 Flow Pathways and Flow Partitioning

The hydraulic behaviour of leaky barriers involves four simultaneous pathways, i.e. underflow through a lower gap, through-flow through internal pores, around-flow through bypass channels and overtopping at high flows (Altmann et al., 2024; Follett et al., 2021). Severe turbulence, localized head loss, velocity redistribution and flow contraction are the consequences of the multi-pathway profile (Altmann et al., 2024).

The momentum and continuity equations were used to derive an analytical expression showing that the solid volume fraction (1-porosity) is the main factor controlling the backwater rise upstream (Huang et al., 2022). This momentum-based framework provides a physically interpretable basis for the estimation of manning's roughness coefficients from the structural dimensions (Huang et al., 2022).

2.5.2 Lower-Gap Hydraulics and Discharge Partitioning

The lower gap is used to control discharge splitting, maintain fish passage, and meet river connectivity requirements (Follett et al., 2021). A two-box, momentum-based model treats the porous matrix and the open lower gap as two flow regions (Follett et al., 2021). It uses canopy drag theory for the log matrix and an analogy of a sluice gate to model the loss of momentum in underflow, and shows good agreement with predictions for a range of jam lengths, porosities and discharges (Follett et al., 2021).

Monitoring juvenile rainbow trout (Oncorhynchus mykiss) movements in flume trials suggests that high-blockage barriers create large recirculation zones and an accelerated underflow jet (Altmann et al., 2024). Solid barriers cause more floodplain inundation than porous ones for the same discharges, and upstream fish passage is improved by shorter and non-porous barriers (Altmann et al., 2024).

2.5.3 Porosity, Frontal Area, and Resistance

Increased log jam porosity reduces flow obstruction, equilibrium scour depths, and downstream geomorphic disturbance (Huang et al., 2022). Field monitoring confirms that structural metrics combined with the ratio of backwater length to jam spacing drives effective reach-scale hydraulic resistance across a series of logjams (Follett & Wohl, 2024). Turbulence fields around porous barriers also affect hyporheic exchange (Muhawenimana et al., 2021). Particle image velocimetry and fluorescent dye tracing show that hyporheic flow velocities in channels with log jams are two orders of magnitude higher than in bare channels and that the dimensionless log-jam-induced hyporheic flux increases fivefold with increasing Froude numbers above 0.06 (Muhawenimana et al., 2021).

2.6 Hydraulic Modelling of Leaky Barriers

2.6.1 Overview of Modelling Approaches

Numerical models are required to quantify the influence of leaky barriers on water surface profiles, flood routing and peak attenuation at reach scales. Five major approaches can be used to model these structures: increased Manning's roughness, cross-section changes, porous flow media, stage-discharge rating curves and internal boundary conditions (Leakey et al., 2020; Wolstenholme et al., 2025). The linear barrier networks are simulated with 1D codes, complex overland flow paths are well captured with 2D models, and localised flume dynamics are resolved with 3D codes (Leakey et al., 2020). At present, there is no universal method for representing leaky barriers, and practical roughness-based methods lack physically grounded calibration frameworks (Leakey et al., 2020; Wolstenholme et al., 2025).

2.6.2 Roughness-Based Representation

The most commonly used practical approach is to model leaky barriers as localized zones of increased Manning's roughness (n) in 1D or 2D models. The method, tested in the Soverato River study (Italy; cited by Leakey et al., 2020), reproduces successfully historical flood marks and upstream backwater profiles without intensive grid refinement by treating woody debris clogging as a localized roughness adjustment. Similarly, using roughness-based representations of leaky dams in CAESAR-Lisflood 1.9j, Manning's n and gap size are shown to be the most sensitive parameters controlling hydraulic efficacy (Leakey et al., 2020). However, roughness-based methods do not properly account for low-flow water levels or steep channel behavior, indicating the need for equations that connect Manning's roughness directly to the dimensions of physical barriers (Leakey et al., 2020).

2.6.3 1D Internal Boundary Condition Approach

The second is a physically rigorous 1D approach that uses a Godunov-type finite volume scheme for solving the shallow water equations, and treats the leaky barriers as internal boundary conditions (Zhuang et al., 2025). This approach explicitly simulates the stage-discharge relation at the structure boundary, which can allow for different hydraulic behaviors at low and high flows (Zhuang et al., 2025). The transient simulations indicate the need for the validated mathematical tools (Zhuang et al., 2025) to optimize the barrier array leakiness and spacing. This framework further provides an initial value of the flume roughness of $n0 \approx 0.009$ for smooth laboratory channels, which gives an important reference value for experimental validation (Zhuang et al., 2025).

2.6.4 Two-Dimensional Modelling of Logjams

In the case of 2D hydrodynamic solvers, Altmann et al. (2024) showed that logjams can be simulated accurately by coupling a solid, zero-thickness wall element to induce flow contraction, with a localized roughness modification to account for internal energy dissipation. The method was calibrated with the software Basement v3 for 350 configurations and was able to predict backwater rise for full- and partial-spanning jams within a ±30% error margin (Altmann et al., 2024). The main advantage of this approach is its transferability to standard 2D engines, but these calibrated coefficients are not universal and need to be carefully verified outside their calibration bounds (Altmann et al., 2024). In conclusion, although 1D, 2D and roughness approaches are used for different spatial scales, a roughness-based representation is still the most practical way for 1D reach-scale modeling in HEC-RAS as long as a physically based equation exists to estimate Manning's n from measurable properties.

2.6.5 HEC-RAS and Terrain Representation

HEC-RAS simulates 1D water surface profiles, 2D depth-averaged flow fields, and structural effects. In laboratory flume settings, the grid size and terrain interpolation methods have significant influence on the accuracy of water surface profiles, so it is important to have a high-resolution representation of the terrain, according to the US Army Corps of Engineers – Hydrologic Engineering Center (2023). However, HEC-RAS does not have a specific leaky barrier module. Workarounds such as increasing Manning’s n, inline structures based on weir/orifice curves, or 2D porous media features are used by practitioners (Altmann et al., 2024; Zhuang et al., 2025). None of these methods is universally accepted and the lack of a physically based Manning’s \(n\) estimation method remains a major practical gap.

2.7 Research Summary and Identified Gaps

The literature reviewed shows that leaky barriers and engineered log jams are effective nature-based flood attenuation components (Follett & Wohl, 2024; Muhawenimana et al., 2021; Stout et al., 2016; Wolstenholme et al., 2025; Zhuang et al., 2025) with their hydraulic performance controlled by blockage, porosity, gap height, length, log diameter, and flow conditions (Follett et al., 2021; Huang et al., 2022; Muhawenimana et al., 2021; Schalko et al., 2018). Predictions of backwater rise have been improved by analytical models based on equations involving Froude numbers, compactness and debris content (Schalko et al., 2018), solid volume fractions and drag coefficients (Huang et al., 2022), and two-box momentum balances for discharge partitioning in the lower-gap (Follett et al., 2021) reformulated by Poppema and Wüthrich (2024) based on the Follett et al. (2020) framework to improve their practical applicability.

Nevertheless, these results also show critical gaps, since there is no generally accepted framework to estimate the effective Manning’s roughness from geometric parameters (Leakey et al., 2020; Zhuang et al., 2025), existing equations need unavailable pre-installation inputs (Follett et al., 2021; Huang et al., 2022), lower-gap dynamics are oversimplified (Follett et al., 2021; Wolstenholme et al., 2025), flume studies cannot be directly transferred to the field (Muhawenimana et al., 2021; Schalko et al., 2018), and a validated bridge between laboratory observations and numerical engines such as HEC-RAS and CAESAR-Lisflood is still lacking (Altmann et al., 2024; Wolstenholme et al., 2025). Thus, this work employs systematic flume experiments, hydraulic analyses, and numerical modeling to develop and validate a physically based representation of Manning’s roughness for channel-spanning leaky barriers in HEC-RAS and CAESAR-Lisflood.

CHAPTER 3 MANNING'S n DETERMINATION USING HEC-RAS

3.1 Introduction

HEC-RAS (Hydrologic Engineering Centre – River Analysis System) is a one-dimensional hydraulic modelling program developed by the U.S. Army Corps of Engineers that solves the gradually varied flow equations for a specified channel geometry and roughness. In this study, HEC-RAS 1D steady state hydraulic modelling has been used for the creation of the digital representations of three laboratory flume experiments from the research papers, namely Muhawenimana et al. (2021), Huang et al. (2022), and Schalko et al. (2018, 2019) and to determine the Manning roughness coefficient which when applied over the barrier zone in the HecRAS produces the same upstream water depth H1 as mentioned in the research paper. This calibration based approach considers that the n is the single parameter that represent the cumulative hydraulic resistance offered by the leaky barrier.

The extracted HEC-RAS Manning's *n* values (hereafter n_H) are then compared against values that has been derived from the energy slope method applied to the same datasets, as a means of validating the energy slope approach.

3.2 Research Datasets from Published Literature

Three published experimental datasets were selected as the primary data source for HEC-RAS model development, calibration, and validation. Together they represent engineered leaky barriers (Muhawenimana et al. 2021; Huang et al. 2022) and large woody debris jams (Schalko et al. 2018, 2019), covering a wide range of barrier geometries, channel widths, bed slopes, and hydraulic conditions. Key measured parameters across all datasets include barrier longitudinal length L_s), log diameter d, channel width B, solid volume fraction φ, discharge Q, and upstream and downstream water depths H_1 and H_2. Engineered-barrier-specific parameters — bed gap b_0 and inter-log gap b — were recorded for Muhawenimana and Huang only, as these geometric features are not applicable to naturally forming LW jams.

3.2.1 Muhawenimana et al. (2021)

The Muhawenimana dataset represents one of the most detailed experimental programmes available on laboratory-scale engineered, channel-spanning leaky barriers. Experiments were conducted in a recirculating compound-channel flume at Cardiff University (10 m long, 1.2 m wide, 0.3 m deep) with a symmetrical main channel of width B = 0.6 m flanked by two 0.3 m floodplains and a bed slope S = 0.001. Leaky barriers consisted of wooden dowels of diameter d = 0.025 m rigidly spanning the main channel. Three barrier configurations (Linear, Lattice, Alternating) were tested; only the porous Linear dataset is used here. Barrier heights H_s of

0.060 m and 0.095 m were tested with a fixed bed gap b_0 = 0.050 m and inter-log gap b = 0.010 m. Solid volume fraction φ ranged from 0.393 to 0.453. Two discharges, Q = 0.022 m³/s (80% bankfull) and Q = 0.028 m³/s (100% bankfull), produced fixed downstream Froude number Fr_2 = 0.25 throughout. A total of 15 data points from porous Linear configurations are used. The flume experiment setup showing the position and multiple views of the leaky barrier is shown in the Figure 3.1 and Figure 3.2.

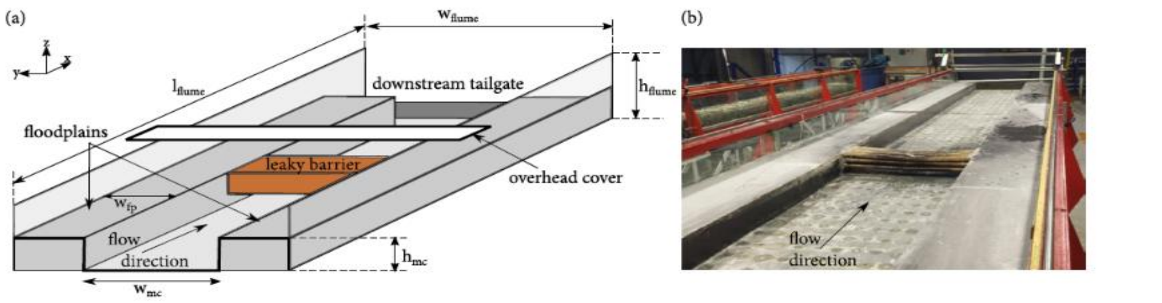

Figure 3.1: 3D schematic (a) and photograph (b) of the Cardiff University compound channel flume showing the leaky barrier positioned within the main channel.

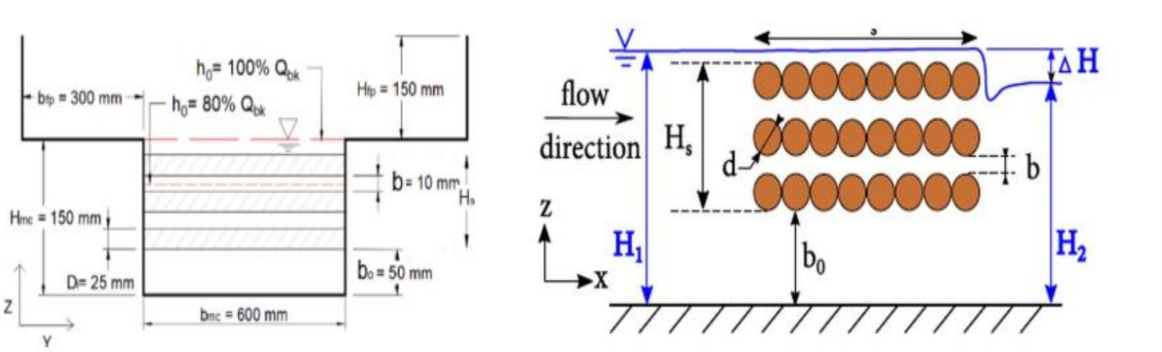

Figure 3.2: Cross-sectional and longitudinal schematic views of the experimental leaky barrier setup (Muhawenimana et al., 2021).

3.2.2 Huang et al. (2022)

The Huang dataset examined hydraulic characteristics in a 16 m × 0.60 m horizontal flume (S = 0) at Wuhan University. A single fixed barrier configuration consisting of 12 longitudinal dowels (d = 0.025 m, L_s = 0.300 m, H_s = 0.095 m) was tested at ten solid volume fractions ranging from φ = 0.276 to 0.392, with b_0 = 0.055 m constant. Discharges varied from Q = 0.012 to 0.028 m³/s, producing Fr_2 = 0.20–0.30 and Reynolds numbers Re = 15,000–31,000. All nine experiments are included.

3.2.3 Schalko et al. (2018, 2019)

The Schalko dataset represents physical model studies of large woody debris jams — naturally forming accumulations rather than engineered barriers — in a 0.40 m wide glass flume at ETH Zurich (S = 0.001).

Cylindrical logs (d = 0.011–0.015 m) were held in place by a metal rack. Barrier heights ranged from H_s = 2.4 to 3.6 m (prototype scale), corresponding to the four sub-configurations CA = 24.3, 11.1, 8.5, and 7.0 m^{-1}. Solid volume fraction φ = 0.278–0.417 and discharges Q = 0.003–0.055 m^3/s were tested, with Fr_2 extending to 1.4, covering near-critical and supercritical downstream conditions. Twenty-two data points are included across all sub-configurations. The large wood accumulation placement in the experimental flume is shown in the Figure 3.3.

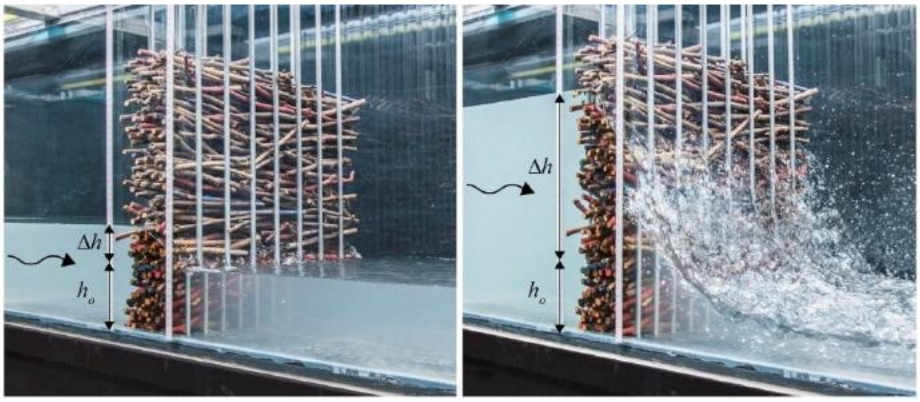

Figure 3.3: Large wood accumulation experiments at VAW, ETH Zurich (Schalko et al., 2018).

3.3 HEC-RAS Model Setup

The following sections describe the HEC-RAS model configuration applied uniformly to all three datasets. The flume geometry, barrier representation, boundary conditions, and calibration procedure were kept consistent across datasets to ensure comparable n_H values.

3.3.1 Flume Geometry Representation

The geometry of the laboratory flume was replicated in the HEC-RAS model as closely as possible. Physical cross-section geometry of the laboratory flume as established during the experimental studies were used to develop the geometry of the HEC-RAS model. Figure 3.4 demonstrates the side-by-side comparison of the cross-section geometry of the laboratory flume from Muhawenimana et al. (left), along with the same cross-section illustrated in the HEC-RAS cross-section data editor (right). The illustration clearly shows that the physical dimensions of the laboratory flume correspond directly to those of the numerical model.

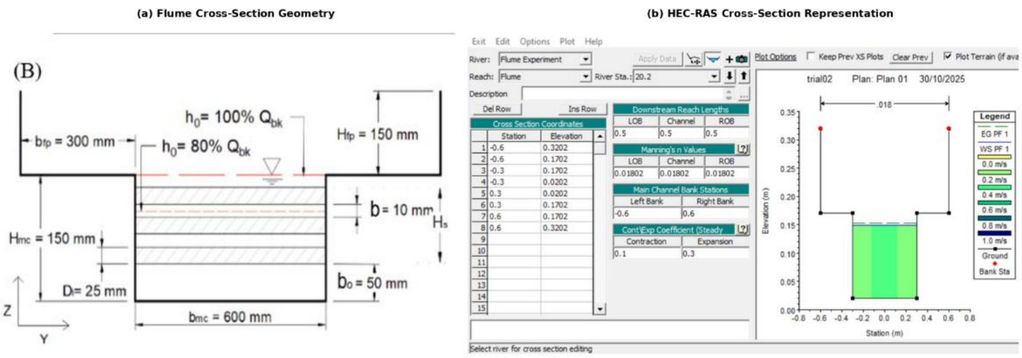

Figure 3.4: (Left) Cross-sectional geometry of the laboratory flume used in Muhawenimana et al. (2021); (Right) Corresponding cross-section reproduced in the HEC-RAS cross-section data editor.

3.3.2 Representation of the Leaky Barrier

The leaky barrier was not modelled as a discrete hydraulic structure within HEC-RAS, but rather represented as a zone of elevated hydraulic resistance using an increased Manning's *n* value. This approach is consistent with the concept of representing localised flow obstructions through equivalent roughness within 1D hydraulic frameworks. The barrier was positioned at the location specified in each research paper, measured from the upstream end of the flume.

To spatially resolve the resistance zone associated with the barrier, cross-sections were placed at very close intervals in the vicinity of the barrier location, thereby allowing the elevated Manning's *n* values to be applied over a well-defined and controlled barrier zone length within the model. Figure 3.5 illustrates the HEC-RAS plan view of the full channel reach, showing the clearly distinguishable barrier zone — identified by the densely-spaced cross-sections highlighted in the model — relative to the regularly-spaced cross-sections in the remainder of the channel. Figure 3.6 represents the zoomed view of the channel showing the leaky barrier zone in the flume.

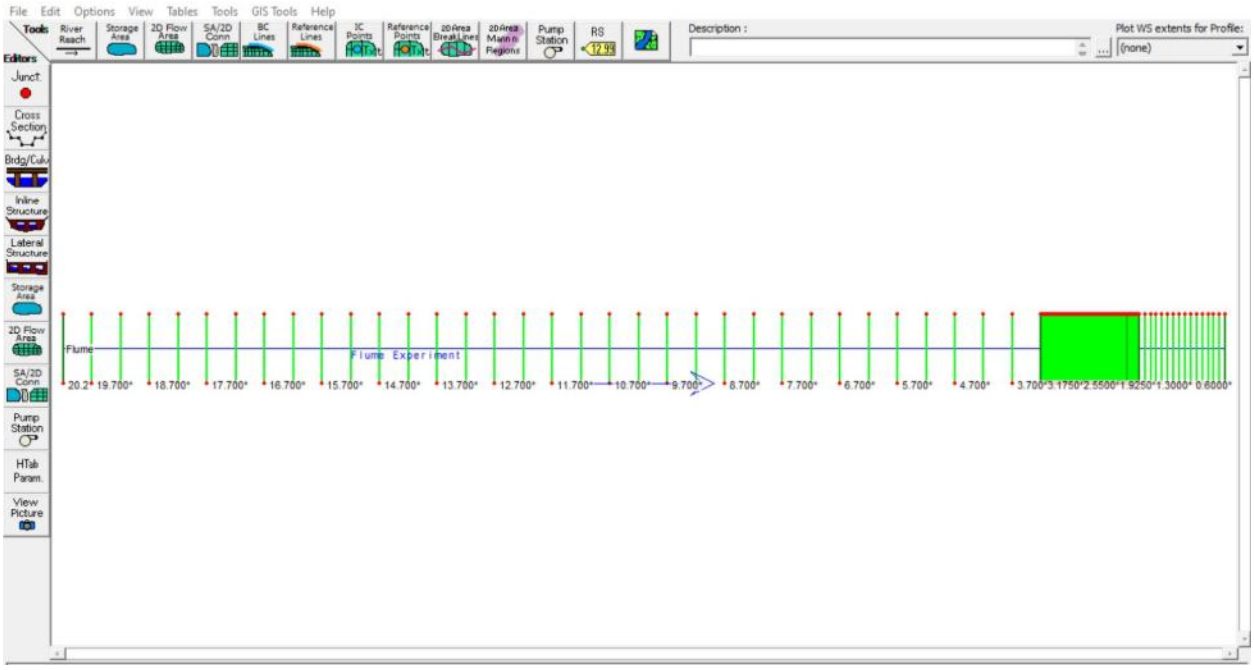

Figure 3.5: HEC-RAS plan view showing the location of the leaky barrier zone (highlighted, right side) with closely-spaced cross-sections, distinguishable from the regularly-spaced cross-sections in the rest of the channel reach.

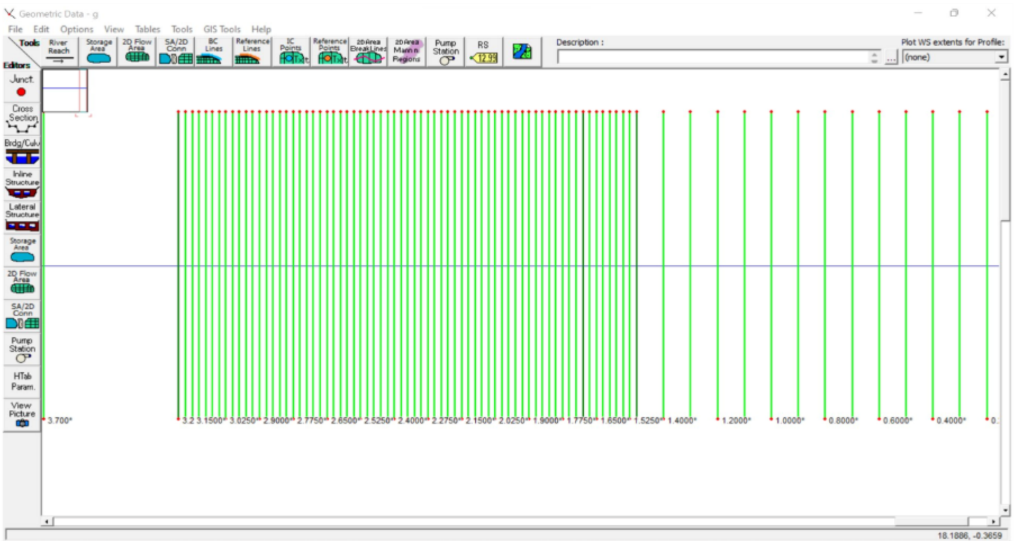

Figure 3.6: Zoomed HEC-RAS plan view of the leaky barrier zone (bounded by the two black marker lines).

For all cross-sections located outside the barrier zone, the Manning's *n* value was assigned as the roughness coefficient corresponding to the smooth bed and walls of the laboratory flume, as specified in each experimental study. Within the barrier zone, an elevated Manning's *n* value was assigned to represent the additional resistance exerted by the leaky barrier on the flow. The magnitude of the Manning's *n* value of the barrier zone were treated as calibration parameter. Figure 3.7 shows the HEC-RAS Manning's *n* values editor, illustrating the two-zone roughness assignment: the standard flume roughness (n = 0.01802) applied to the majority of cross-sections, and the elevated roughness (n = 0.156) applied to cross-sections within the barrier zone (River Stations 1.6250 to 1.5000).

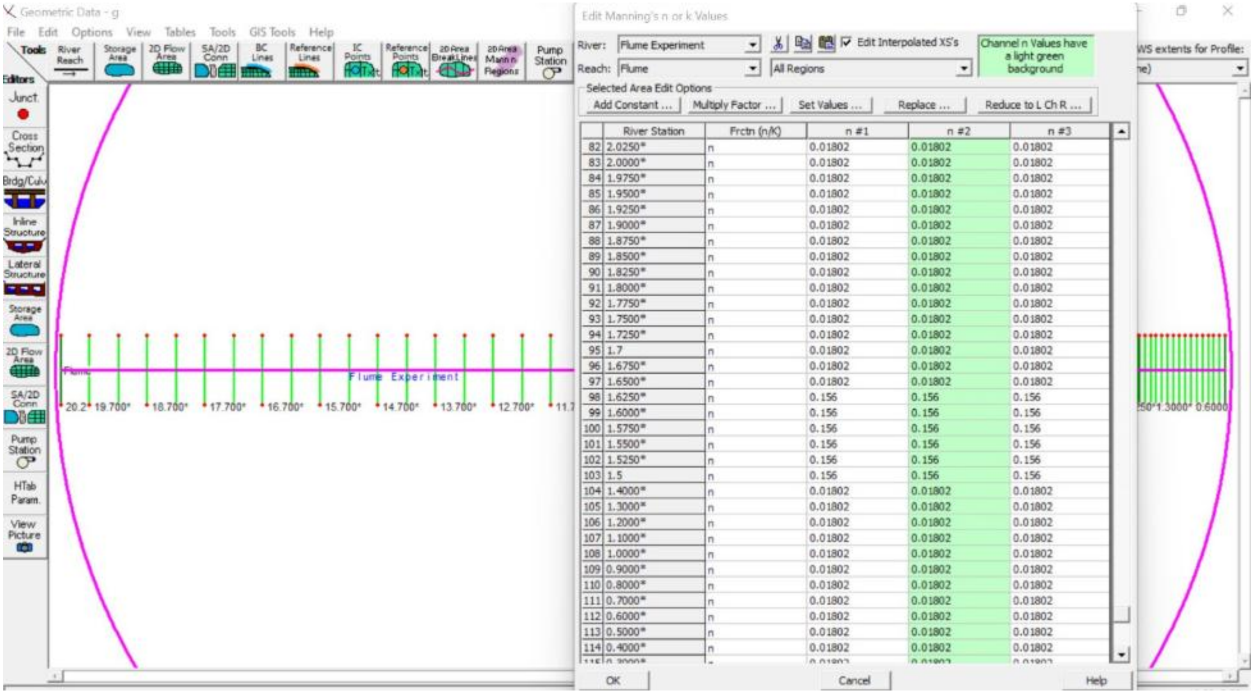

Figure 3.7: HEC-RAS Manning's n values editor showing the flume roughness (n = 0.01802) assigned to standard cross-sections and the elevated roughness (n = 0.156) assigned to cross-sections within the leaky barrier zone (highlighted rows).

3.3.3 Boundary Conditions

Each experimental run was simulated using steady-state flow simulations. For all the simulations the upstream boundary condition was specified as the volume flow rate (Q) for each experimental run from the published literature. The downstream boundary condition was set based on a known water surface elevation that was equivalent to the downstream water depth measured at the exit of the flume and listed in each experimental dataset. As such this combination of boundary conditions reproduces the hydraulics that existed when the physical experiments were conducted, thus constraining the model with respect to the inflow discharge and the tail-water elevation at the downstream end.

A sample HEC-RAS steady state flow data editor and boundary condition setup are shown in Figure 3.8. The upstream discharge (Q = 0.022 m³/s) was specified in the Flow Change Location Table and the downstream known water surface elevation (0.13 m) was input into the Boundary Condition Dialog. Both values represent an 80 percent Bank Full flow condition of the data presented in Muhawenimana et al. (2021).

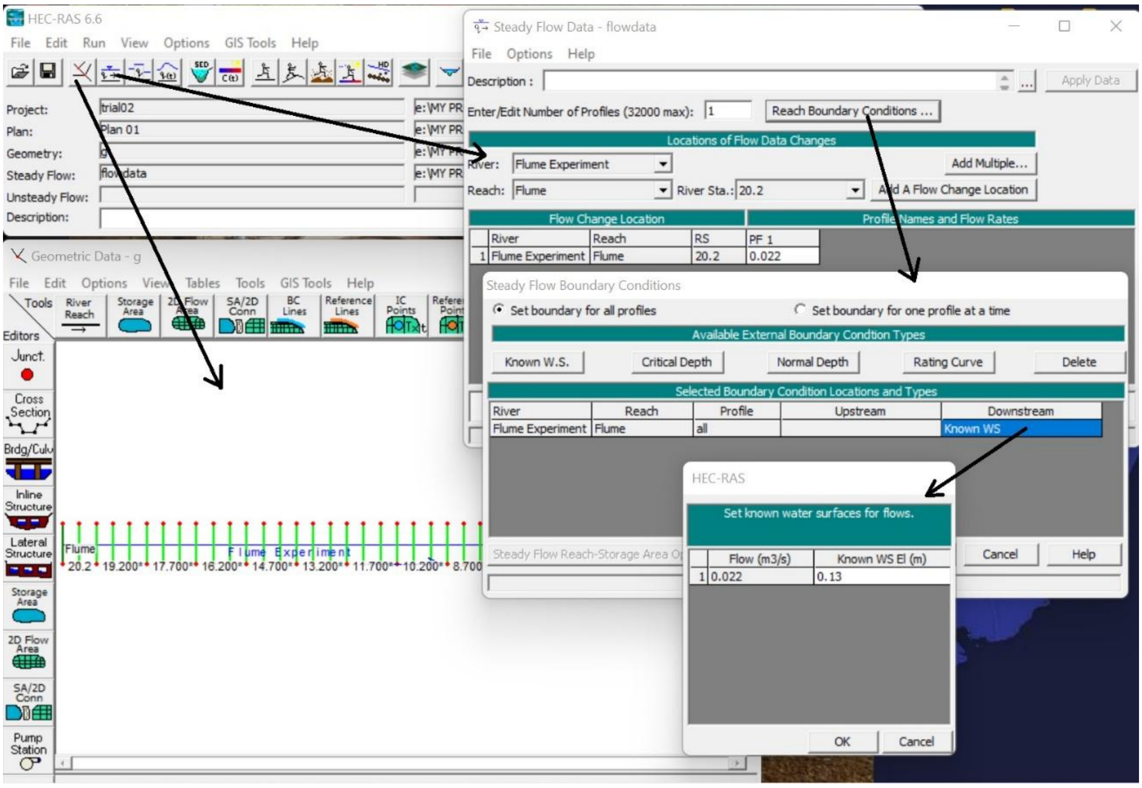

Figure 3.8: HEC-RAS steady flow data editor showing the upstream discharge boundary condition (Q = 0.022 m³/s) and the downstream known water surface elevation boundary condition (0.13 m) for a representative experimental run from Muhawenimana et al. (2021).

3.3.4 Calibration Procedure

The calibration of the HEC-RAS model was done through iterative adjustments to the Manning's *n*-value that is applied to the cross-sections within the barrier zone. In each run, the Manning's *n*-value that was assigned to the barrier zone was systematically adjusted upward from an initial guess until the simulated upstream water surface elevation of the HEC-RAS model matches with the measured upstream water surface elevation in the associated physical experiment. The upstream water surface elevation was chosen as the calibration point because it represents a direct measure of the backwater caused by frictional losses due to the leakage characteristics of the barriers. Once the simulated and measured upstream water surface elevations were shown to be equal, this indicated that the appropriate Manning's *n*-value had been identified for that specific combination of flow rate, barrier design and downstream water level.

The physical length of each barrier was defined as the length of the barrier zone in the model. Therefore, during calibration, there was no adjustment made to either the spatial location or length of the barrier zone. The Manning's *n*-values applied to the cross-sectional area within the barrier zone were therefore the only adjustable parameters. Using this one-parameter calibration method allowed for a single definition of the hydraulic roughness at each test condition. A separate calibration was carried out on each experimental case represented in the three datasets. Each calibration resulted in a unique Manning's *n*-value being established for each combination of flow rate, barrier configuration, and downstream water level.

3.4 HEC-RAS Calibrated Manning's n — Results

Manning's roughness coefficients extracted from HEC-RAS steady-state simulations are presented in Tables 3.1–3.3 for all three datasets. Across all 46 experimental runs, n_H spans from 0.086 (R. Huang, lowest discharge) to 1.426 (Schalko, tallest barrier) — substantially exceeding typical natural channel values of 0.01–0.05. The bed roughness n_0 = 0.009–0.018 is negligible relative to *n*_HEC-RAS in all cases (ratio *n*_HEC-RAS / n_0 ranges from 6 to 158), confirming that barrier resistance, not bed friction, governs the hydraulic response. The following sections present the data and discuss the influence of each key parameter for each dataset individually.

3.4.1 Muhawenimana et al. (2021)

Table 3.1 presents the 15 experimental conditions from Muhawenimana et al. (2021), spanning three groups: (i) φ = 0.4531, H_s = 0.095 m, Q = 0.022 m³/s (rows 1–5) with barrier length L_s varied from 0.10 to 0.20 m; (ii) φ = 0.3927, H_s = 0.095 m, Q = 0.028 m³/s (rows 6–10); and (iii) φ = 0.3927, H_s = 0.060 m, Q = 0.028 m³/s (rows 11–15). Bed slope S = 0.001 and channel width B = 0.6 m are constant throughout.

Table 3.1 — Muhawenimana et al. (2021): 15 experimental conditions and calibrated n_H

Ls (m)	d (m)	B (m)	b_0 (m)	Hs (m)	φ	Q (m³/s)	H_1 (m)	H_2 (m)	Fr_2	af	CA	n_0	n_H
0.100	0.025	0.6	0.05	0.095	0.4531	0.022	0.1340	0.130	0.25	23.076	14.107	0.01802	0.1560
0.125	0.025	0.6	0.05	0.095	0.4531	0.022	0.1351	0.130	0.25	23.076	17.634	0.01802	0.1560
0.150	0.025	0.6	0.05	0.095	0.4531	0.022	0.1353	0.130	0.25	23.076	21.161	0.01802	0.1450
0.175	0.025	0.6	0.05	0.095	0.4531	0.022	0.1335	0.130	0.25	23.076	24.688	0.01802	0.1110
0.200	0.025	0.6	0.05	0.095	0.4531	0.022	0.1348	0.130	0.25	23.076	28.214	0.01802	0.1220
0.100	0.025	0.6	0.05	0.095	0.3927	0.028	0.1735	0.150	0.25	20.000	8.929	0.01802	0.2900
0.125	0.025	0.6	0.05	0.095	0.3927	0.028	0.1754	0.150	0.25	20.000	11.162	0.01802	0.2760
0.150	0.025	0.6	0.05	0.095	0.3927	0.028	0.1757	0.150	0.25	20.000	13.394	0.01802	0.2540
0.175	0.025	0.6	0.05	0.095	0.3927	0.028	0.1750	0.150	0.25	20.000	15.626	0.01802	0.2305
0.200	0.025	0.6	0.05	0.095	0.3927	0.028	0.1775	0.150	0.25	20.000	17.859	0.01802	0.2340
0.100	0.025	0.6	0.05	0.060	0.3927	0.028	0.1570	0.150	0.25	20.000	8.929	0.01802	0.1250
0.125	0.025	0.6	0.05	0.060	0.3927	0.028	0.1592	0.150	0.25	20.000	11.162	0.01802	0.1339
0.150	0.025	0.6	0.05	0.060	0.3927	0.028	0.1573	0.150	0.25	20.000	13.394	0.01802	0.1050
0.175	0.025	0.6	0.05	0.060	0.3927	0.028	0.1588	0.150	0.25	20.000	15.626	0.01802	0.1100
0.200	0.025	0.6	0.05	0.060	0.3927	0.028	0.1593	0.150	0.25	20.000	17.859	0.01802	0.1085

In each group, CA increases with increasing Ls from 0.10 to 0.20 m at fixed rod spacing. Contrary to the expectation that higher CA leads to greater resistance, n_HEC-RAS falls as CA increases within each group (e.g. Group ii: n falls from 0.290 at CA = 8.9 to 0.231–0.234 at CA = 17.9; overall r = −0.42). This inverse relationship is because here CA is increased by increasing barrier length at fixed porosity, rather than increasing the density of rods. A longer barrier of the same porosity results in the same rod resistance being distributed over a longer streamwise length and therefore the lower friction slope per unit length and lower Manning's n. This length-driven CA mechanism is physically different from the density-driven mechanism in that an increase in the amount of solid material within the unit volume does increase drag.

The effect of barrier height is isolated by comparison of Groups (ii) and (iii) with identical φ = 0.3927, Q = 0.028 m3/s and same range of CA: Hs = 0.095 m yields roughly twice the n of Hs = 0.060 m at matched conditions (e.g. 0.290 vs 0.125 at CA = 8.9; 0.234 vs 0.109 at CA = 17.9). In this dataset the only dominant geometric control is the barrier height, in agreement with the piecewise Manning's n model of Chapter 5 where Hs controls the reference resistance n_{max}.

The group (ii) (φ = 0.3927, higher Q) shows higher n than group (i) (φ = 0.4531, lower Q) which apparently indicates that the lower porosity gives higher resistance. But discharge Q also varies between groups (0.028 vs 0.022 m 3 /s), confounding the φ-n comparison. In Groups (ii) and (iii), where both Q and φ are constant, there is no variation in φ and the independent effect of porosity cannot be disentangled from this dataset alone.

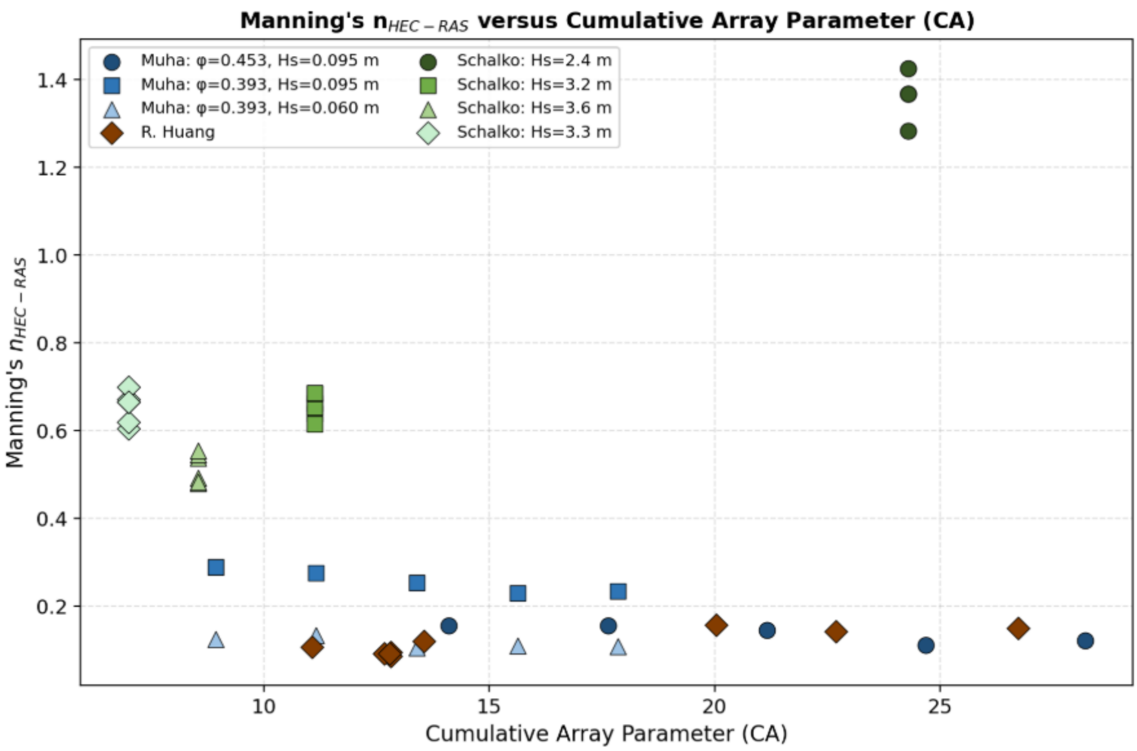

Figure 3.9 — Muhawenimana et al.: n_H vs CA within each group

3.4.2 Huang et al. (2022)

Table 3.2 presents the 9 experiments from Huang et al. (2022). All experiments are conducted on a horizontal bed (S = 0) with fixed L_s = 0.30 m, H_s = 0.095 m, and b_0 = 0.055 m. Solid volume fraction φ varies from 0.276 to 0.392 and discharge Q from 0.012 to 0.028 m³/s, giving CA from 11.1 to 26.7. Unlike the Muhawenimana dataset where L_s varied at fixed Q and φ, both structural density and discharge vary here, making this a direct test of how barrier density and flow conditions jointly govern *n*.

Table 3.2 — Huang et al. (2022): 9 experimental conditions and calibrated n_H

Ls (m)	d (m)	B (m)	b_0 (m)	Hs (m)	φ	S	Q (m³/s)	H_1 (m)	H_2 (m)	Fr_2	af	CA	n_0	n_H
0.3	0.025	0.6	0.055	0.095	0.2945	0.0	0.0120	0.1038	0.1000	0.20	14.999	12.814	0.009	0.0950
0.3	0.025	0.6	0.055	0.095	0.2945	0.0	0.0150	0.1050	0.1000	0.25	14.999	12.814	0.009	0.0860
0.3	0.025	0.6	0.055	0.095	0.2931	0.0	0.0167	0.1074	0.1005	0.28	14.927	12.677	0.009	0.0920
0.3	0.025	0.6	0.055	0.095	0.2755	0.0	0.0168	0.1144	0.1069	0.25	14.031	11.069	0.009	0.1070
0.3	0.025	0.6	0.055	0.095	0.2942	0.0	0.0180	0.1081	0.1001	0.30	14.983	12.785	0.009	0.0930
0.3	0.025	0.6	0.055	0.095	0.3018	0.0	0.0224	0.1393	0.1301	0.25	15.371	13.548	0.009	0.1210
0.3	0.025	0.6	0.055	0.095	0.3924	0.0	0.0280	0.1638	0.1501	0.25	19.985	26.728	0.009	0.1500
0.3	0.025	0.6	0.055	0.095	0.3705	0.0	0.0280	0.1700	0.1590	0.23	18.869	22.693	0.009	0.1430
0.3	0.025	0.6	0.055	0.095	0.3538	0.0	0.0280	0.1772	0.1655	0.22	18.019	20.033	0.009	0.1580

A strong positive correlation exists (r = +0.86), in direct contrast to the inverse Muhawenimana relationship. Here CA increases because rod density increases (lower φ, more solid material per unit volume): rows 1–6 (φ ≈ 0.27–0.30, CA = 11.1–13.5) yield *n* = 0.086–0.107, while rows 6–9 (φ = 0.30–0.39, CA = 13.5–26.7) give *n* = 0.121–0.158. This density-driven CA mechanism genuinely increases drag per unit barrier volume and produces proportionally higher Manning's *n* — the correct physical interpretation absent from the length-driven Muhawenimana comparisons. This confirms that CA is a physically meaningful predictor of *n* only when CA variation is driven by structural density, not barrier length extension.

The three highest-Q runs (Q = 0.028 m³/s, rows 7–9) all produce higher *n* (0.143–0.158) than comparably dense runs at lower Q. Increasing Q raises H_1 and the friction slope, elevating *n* even at the same barrier geometry. The experimental design does not fully decouple φ from Q (higher-φ runs coincide with higher Q), so both contributions cannot be cleanly isolated.

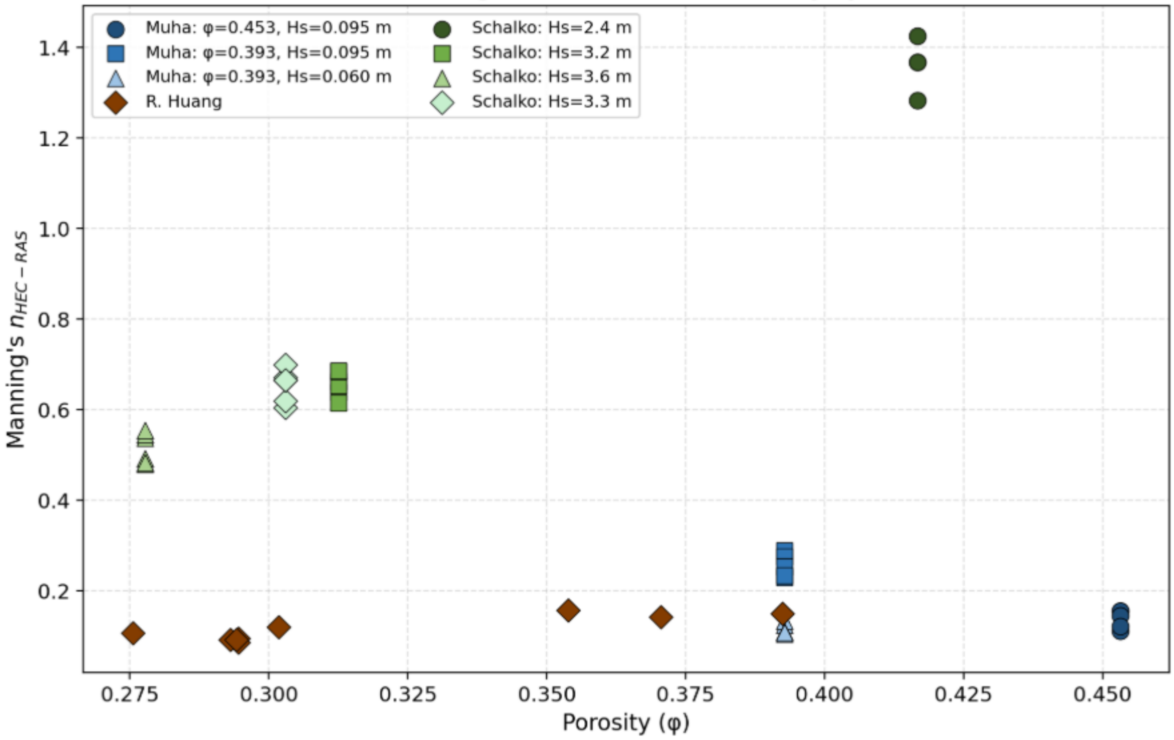

Figure 3.10 — Huang et al.: n_H vs Porosity

3.4.3 Schalko et al. (2018, 2019)

Table 3.3 presents 22 experiments from Schalko across four sub-configurations: H_s = 2.4 m (rows 1–4, CA = 24.3), H_s = 3.2 m (rows 5–10, CA = 11.1), H_s = 3.6 m (rows 11–16, CA = 8.5), and H_s = 3.3 m with d = 0.015 m (rows 17–22, CA = 7.0). With H_s up to 3.6 m and CA up to 48.2, n_H (0.480–1.426) is an order of magnitude higher than the other two datasets, and Fr_2 extends to 1.4, covering near-critical and supercritical conditions absent from Muhawenimana and Huang.

Table 3.3 — Schalko et al. (2018, 2019): 22 experimental conditions and calibrated n_H

Ls (m)	d (m)	B (m)	Hs (m)	φ	S	Q (m³/s)	H_1 (m)	H_2 (m)	Fr_2	af	CA	n_0	n_H
0.100	0.011	0.4	2.4	0.4167	0.001	0.008	0.1848	0.10	0.2	48.229	24.297	0.009	1.2830
0.100	0.011	0.4	2.4	0.4167	0.001	0.016	0.2742	0.10	0.4	48.229	24.297	0.009	1.3680
0.100	0.011	0.4	2.4	0.4167	0.001	0.024	0.3442	0.10	0.6	48.229	24.297	0.009	1.3680
0.100	0.011	0.4	2.4	0.4167	0.001	0.032	0.4165	0.10	0.8	48.229	24.297	0.009	1.4260
0.100	0.011	0.4	3.2	0.3125	0.001	0.008	0.1392	0.10	0.2	36.172	11.131	0.009	0.6620
0.100	0.011	0.4	3.2	0.3125	0.001	0.016	0.1867	0.10	0.4	36.172	11.131	0.009	0.6385
0.100	0.011	0.4	3.2	0.3125	0.001	0.024	0.2266	0.10	0.6	36.172	11.131	0.009	0.6148
0.100	0.011	0.4	3.2	0.3125	0.001	0.032	0.2748	0.10	0.8	36.172	11.131	0.009	0.6545
0.100	0.011	0.4	3.2	0.3125	0.001	0.048	0.3556	0.10	1.2	36.172	11.131	0.009	0.6848
0.100	0.011	0.4	3.2	0.3125	0.001	0.055	0.3847	0.10	1.4	36.172	11.131	0.009	0.6858

Ls (m)	d (m)	B (m)	Hs (m)	φ	S	Q (m^3/s)	H_1 (m)	H_2 (m)	Fr_2	af	CA	n_0	n_H
0.100	0.011	0.4	3.6	0.2778	0.001	0.008	0.1250	0.10	0.2	32.153	8.535	0.009	0.4800
0.100	0.011	0.4	3.6	0.2778	0.001	0.016	0.1659	0.10	0.4	32.153	8.535	0.009	0.4920
0.100	0.011	0.4	3.6	0.2778	0.001	0.024	0.2021	0.10	0.6	32.153	8.535	0.009	0.4840
0.100	0.011	0.4	3.6	0.2778	0.001	0.032	0.2495	0.10	0.8	32.153	8.535	0.009	0.5390
0.100	0.011	0.4	3.6	0.2778	0.001	0.048	0.3167	0.10	1.2	32.153	8.535	0.009	0.5455
0.100	0.011	0.4	3.6	0.2778	0.001	0.055	0.3452	0.10	1.4	32.153	8.535	0.009	0.5546
0.092	0.015	0.4	3.3	0.3030	0.001	0.003	0.0764	0.05	0.2	25.722	6.990	0.009	0.6050
0.092	0.015	0.4	3.3	0.3030	0.001	0.006	0.1067	0.05	0.4	25.722	6.990	0.009	0.6200
0.092	0.015	0.4	3.3	0.3030	0.001	0.008	0.1279	0.05	0.6	25.722	6.990	0.009	0.6650
0.092	0.015	0.4	3.3	0.3030	0.001	0.011	0.1522	0.05	0.8	25.722	6.990	0.009	0.6710
0.092	0.015	0.4	3.3	0.3030	0.001	0.017	0.1966	0.05	1.2	25.722	6.990	0.009	0.6995
0.092	0.015	0.4	3.3	0.3030	0.001	0.020	0.2096	0.05	1.4	25.722	6.990	0.009	0.6660

The sub-configuration with H_s = 2.4 m (CA = 24.3) produces n = 1.283–1.426; H_s = 3.6 m (CA = 8.5) produces n = 0.480–0.555; H_s = 3.3 m (CA = 7.0) produces n = 0.605–0.700. Although the taller barriers produce lower n here, this is because CA is simultaneously lower for taller barriers in the Schalko configurations — the correlation between H_s and CA is negative in this dataset, with the smaller, denser Hs=2.4 m configuration having the highest CA (24.3) and hence the highest n. Barrier height and structural density therefore cannot be decoupled across sub-configurations.

The strongest cross-dataset CA–n correlation arises from between-group variation. CA = 24.3 (H_s = 2.4 m) produces n = 1.28–1.43; CA = 7.0 (H_s = 3.3 m) yields n = 0.61–0.70. Within each sub-group, CA is fixed by the constant geometry, so all within-group n variation is driven by discharge. This cross-group CA–n correlation is partly a H_s/CA covariance artefact rather than a pure density effect.

Within each sub-group, n increases monotonically with Fr_2 as rising Q drives higher H_1 and friction slope: the CA = 24.3 group rises from n = 1.283 at Fr_2 = 0.2 to 1.426 at Fr_2 = 0.8 (r = +0.94 within group); the CA = 7.0 group rises from 0.605 to 0.700 at Fr_2 = 1.2 then decreases slightly to 0.666 at Fr_2 = 1.4, indicating a resistance saturation near critical flow. The overall 22-experiment Fr_2–n correlation is weak (r = −0.16) because between-group H_s differences dominate.

The near-perfect φ–n correlation is structurally imposed: larger H_s corresponds to lower φ in this dataset (H_s = 2.4 m → φ = 0.417; H_s = 3.6 m → φ = 0.278), making φ a proxy for CA. No within-group φ variation exists to test its independent effect. Similarly, *af* ranges from 25.7 to 48.2 — far higher than the other datasets — driven by the much larger H_s values, and the positive af–*n* correlation (r = +0.82) reflects the joint CA/H_s influence.

3.4.4 Cross-Dataset Summary: Key Controls on n_HEC-RAS

The three datasets collectively identify three controlling factors on Manning's *n* in leaky barrier and large woody debris configurations, in decreasing order of importance:

- **Barrier height H_s** — primary control. Schalko (H_s = 2.4–3.6 m) produces *n* = 0.48–1.43; Muhawenimana and Huang (H_s = 0.06–0.095 m) produce *n* = 0.086–0.290. The order-of-magnitude difference across datasets is primarily attributable to H_s, consistent with the piecewise Manning's *n* model (Chapter 5) where H_s governs the n_{max} reference resistance.

- **CA and structural density — secondary, mechanism-dependent.** When CA increases through higher rod density (Huang: r = +0.86; Schalko cross-group: r = +0.95), *n* increases consistently. When CA increases through longer barriers at fixed density (Muhawenimana: r = −0.42), *n* decreases. The predictive model's positive CA exponent (y = 0.4364) correctly captures density-driven CA; length-driven CA extension is outside its physical scope.

3.5 Energy Slope Method for Manning's n

In addition to HEC-RAS calibration, Manning's roughness coefficient *n* was independently calculated from the measured head loss across the barrier using the energy slope method. The advantage of this approach is that it requires only the measured upstream depth H_1, downstream depth H_2, discharge Q, and the geometric dimensions of the channel cross-section — without requiring iterative hydraulic model calibration. This provides an independent, physics-based estimate of *n* that can be directly compared with n_H

Manning's roughness coefficient was calculated from the measured head loss between the upstream gauge (H_1) and downstream gauge (H_2) across the barrier plate length W = 0.450 m:

$$n_{\mathrm{cal}} = \frac{A \times R^{\frac{2}{3}} \times S_{\mathrm{f}}^{\frac{1}{2}}}{Q} \tag{1}$$

where: $H_m = (H_1 + H_2) / 2$ is the mean depth; $A = B \times H_m$ is the cross-sectional flow area; $R = A / (B + 2H_m)$ is the hydraulic radius; $S_f = (H_1 - H_2) / W$ is the friction slope; and Q is the measured discharge. Channel width B

= 0.086 m and barrier length W = 0.450 m apply to the Waikato flume experiment (Section 3.6); the same formula is applied to the published datasets using the corresponding B and W values.

3.5.1 Validation Against Published Research Data

The energy slope formula was applied to all three published datasets using the measured H_1, H_2, Q, B, and L_s values for each experimental run, yielding a calculated roughness coefficient n_{cal}. These values were then compared against the HEC-RAS-calibrated values n_HEC-RAS using the Nash–Sutcliffe Efficiency (NSE) criterion. Table 3.4 summarises the results.

Table 3.4 — NSE: energy-slope n_{cal} vs n_H for each published dataset

Dataset	Barrier Type	N	NSE
Muhawenimana et al. (2021)	ELJ	15	0.344
R. Huang (2022)	ELJ	9	0.884
Schalko (2018/2019)	NLJ	22	0.987

3.5.2 Discussion of Validation Results

The energy slope method produces excellent agreement with HEC-RAS for the Schalko dataset (NSE = 0.987) and good agreement for the Huang dataset (NSE = 0.884). For Schalko, the high NSE reflects large and consistent head drops across the barrier (H_s up to 3.6 m, Q up to 0.055 m^3/s), yielding high signal-to-noise ratios in both H_1–H_2 differences and friction slopes. The Huang dataset, with its horizontal bed (S = 0) and moderate barrier heights (H_s = 0.095 m), also produces clear, measurable head losses across a wide range of discharges and densities, supporting reliable energy slope estimation.

Muhawenimana NSE = 0.344 — explanation. The substantially lower NSE for Muhawenimana (0.344) does not indicate a failure of the energy slope formula, but rather reflects three characteristics of that specific experimental design that reduce agreement between n_{cal} and n_H:

- **Compound channel geometry.** The Cardiff flume has a symmetrical compound cross-section with a main channel (B = 0.6 m) flanked by two 0.3 m floodplains. The energy slope formula used here assumes a simple rectangular channel cross-section, neglecting the lateral flow exchange between the main channel and floodplains. At 100% bankfull discharge (Q = 0.028 m^3/s), floodplain flow contributions modify the effective hydraulic radius and the energy grade line in ways not captured by the simple 1D formula. HEC-

RAS explicitly represents the compound geometry, so n_H is better conditioned to the true cross-sectional flow distribution.

- **Narrow range of H_1 and head drop.** Across the 15 Muhawenimana experiments, H_1 varies only from 0.134 to 0.178 m and the head drop ($H_1 - H_2$) is small (typically 4–28 mm), because the barrier heights are low (H_s = 0.060–0.095 m) relative to the total flume depth. Small absolute head differences amplify the relative effect of measurement uncertainty (gauge precision ±0.1 mm). A 0.1 mm error in a 5 mm head drop represents a 2% error in friction slope, translating directly to a 1% error in n — sufficient to generate substantial NSE degradation across 15 observations.

- **Fixed Fr_2 and near-uniform H_2 across groups.** The fixed downstream Froude number Fr_2 = 0.25 constrains H_2 to approximately 0.130 m (Group i) and 0.150 m (Groups ii–iii) throughout. The resulting small variation in H_1–H_2 across the dataset means that n_{cal} is largely driven by minor fluctuations in head measurement rather than by systematic changes in barrier resistance — reducing the effective signal in the comparison. HEC-RAS iterates to the exact upstream water surface elevation for each run, making n_H more sensitive to true resistance variations, whilst n_{cal} captures measurement noise as well.

Taken together, these three factors explain why the energy slope method, while accurate for datasets with large and well-defined head drops (Schalko, Huang), produces lower NSE for the Muhawenimana dataset where the combination of compound geometry, small absolute head differences, and fixed tailwater conditions creates a challenging measurement environment. The method remains physically valid and is applied without modification to the Lab flume experiment in Chapter 5, where the simple rectangular geometry and controlled measurement conditions are better suited to the energy slope approach.

3.6 Summary

HEC-RAS 1D steady-state simulations were calibrated against the measured upstream water depth H_1 for 46 experimental runs across three published datasets, yielding HecRAS Manning's n_H values ranging from 0.086 (Huang, lowest discharge and density) to 1.426 (Schalko, tallest barrier and highest discharge). The dominant physical controls were identified as: (1) barrier height H_s — the primary between-dataset control; (2) cumulative array parameter CA when driven by structural density — the primary within-dataset control for Huang and Schalko; and (3) discharge and Fr_2 — the within-configuration control at fixed geometry. The energy slope method independently estimates n with excellent agreement for Schalko (NSE = 0.987) and good agreement for Huang (NSE = 0.884). The lower NSE for Muhawenimana (NSE = 0.344) is attributed to compound channel geometry, small head drops relative to gauge precision, and fixed tailwater conditions — structural features of that experimental design that reduce energy slope estimation accuracy, not deficiencies in the underlying formula. These calibrated *n* values and the identified parameter controls form the basis for the Manning's *n* predictive model developed in Chapter 5.

CHAPTER 4 DEVELOPMENT AND VALIDATION OF THE BACKWATER RISE MODEL

4.1 Introduction

This chapter presents the development and experimental validation of an analytical model for predicting the upstream water depth H_1 — and hence the backwater rise $\Delta H = H_1 - H_0$ — induced by channel-spanning leaky barriers. Accurate prediction of backwater rise is central to the hydraulic design of leaky barriers for natural flood management: it determines the extent of upstream inundation, guides barrier placement within a catchment, and provides the boundary condition for downstream routing and HEC-RAS simulation.

The prediction framework adopted in this study is based on the Follett (2020) two-case analytical model, which predicts H_1 from the downstream water depth H_4, the unit discharge q, and the cumulative array parameter CA. A key extension introduced in this study is the CA correction for gapped barriers (Type 2), which modifies the effective drag parameter when the downstream depth H_4 equals or exceeds the barrier height H_s. The framework is validated against four experimental datasets: the University of Waikato laboratory flume experiments (E Lab), and three published datasets from Schalko et al. (2018, 2019), Huang et al. (2022), and Muhawenimana et al. (2021), collectively spanning 308 hydraulic observations across two barrier types and four laboratory facilities.

The chapter is structured as follows. Section 4.2 describes the laboratory flume experimental methodology, including barrier fabrication, flume setup, and measurement procedure. Section 4.3 presents the H_1 prediction model formulation step by step. Section 4.4 presents and discusses the validation results for each dataset. Section 4.5 summarises the findings.

4.2 Laboratory Flume Experiments

The University of Waikato (E Lab) experimental dataset was generated specifically for this study to calibrate and validate the backwater rise model across a range of barrier configurations and flow conditions. All experiments were conducted in the hydraulic testing laboratory of the School of Engineering.

4.2.1 Leaky Barrier Fabrication

Scaled leaky barrier models were fabricated from basawood (balsa wood) side plates and 4.5 mm diameter bamboo dowels. Each side plate was cut to 450 mm × 200 mm and precision-drilled with a regular grid of holes to accommodate the dowel pattern. Dowels were supplied as 300 mm bamboo flower stakes and cut to exactly 86 mm to span the internal flume width. Six distinct dowel hole-occupancy patterns (Configurations I–6) were developed to vary the cumulative array parameter CA across the range 5.58–28.01 m^{-1}. Each configuration was tested at two barrier heights, H_s = 0.10 m and H_s = 0.20 m, with a fixed bed gap b_0 = 0.010 m to allow baseflow passage.

For each configuration, three geometric parameters were calculated from the known dowel count *N*, dowel diameter *d* = 4.5 mm, barrier height H_s, and barrier length L_s = 0.45 m. The **Solid Volume Fraction** (SVF, also denoted φ) is the proportion of the barrier volume occupied by solid dowel material:

$$SVF = \frac{N \times \frac{\pi d^2}{4}}{H_S \times L_S}$$

where the numerator is the total cross-sectional area of all *N* circular dowels and the denominator is the plan area of the barrier face ($H_s \times L_s$). The **porosity** ϕ is the void fraction of the barrier:

$$\phi = 1 - SVF$$

The **Cumulative Array Parameter** (CA, m^{-1}) quantifies the cumulative drag capacity of the dowel array following the momentum-based framework of Follett et al. (2020). For barriers without a bed gap (Type 1, b_0 = 0), CA is defined as:

$$CA = 4 \times \frac{L_s}{\pi d} \times \frac{\varphi}{(1 - \varphi)^3}$$

where φ here denotes the solid volume fraction (SVF). For the gapped barriers used in this study (Type 2, b_0 = 0.010 m), an effective porosity correction is applied when the downstream depth H_4 exceeds H_s, as described in Section 4.3.1. The experimental data for all the configurations were summarised in Appendix section.

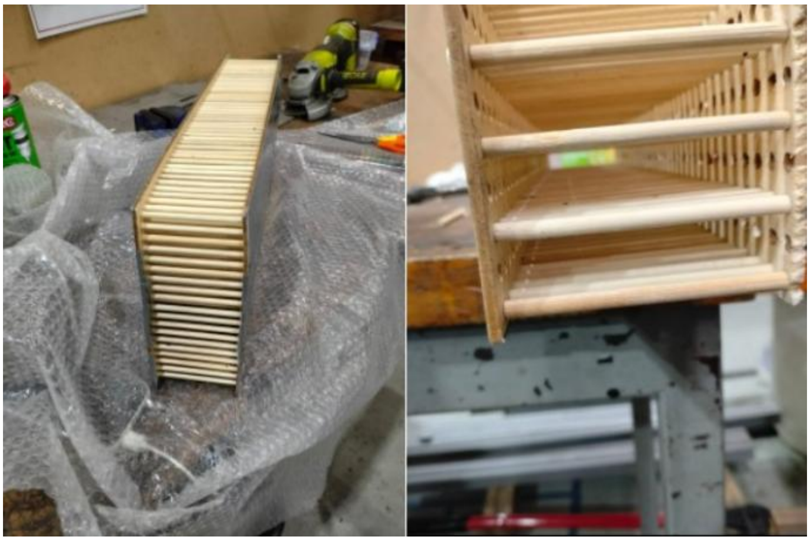

Figure 4.1 Assembled leaky barrier showing key structural features, Pattern 1(left) and Pattern 2(right)

After assembly, each barrier was coated with two coats of exterior-grade clear varnish to prevent water absorption and dimensional change during testing. A photograph of the assembled barrier and a schematic of the six dowel patterns are presented in Figures 4.1 and 4.2.

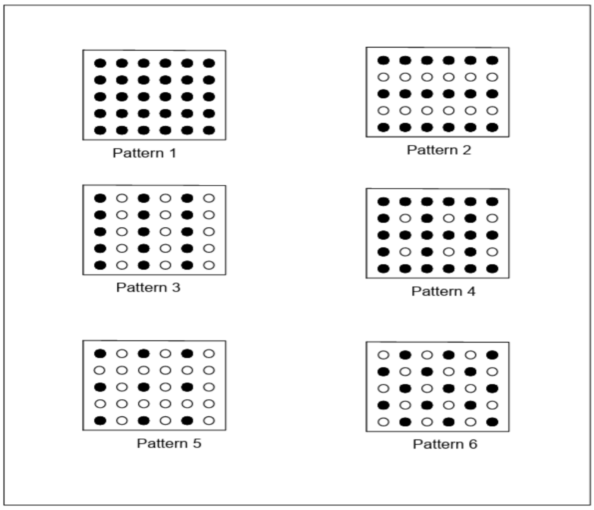

Figure 4.2 Schematic diagram of the six dowel hole patterns tested

4.2.2 Experimental Flume Setup

The experimental programme was conducted in a recirculating tilting flume of internal width B =0. 086 m, total length 5 m, and transparent glass sidewalls. The flume bed slope is adjustable via a mechanical lifting mechanism and was set to s = 0 (horizontal) and s = 0.02 (2%) for different test series. Water is supplied by a centrifugal pump through a recirculating system; discharge is controlled by a gate valve.

The leaky barrier was installed perpendicular to the flow at a designated cross-section. Water depths were measured using rulers at four locations, upstream face of the leaky barrier (H_1), downstream face of the leaky barrier (H_2), and two more locations further downstream of the leaky barrier are shown in Figures 4.3 and 4.4.

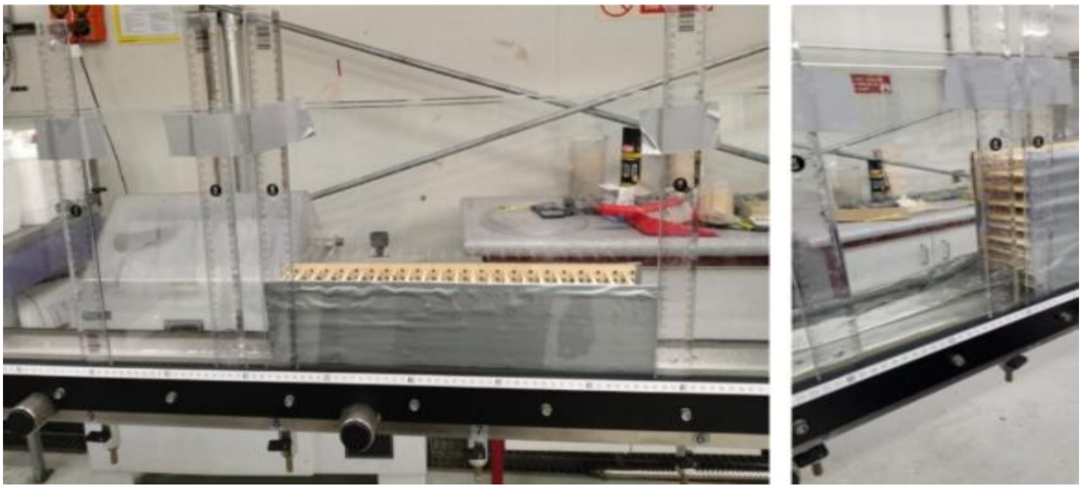

Figure 4.3 Representative dowel pattern configurations 2 as installed in the experimental flume

4.2.3 Experimental Procedure

All experiments were conducted under steady-state flow conditions following six steps:

- **Step 1 — Baseline characterisation.** Without the barrier installed, the pump was started and discharge adjusted to the target flow rate. Water depths at all stations were recorded as baseline (unobstructed) depths H_0.
- **Step 2 — Barrier installation.** The selected barrier configuration was installed at the designated cross-section.
- **Step 3 — Discharge adjustment.** Pump discharge was set to the target experimental value (11 increments per configuration) using the gate valve and flow meter.
- **Step 4 — Steady-state establishment.** Flow was allowed to stabilise for at least three minutes after each discharge change before measurements were taken.
- **Step 5 — Depth recording.** Water depths H_1 and H_4 were recorded at all measurement stations using the point gauge. Each reading was taken as the mean of three repeated measurements to reduce uncertainty.
- **Step 6 — Repetition.** Steps 3–5 were repeated across all target discharges and all six barrier configurations. In total, 262 test runs were completed across six configurations and two bed slopes.

4.3 Backwater Rise Model Formulation

The H_1 prediction model is based on the Follett (2020) momentum-based analytical framework. The framework identifies two flow regimes — free flow (Case A) and tailwater-controlled flow (Case B) — determined by comparing the minimum critical depth $H_{3,min}$ through the barrier with the measured downstream depth H_4. A CA correction is applied for Type 2 gapped barriers when $H_4 \geq H_s$. Equations 4.1–4.3 summarise the complete equation set.

4.3.1 CA Selection

The cumulative array parameter CA governs the hydraulic resistance of the barrier. For Type 1 barriers (b_0 = 0):

$$\mathrm{CA}_{\mathrm{orig}} = \frac{4}{\pi} \cdot \frac{L_s}{d} \cdot \frac{\varphi}{(1-\varphi)^3} \tag{4.1}$$

For Type 2 barriers ($b_0 > 0$), when $H_4 \geq H_s$ the barrier is submerged below the waterline and an effective solid volume fraction φ_{eff} is used:

$$\varphi_{\mathrm{eff}} = \varphi \cdot \frac{(H_s - b_0)}{H_4} \tag{4.2}$$

$$\mathrm{CA}_{\mathrm{corr}} = \frac{4}{\pi} \cdot \frac{L_s}{d} \cdot \frac{\varphi_{\mathrm{eff}}}{(1-\varphi_{\mathrm{eff}})^3} \tag{4.3}$$

When $H_4 < H_s$, the standard $\mathrm{CA}_{\mathrm{orig}}$ applies. The correction ensures the effective drag parameter reflects only the active (above-gap) fraction of the barrier.

4.3.2 Critical Depth $H_{3,\mathrm{min}}$

The minimum critical depth through the barrier (Follett 2020, Eq. 5):

$$H_{3,\mathrm{min}} = \left(\frac{\mathrm{CA} \cdot q^2}{2g}\right)^{\frac{1}{3}} \tag{4.4}$$

$H_{3,\mathrm{min}}$ depends only on CA and unit discharge q; it is independent of upstream conditions. It determines the flow regime: when $H_4 < H_{3,\mathrm{min}}$ → Case A (free flow); when $H_4 \geq H_{3,\mathrm{min}}$ → Case B (submerged).

4.3.3 H_1 Prediction

Case A — Free flow ($H_{3,\mathrm{min}} > H_4$): Flow through the barrier is free-flowing; H_1 is determined by energy principles (Follett 2020, Eq. 6):

$$H_1 = \sqrt{3} \cdot H_{3,\mathrm{min}} \tag{4.5}$$

Case B — Submerged ($H_{3,min} \leq H_4$): Tailwater controls the upstream head; H_1 is computed from the momentum balance (Follett 2020, Eq. 3):

$$H_1 = \sqrt{\left(H_4^{\,2} + \frac{\mathrm{CA} \cdot q^2}{g \cdot H_4}\right)} \tag{4.6}$$

The backwater rise is then $\Delta H = H_1 - H_0$, where H_0 is the unobstructed flow depth at the same discharge.

4.4 Results and Discussion

The H_1 prediction framework was applied to all four datasets (N = 308). Table 4.1 summarises performance across datasets and combined. Figures 4.4–4.6 present $H_{1,pred}$ vs $H_{1,obs}$ scatter plots per dataset and combined.

Table 4.1 — H_1 prediction model performance across all datasets

Dataset	N	Barrier Type	NSE	RMSE (cm)	MAPE (%)
E Lab (Waikato)	262	Type 2 (gap, b_0=0.01 m)	0.887	1.489	11.41
Schalko et al.	22	Type 1 (no gap, b_0=0)	0.942	2.292	7.51
R. Huang	9	Type 2 (gap, b_0=0.055 m)	0.984	0.363	2.75
Muhawenimana	15	Type 2 (gap, b_0=0.05 m)	0.879	0.584	3.44
Combined	308	All datasets	0.932	1.510	10.49

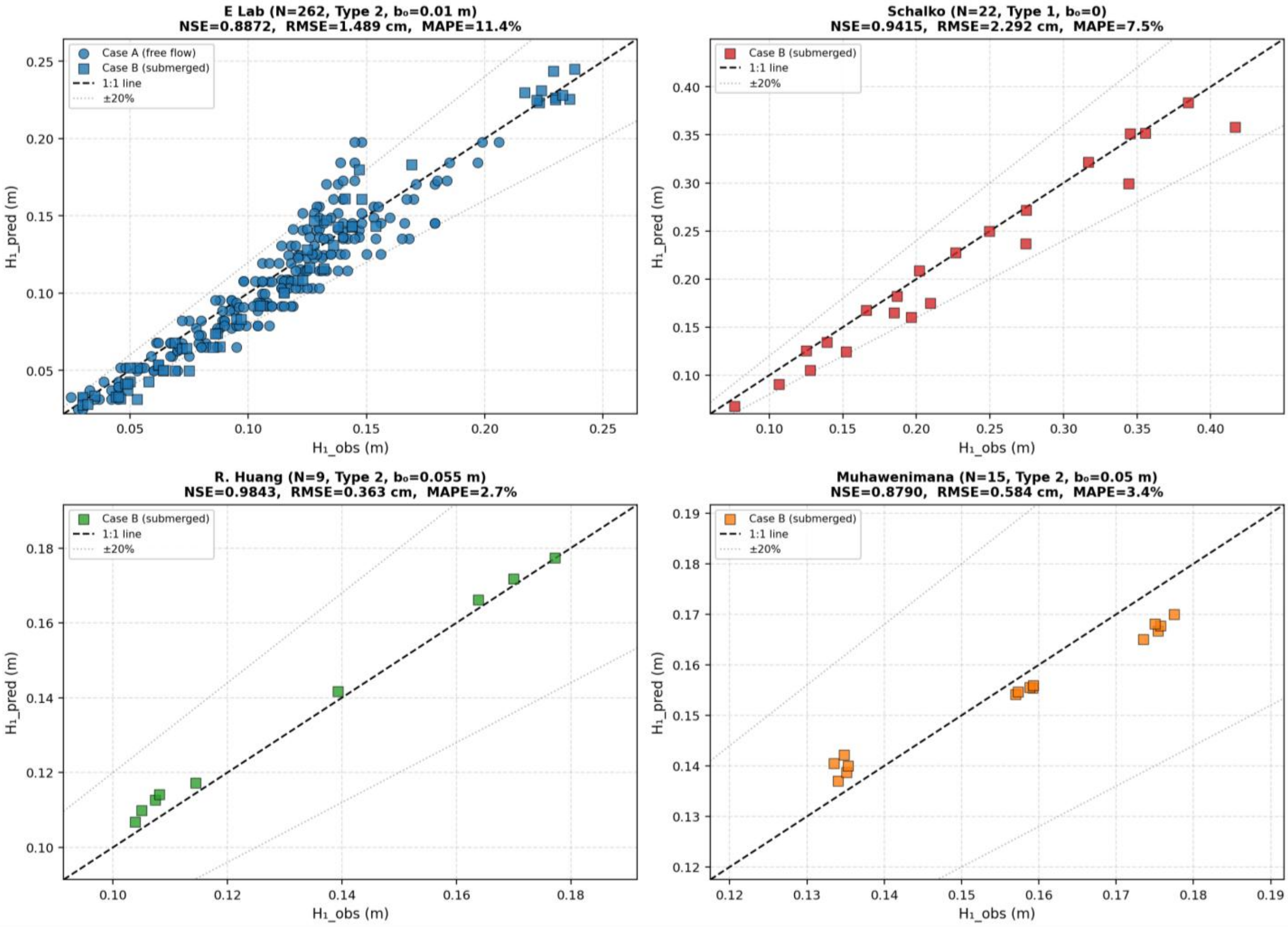

Figure 4.4: H_1_pred vs H_1_obs for each dataset individually. Filled circles = Case A; filled squares = Case B. 1:1 line (dashed) and ±20% band (dotted) shown. R. Huang achieves the best agreement (NSE=0.984); E Lab shows widest scatter at low discharge.

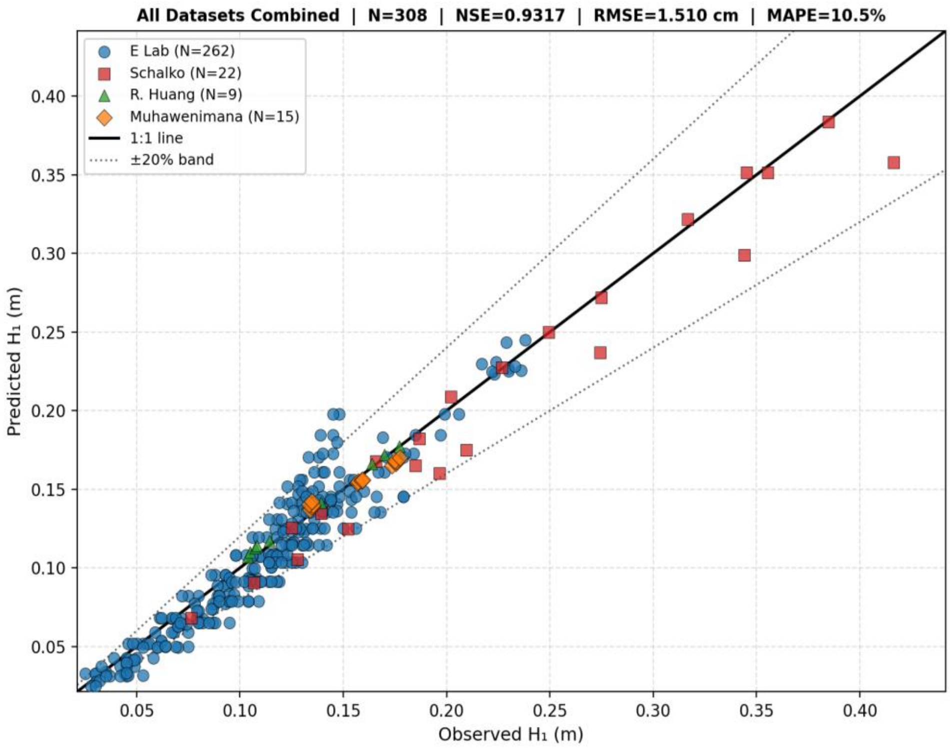

Figure 4.5: Combined H_1_pred vs H_1_obs for all 308 observations. NSE=0.932, RMSE=1.510 cm, MAPE=10.49%. Slight systematic under-prediction (mean error = −4.6%) is visible, driven by low-discharge E Lab observations.

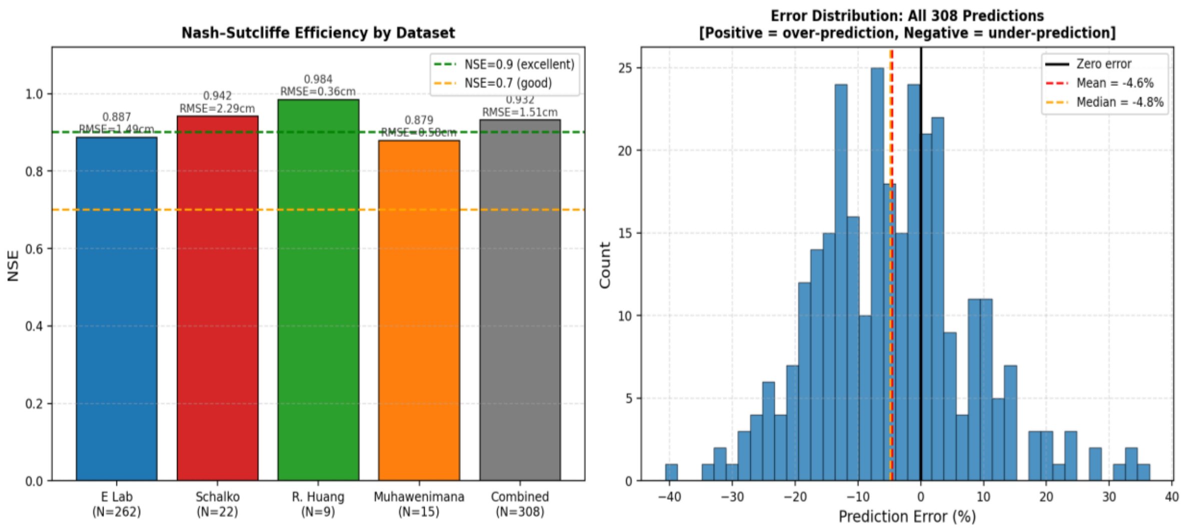

Figure 4.6: NSE per dataset and error distribution across 308 predictions

4.4.1 E Lab Dataset (N = 262, NSE = 0.887)

The E Lab dataset is the largest and most diverse, spanning six barrier configurations, two barrier heights (H_s = 0.10 m and 0.20 m), and 11 discharge steps per configuration. Of the 262 observations, 202 fall in Case A and 60 in Case B, with 22 requiring the CA correction ($H_4 \geq H_s$). The model achieves NSE = 0.887 and RMSE =

1.489 cm. The largest errors occur at very low discharges ($q < 5 \times 10^{-3}$ m²/s) where Case B sensitivity to H_4 measurement uncertainty is highest; at mid-to-high discharges, errors are predominantly within ±10%.

4.4.2 Schalko Dataset (N = 22, NSE = 0.942)

The Schalko dataset represents Type 1 large woody debris jams ($b_0 = 0$) across four sub-configurations with H_1 ranging from 0.068 to 0.418 m. All 22 observations fall in Case B. NSE = 0.942 and RMSE = 2.292 cm; the higher absolute RMSE reflects the large H_1 values in Schalko. MAPE = 7.51% confirms that the standard CA formulation applies well to natural woody debris jams without a bed gap.

4.4.3 Importance of the CA Correction — R. Huang and Muhawenimana

The CA correction is critical for gapped barriers with large b_0. Without correction, the model systematically over-predicts H_1 for both the Huang ($b_0 = 0.055$ m) and Muhawenimana ($b_0 = 0.050$ m) datasets, yielding strongly negative NSE values (Table 4.2). Applying CA_{corr} recovers performance to NSE = 0.984 (Huang) and NSE = 0.879 (Muhawenimana), with RMSE below 1 cm in both cases.

Both the Huang and Muhawenimana datasets consist entirely of Case B (tailwater-controlled, submerged) observations, which is precisely the condition under which the standard CA_{orig} formulation is most exposed to error. In Case B, H_1 is computed directly from the momentum balance using CA and the downstream depth H_4 (Equation 4.6), so any over-estimation of CA propagates directly into an over-estimation of H_1 with no offsetting mechanism. By contrast, in Case A the upstream depth is set by the critical-depth relationship (Equation 4.5), which is comparatively less sensitive to the precise value of CA. This explains why the CA correction proves decisive specifically for these two gapped, fully-submerged datasets, while having no bearing on the Schalko dataset, where $b_0 = 0$ and CA_{orig} already applies without modification.

A representative example from the Huang dataset illustrates the magnitude of the resulting error. For the lowest-discharge run ($\varphi = 0.2945$, $H_s = 0.095$ m, $b_0 = 0.055$ m, $H_4 = 0.1019$ m), the uncorrected solid volume fraction $\varphi = 0.2945$ is referenced to the full barrier height H_s, whereas the effective solid volume fraction $\varphi_{eff} = \varphi \cdot (H_s - b_0)/H_4$ rescales this to approximately 0.116 — close to a 60% reduction — because only the upper 0.040 m of the 0.095 m barrier height lies above the bed gap and is actually submerged below H_4. Because CA scales with $\varphi/(1-\varphi)^3$ (Equation 4.1), this difference in svf is amplified sharply: CA_{orig} evaluates to approximately 12.8 m^{-1} for this run, more than five times the CA_{corr} value of approximately 2.6 m^{-1} obtained once the gap fraction is accounted for. Carried through the Case B momentum equation, this order-of-magnitude inflation in CA is sufficient to explain the strongly negative NSE values obtained without correction, and underlines why the gap fraction $(H_s - b_0)/H_4$ cannot be neglected for barriers with a substantial clear bed gap.

Table 4.2 quantifies this effect across the full Huang and Muhawenimana datasets. Without correction, the model is not merely inaccurate but unusable: an NSE below zero indicates that simply predicting the mean observed H_1 for every run would outperform the uncorrected CA_{orig} model. RMSE values of 4.99 cm (Huang) and 5.19 cm (Muhawenimana) are large relative to the observed H_1 range of these datasets (0.10–0.18 m), confirming that the uncorrected model over-predicts backwater rise by an amount comparable to, or exceeding, the barrier height itself. Once CA_{corr} is substituted, both NSE values move from strongly negative to above 0.87, and RMSE falls below 1 cm in both cases — a reduction of more than an order of magnitude. This before-and-after contrast demonstrates that the effective porosity correction is not a minor refinement but a necessary precondition for the Follett (2020) framework to be applicable to gapped, submerged leaky barriers at all.

Table 4.2 — Effect of CA correction on prediction accuracy for gapped barriers

Dataset	NSE (without corr.)	NSE (with corr.)	RMSE without (cm)	RMSE with (cm)
R. Huang	−1.97	0.984	4.99	0.36
Muhawenimana	−8.55	0.879	5.19	0.58

The over-prediction without correction arises because the standard CA uses the full solid volume fraction φ referenced to the total flow depth, which overestimates the effective drag when the clear bed gap occupies a significant fraction of H_4. The effective solid volume fraction correction $\varphi_{eff} = \varphi \cdot (H_s - b_0)/H_4$ scales the solid log fraction to the active (above-gap) depth only, eliminating this systematic bias.

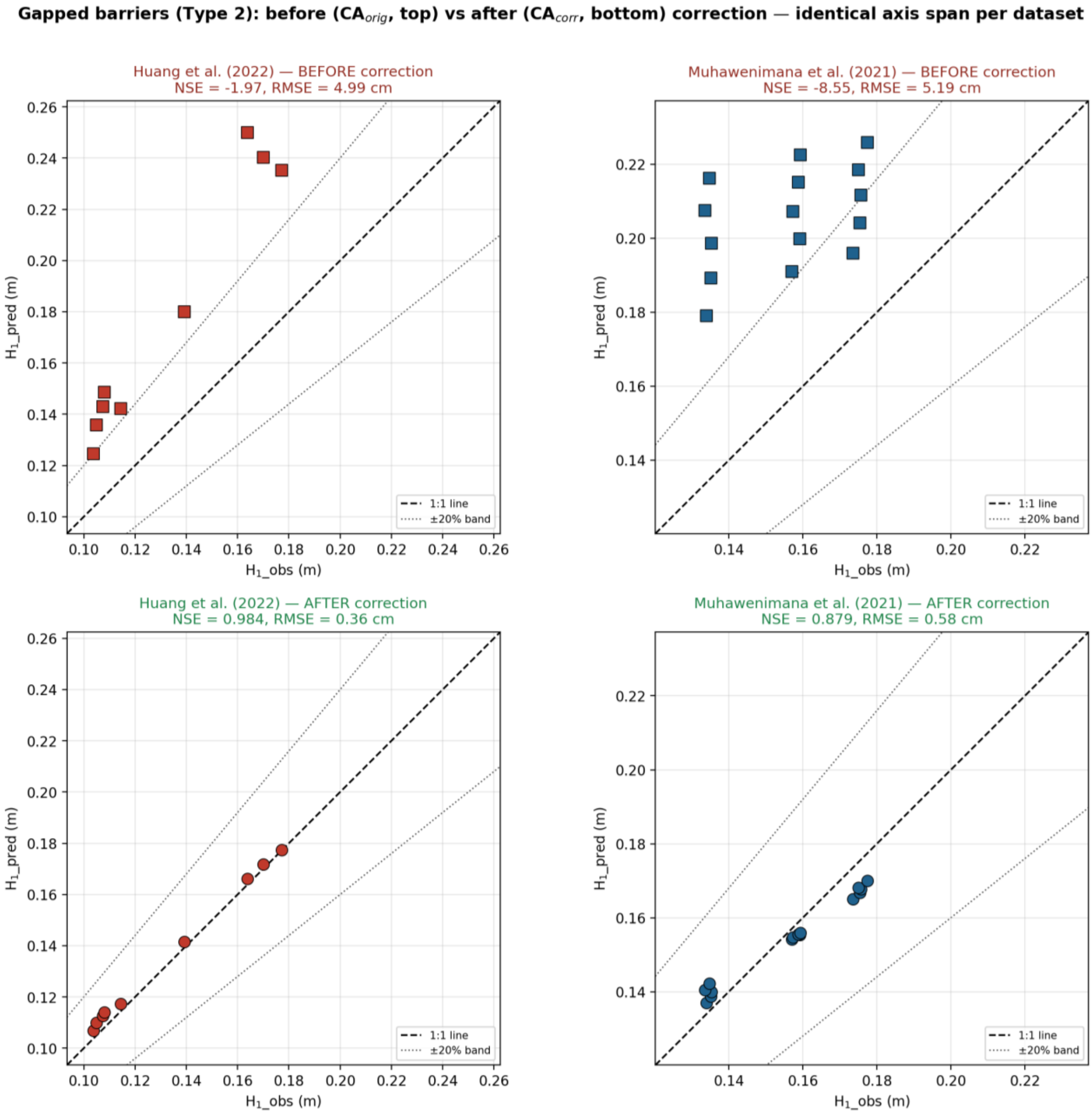

Figure 4.7: Effect of the effective-porosity (CA) correction on H_1 prediction for gapped barriers (Type 2).

4.4.4 Combined Performance

Across all 308 observations, the combined model achieves NSE = 0.932, RMSE = 1.510 cm, and MAPE = 10.49%. A slight systematic under-prediction exists (mean error = −4.6%), driven primarily by low-discharge E Lab observations in Case B where H_4 measurement sensitivity is highest. The ±20% band captures 87.7% of all predictions, confirming the practical reliability of the framework across barrier types and laboratory facilities.

4.5 Summary

The Follett (2020) analytical framework, extended with a CA correction for gapped barriers, provides accurate predictions of upstream water depth H_1 across 308 experimental observations spanning two barrier types, four laboratory facilities, and a wide range of hydraulic conditions. The three-step procedure — CA selection, critical depth $H_{3,min}$ computation, and Case A/B selection — is explicit, non-iterative, and requires only measurable inputs (H_4, q, and barrier geometry). Combined NSE = 0.932 confirms excellent overall predictive skill. The CA correction is essential for barriers with large bed gaps ($b_0 \geq 0.05$ m), where uncorrected predictions over-estimate H_1 by more than an order of magnitude. The E Lab validation dataset from the University of Waikato flume experiments confirms model applicability to the barrier configurations and flow conditions relevant to this study, forming the basis for the Manning's *n* model development presented in Chapter 5.

CHAPTER 5 DEVELOPMENT OF MANNING'S n MODEL

5.1 Introduction

This chapter presents the development and calibration of a predictive equation for Manning's roughness coefficient *n,* for channel-spanning leaky barriers in the unsubmerged flow regime condition ($H_1 < H_s$). The equation is derived from 82 laboratory observations carried over six different leaky barrier configurations. This equation uses a three-step hierarchical regression procedure, and it is validated against the experimental dataset. Section 5.2 presents the energy slope method used to calculate Manning's *n* from measured hydraulic quantities, with complete results for each of the six configurations in Tables 5.1–5.6. Section 5.3 develops the predictive equation step by step, and **then the performance of the equation is analysed**

5.2 Manning's n Calculation Using the Energy Slope Method

Manning's roughness coefficient *n* was calculated for each experimental observation using head loss measured between the water depth measure at the upstream face (H_1) and downstream face (H_2) of the leaky barrier, across the length of the barrier, W = 0.450 m, using the standard energy slope form of Manning's equation for a wide rectangular channel:

$$n_{\mathrm{cal}} = \frac{A \times R^{\frac{2}{3}} \times S_{\mathrm{f}}^{\frac{1}{2}}}{Q} \tag{5.1}$$

where: $H_m = (H_1 + H_2) / 2$ is the mean flow depth (m); $A = B \times H_m$ is the cross-sectional area (m^2); $R = A / (B + 2H_m)$ is the hydraulic radius (m); $S_f = (H_1 – H_2) / W$ is the friction slope; Q is the measured discharge (m^3/s); and B = 0.086 m is the channel width and W = 0.450 m is the length of the barrier.

This formula was applied to all experimental runs at zero bed slope (s = 0) across the six barrier configurations.

Table 5.1 — Summary: calibrated a_k coefficients and performance metrics, all configurations

Config	CA (m^{-1})	CA^y	N	a_k	MAPE (%)	NSE
I	28.0123	4.281	11	0.1825	10.25	0.853
2	12.6210	3.023	11	0.1405	6.82	—
3	11.0764	2.856	11	0.2330	9.91	—
4	18.6403	3.584	11	0.1836	7.22	—
5	5.5753	2.117	11	0.1741	3.48	—
6	11.0764	2.856	11	0.2038	8.64	—
Mean	—	—	66	0.1863	7.49	0.853

5.3 Development of the Predictive Equation for Unsubmerged Condition

The following sections represents the step-by-step derivation of the predictive equation for Manning's *n* using the 82 unsubmerged experimental observations with zero bed slope, tabulated in Section 5.2. The derivation follows a three-step hierarchical regression procedure: Step 1 determines the CA exponent y; Step 2 determines the H_1 exponent r_A; and then Step 3 calibrates a configuration-specific coefficient a_k for each of the six barrier configurations.

5.3.1 Introduction

The hydraulic resistance of a channel-spanning leaky barrier in the unsubmerged flow regime — where the upstream water depth H_1 is less than the barrier height H_s — is governed primarily by the geometry of the barrier and the upstream flow depth. In this regime, the water flows mainly through the porous barrier matrix without overtopping, and the full barrier height H_s is active as a resistance element. This is basically different from the submerged regime ($H_1 > H_s$), in which flow bypasses a part of the barrier resistance by flowing over the crest.

This section presents the step-by-step derivation of a predictive equation for Manning's roughness coefficient *n* applicable to the unsubmerged flow regime. The equation takes the dimensional form:

$$n = a_k \cdot g^{-\frac{1}{3}} \cdot {H_1}^r \cdot \mathrm{CA}^y \qquad (1)$$

where $g = 9.81$ m/s² is gravitational acceleration, H_1 is the upstream water depth (m), CA is the cumulative array parameter (m^{-1}), y and r are empirical exponents, and a_k is a calibration coefficient based mainly on the barrier configuration. The derivation follows a three-step procedure applied to 82 unsubmerged experimental data points collected from the laboratory flume experiment across six barrier configurations, explained in the three subsections below.

5.3.2 Determination of the CA Exponent (y)

The first step removes the dependence of Manning's n on the cumulative array parameter CA while controlling for the effect of upstream depth H_1. In order to achieve this, 18 data points were selected from the entire 82-point unsubmerged dataset by choosing one representative data point per configuration per depth band, yielding three depth bands: $H_1 \approx 4.8$ cm, $H_1 \approx 9.3$ cm, and $H_1 \approx 13.1$ cm, each containing six points spanning the full range of barrier configurations (Configs I, 2, 3, 4, 5, and 6).

Within each depth band, H_1 is approximately constant, so any variation in n across configurations must be related to differences in CA. A linear regression of $\log_{10}(n)$ against $\log_{10}(\mathrm{CA})$ was performed independently for each of these three depth bands, yielding a slope corresponding to the CA exponent y. The three slopes obtained were listed as follows:

Band 1 ($H_1 \approx 4.8$ cm): $y_1 = 0.4819$ ($R^2 = 0.606$)

Band 2 ($H_1 \approx 9.3$ cm): $y_2 = 0.4113$ ($R^2 = 0.528$)

Band 3 ($H_1 \approx 13.1$ cm): $y_3 = 0.4159$ ($R^2 = 0.759$)

The three slopes are consistent across depth bands, ranging narrowly from 0.4113 to 0.4819, this indicates that the CA–n power law relationship is stable and not sensitive to the level of upstream depth at which it is determined. The CA exponent was adopted as the average of the three band slopes:

$$y = \frac{0.4819 + 0.4113 + 0.4159}{3} = 0.4364 \tag{2}$$

Figure 5.1 presents the log–log scatter plots and trendlines corresponding for each depth band. The positive slope in all three bands confirms that Manning's n increases with CA and the barriers with higher frontal area density impose greater hydraulic resistance, consistent with physical expectations for drag-dominated porous obstacles.

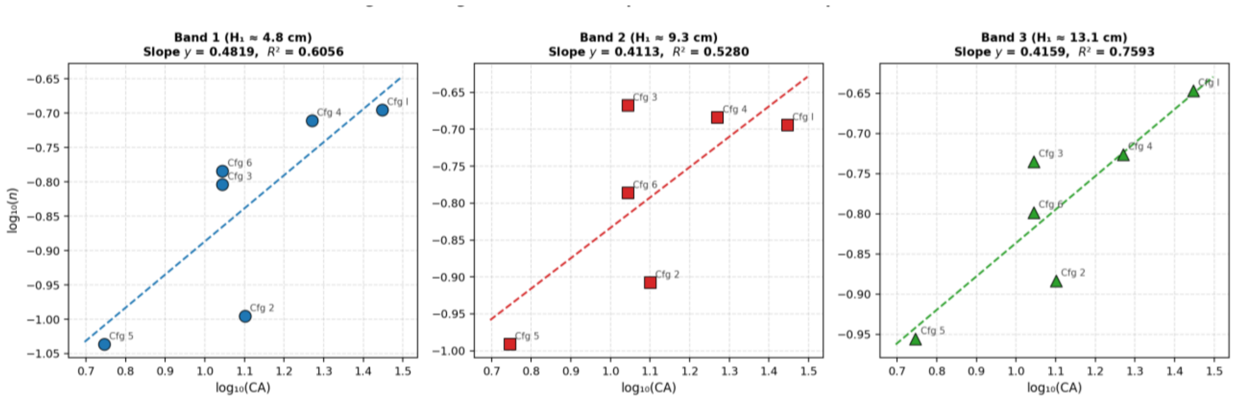

Figure 5.1 — Step 1: Determination of CA Exponent y using three band depths

5.3.3 Determination of the H_1 Exponent (rA)

With the CA exponent determined as $y = 0.4364$, the CA dependence is removed from each observed Manning's n value by computing a residual roughness:

$$n_{\mathrm{resid}} = \frac{n_{\mathrm{obs}}}{\mathrm{CA}^y} \tag{3}$$

This residual n_{resid} represents the depth-dependent component of Manning's n after the CA effect has been removed. A linear regression of $\log_{10}(n_{\mathrm{resid}})$ against $\log_{10}(H_1)$ was then performed using all 82 unsubmerged data points simultaneously across all six configurations, provides the below equation:

$$\log_{10}(n_{\mathrm{resid}}) = 0.2101 \cdot \log_{10}(H_1) + (-1.0708) \quad (R^2 = 0.214) \tag{4}$$

The regression slope $r_A = 0.2101$ is close to the theoretical Manning–Strickler exponent of $1/6 = 0.1667$, which is obtained from the hydraulic radius dependence in Manning's equation for wide channels. Although the higher value of 0.2101 produced a marginally a better statistical fit ($R^2 = 0.214$ versus $R^2 = 0.203$ for $r_A = 1/6$), the difference is small and the theoretical exponent 1/6 was adopted for the final model in order to maintain physical consistency with Manning–Strickler scaling. This approach follows the principle that when an empirical slope is close to a theoretically justified value and the R^2 improvement from the empirical slope is marginal, the theoretical value is preferred for its generalisability. Accordingly:

$$r_A = \frac{1}{6} = 0.1667 \tag{5}$$

Figure 5.2 shows the log–log plot of n_{resid} versus H_1 for all 82 data points. The scatter around the trendline reflects the residual variability not explained by H_1 alone, which is captured by the configuration-specific coefficient a_k determined in Step 3.

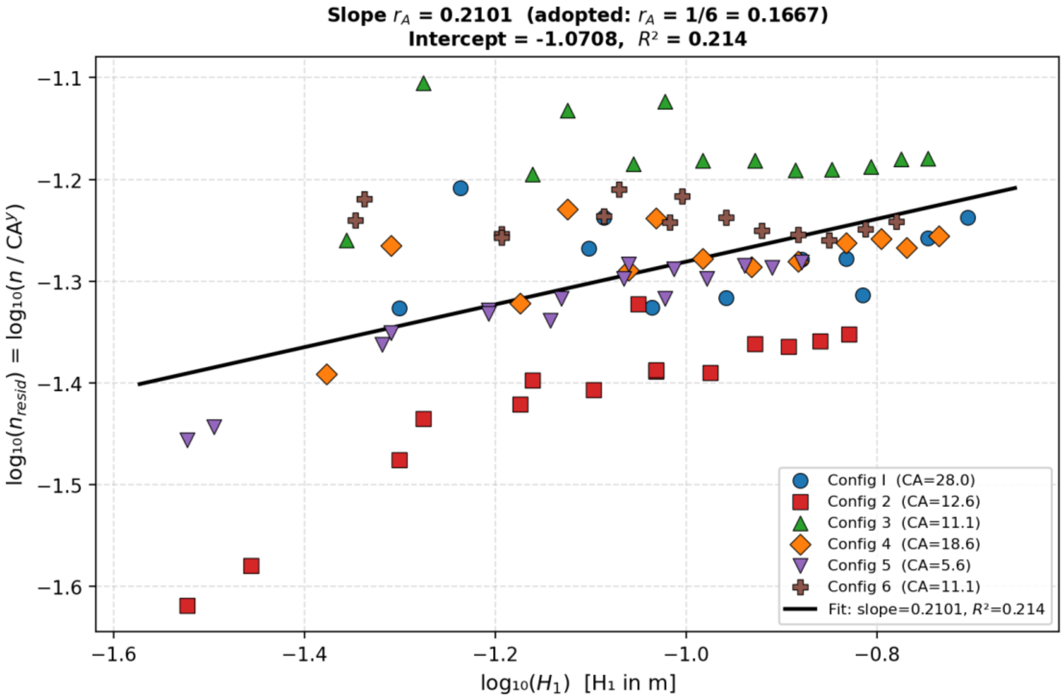

Figure 5.2 — Step 2: Determination of H1 Exponent r_A using unsubmerged data points

5.3.4 Calibration of the Configuration Coefficient (ak)

With both exponents fixed (y = 0.4364, r_A = 1/6), the configuration-specific coefficient a_k is determined for each barrier configuration k by back-calculating an individual coefficient a_{ik} from each experimental data point:

$$a_{ik} = \frac{n_{\text{obs},i}}{\left[g^{-\frac{1}{3}} \cdot H_{1i}^{\frac{1}{6}} \cdot \text{CA}_k{}^{y}\right]} \tag{6}$$

The mean of all individual a_{ik} values within configuration k then gives the representative coefficient a_k:

$$a_k = \frac{1}{N_k} \cdot \sum a_{ik} \tag{7}$$

where N_k is the number of data points in the configuration k. This per-configuration calibration approach allows a_k to absorb any systematic resistance characteristics related to the barrier that is not captured by the CA and H_1 terms alone, such as differences in dowel surface roughness, arrangement geometry (spacing pattern), or end-wall effects between configurations.

Table 5.2 presents the calibrated a_k values for each of the six configurations, along with the associated standard deviation of the individual a_{ik} values and the Mean Absolute Percentage Error (MAPE) of the predictions. Figure 5.3 illustrates the a_k values graphically with ±1 standard deviation error bars.

Table 5.2 — Calibrated ak coefficients and performance metrics per configuration

Config	CA	CA^y	N	ak	std(aik)	MAPE (%)	NSE
I	28.01	4.281	11	0.1825	0.0251	10.25	−0.97
2	12.62	3.023	15	0.1405	0.0143	6.81	0.71
3	11.08	2.856	13	0.2330	0.0322	9.91	−1.25
4	18.64	3.584	13	0.1836	0.0180	7.22	−0.12
5	5.58	2.117	16	0.1741	0.0079	3.48	0.87
6	11.08	2.856	14	0.2038	0.0217	8.64	−7.29
Mean	—	—	82	0.1863	—	7.49	0.853

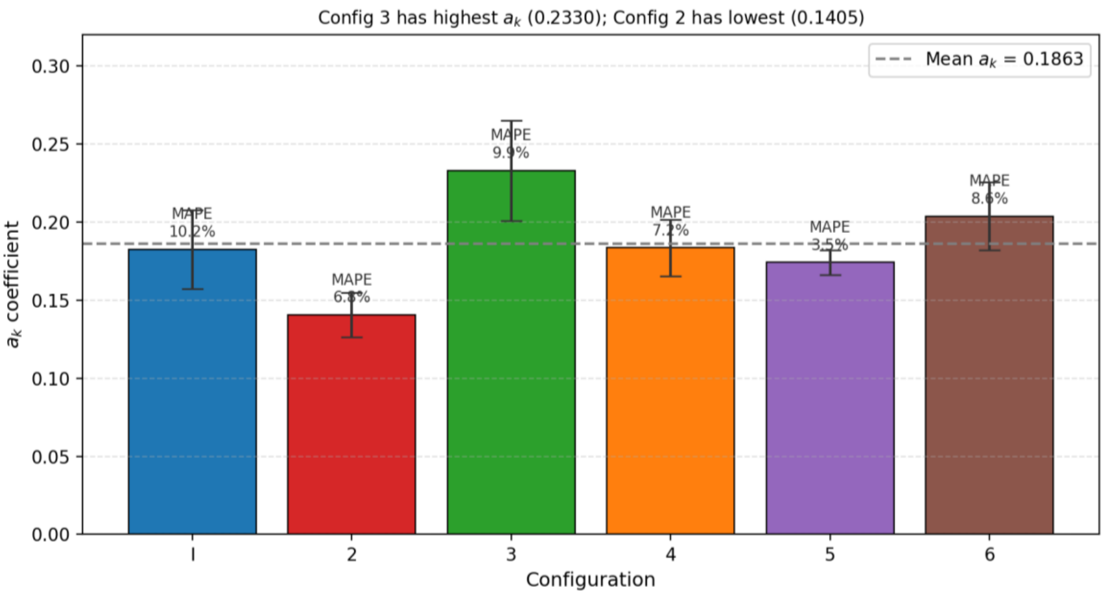

Figure 5.3 — Step3: Calibrated Coefficient a_k per configuration

a_k values range from 0.1405 (Config 2) to 0.2330 (Config 3), with a mean of 0.1863 across all six configurations. The variation in a_k reflects genuine configuration-related resistance characteristics that is not fully captured by the CA parameter alone. Config 3 and Config 6 share the same CA (11.08 m^{-1}) yet have a_k values of 0.2330 and 0.2038 respectively, a difference of 14%, indicating that barriers with the same CA but different spatial arrangements of dowels may prodeuce different levels of hydraulic resistance. Config 5 has the lowest CA (5.58 m^{-1}) and the smallest a_k standard deviation (σ = 0.0079), showing highly consistent behaviour across the full range of H_1 tested.

5.3.5 Final Predictive Equation for Unsubmerged Manning's n

Combining the exponents from Steps 1 and 2 with the configuration-specific coefficient from Step 3, the final predictive equation for Manning's roughness coefficient in the unsubmerged flow regime is:

$$n = a_k \cdot 0.4671 \cdot H_1^{\frac{1}{6}} \cdot \mathrm{CA}^{0.4364} \tag{8}$$

where: n is Manning's roughness coefficient ($s/m^{1/3}$); a_k is the configuration-specific calibration coefficient (dimensionless); $0.4671 = g^{-1/3} = (9.81)^{-1/3}$ ($m^{-1/3}s^{2/3}$); H_1 is the upstream water depth (m); CA is the cumulative array parameter (m^{-1}), defined as CA = $d / (b_0 \cdot L_s)$; and the exponents 1/6 and 0.4364 are universal constants determined from regression analysis across all configurations. This equation is valid for the unsubmerged flow regime, that is, when $H_1 < H_s$.

5.3.6 Application to Experimental Data

The predictive equation was applied to all 82 unsubmerged experimental data points across the six configurations using each configuration's respective a_k value. The predicted Manning's n (n_{pred}) was computed for each data point as:

$$n_{\mathrm{pred}} = a_k \cdot 0.4671 \cdot H_1^{\frac{1}{6}} \cdot \mathrm{CA}^{0.4364}$$

The predicted values were then compared against the observed Manning's n values (n_{obs}) derived from the laboratory flume experiments. Figures 5.4 and 5.5 present the n_{pred} vs n_{obs} comparison plots for individual configurations (Figure 5.5) and all 82 points combined (Figure 5.4).

5.3.7 Results and Discussion

Across all 82 unsubmerged experimental data points, the predictive equation achieves an overall Nash–Sutcliffe Efficiency (NSE) of 0.853, a Mean Absolute Percentage Error (MAPE) of 7.49%, and a Root Mean Square Error (RMSE) of 0.018 s/m$^{1/3}$. An NSE value of 0.853 indicates that the model explains approximately 85% of the total variance in observed Manning's n across all configurations and flow depths, representing very good predictive performance for this type of a semi-empirical hydraulic resistance model. The combined n_{pred} vs n_{obs} plot (Figure 5.4) shows that the majority of data points fall within the ±20% prediction band, with no systematic bias across the full range of observed n values (0.07–0.27 s/m$^{1/3}$).

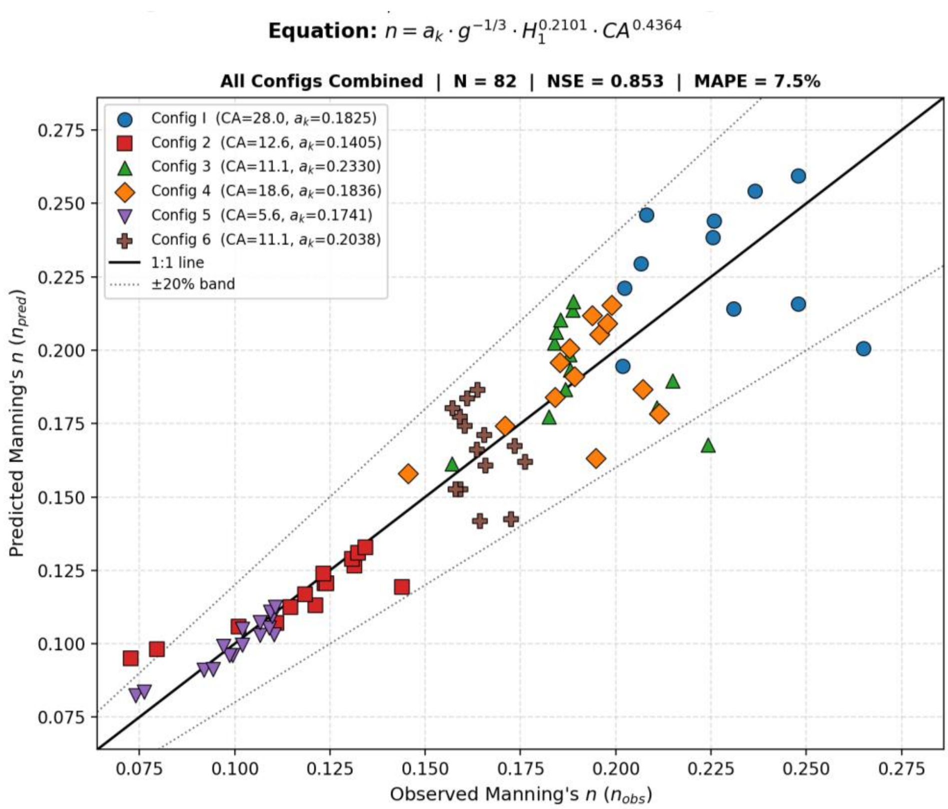

Figure 5.4 — Combined n_{pred} vs n_{obs} for all 82 unsubmerged data points across six configurations.

Figure 5.5 presents the n_{pred} vs n_{obs} scatter plots for each individual configuration, revealing the following pattern of agreement:

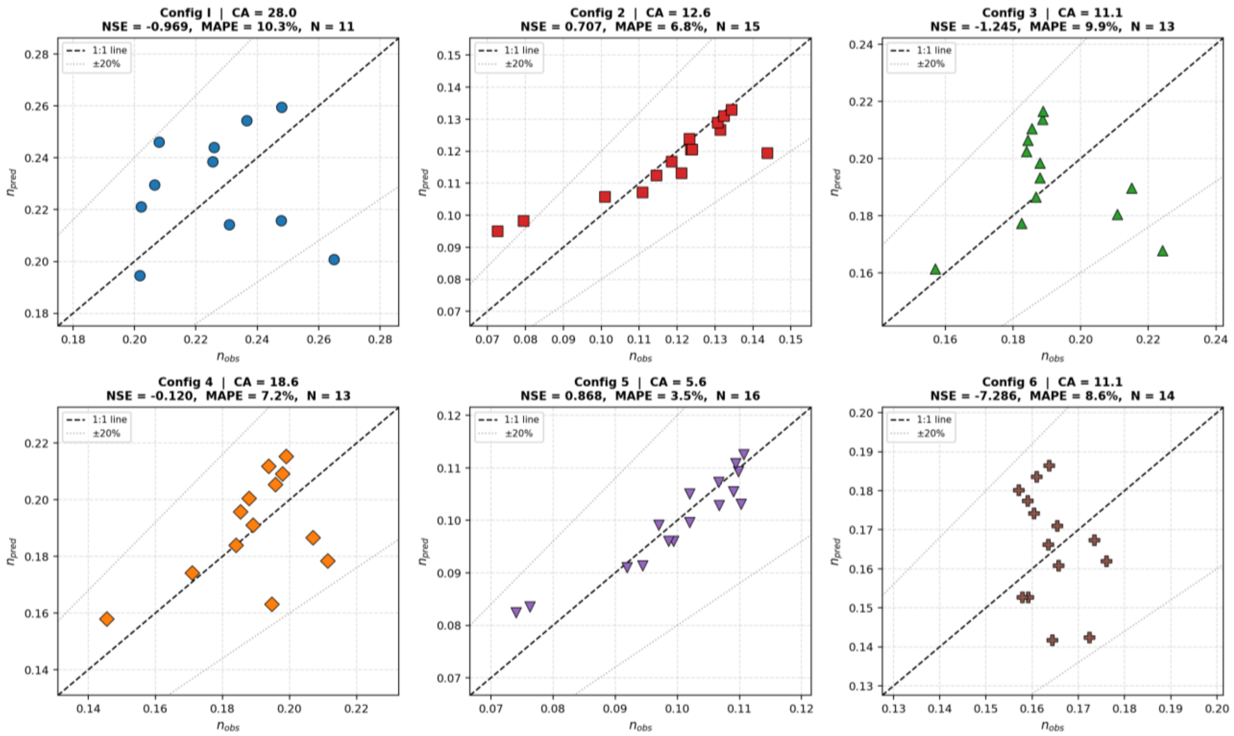

Figure 5.5 — n_{pred} vs n_{obs} for each of the six barrier configurations individually

Config 5 (CA = 5.58 m⁻¹, ak = 0.1741) achieves the best individual prediction accuracy, with MAPE = 3.5% and NSE = 0.87. This configuration has the lowest CA among all six, corresponding to the sparsest barrier arrangement. The high consistency of n_{obs} values across the full H_1 range in Config 5 (standard deviation of a_{ik} = 0.0079, the lowest of all configurations) means the single-coefficient model captures the resistance behaviour with minimal residual scatter. The n_{pred} vs n_{obs} data points align tightly along the 1:1 line across the full range of observed n (0.074–0.111 s/m$^{1/3}$).

Config 2 (CA = 12.62 m⁻¹, ak = 0.1405) performs well overall (MAPE = 6.8%), with the 13 mid-range data points (H_1 = 0.050–0.148 m) falling close to the 1:1 line. However, the two lowest-H_1 points (H_1 = 0.030 m and 0.035 m) are over-predicted by approximately 23–31%, revealing a limitation of the power-law model at very shallow upstream depths where the flow-to-barrier depth ratio is very small and the resistance mechanism may deviate from the assumed scaling.

Config 4 (CA = 18.64 m⁻¹, ak = 0.1836) shows good agreement across the mid-range depths (MAPE = 7.2%), with most data points within ±15% of the 1:1 line. The scatter is slightly higher at low depths (H_1 < 0.07 m), where the model shows modest over-prediction, and at high depths (H_1 > 0.15 m), where slight under-prediction is observed. The overall flat trend in n_{obs} with increasing H_1 (0.183–0.199 s/m$^{1/3}$) is very clearly-reproduced by the gradual rise in n_{pred} driven by the $H_1^{1/6}$ term.

Config 3 (CA = 11.08 m⁻¹, ak = 0.2330) and **Config I (CA = 28.01 m⁻¹, ak = 0.1825)** both show wider scatter in the n_{pred} vs n_{obs} plots, particularly at low H_1 values (MAPE approximately 10%). In both of these configurations, isolated outlier data points at low depths produce unusually high n_{obs} values that the model does not able to capture — for example, in Config I at H_1 = 0.058 m, n_{obs} = 0.265 while n_{pred} = 0.201, an error of 24%. These outliers likely shows the sensitivity of the measurement at very shallow upstream water depths, where small uncertainties in the water level reading transforms to a large relative errors in the computed Manning's n via the energy slope method. Excluding these low-depth outliers, both configurations show satisfactory agreement with MAPE < 8% for H_1 > 0.07 m.

Config 6 (CA = 11.08 m⁻¹, ak = 0.2038) shows a systematic over-prediction at low H_1 (H_1 < 0.07 m, MAPE ≈ 15%) and a gradual transition to under-prediction at high H_1 (H_1 > 0.13 m, MAPE ≈ 13%). This diverging trend — over-prediction at low depths and under-prediction at high depths — suggests that the $H_1^{1/6}$ exponent may slightly overestimate the depth sensitivity for this specific configuration. Notably, Configs 3 and 6 share the same CA value (11.08 m^{-1}) but have different spatial dowel arrangements, and their different a_k values (0.2330 vs 0.2038) indicate that arrangement geometry — beyond what CA captures — influences the hydraulic resistance in this CA range.

5.3.8 Physical Interpretation of the Equation

The predictive equation $n = a_k \cdot g^{-1/3} \cdot H_1^{1/6} \cdot CA^{0.4364}$ has a clear physical structure. The $g^{-1/3}$ term arises naturally from dimensional analysis of the Manning–Strickler relationship, ensuring dimensional consistency. The $H_1^{1/6}$ term reflects the increase in hydraulic radius with upstream depth in a wide rectangular channel, following Manning's equation scaling. The $CA^{0.4364}$ term captures the increase in barrier resistance with frontal area density — a higher CA means more solid material per unit channel cross-section, imposing greater drag on the flow. The configuration coefficient a_k absorbs the remaining configuration-specific variability: differences in dowel spacing pattern, arrangement geometry, and any local three-dimensional flow effects not captured by the depth-averaged 1D representation.

5.3.9 Summary

A three-step hierarchical regression procedure has been used to derive a predictive equation for Manning's roughness coefficient n in the unsubmerged flow regime. The CA exponent $y = 0.4364$ was determined from 18 selected data points across three depth bands; the H_1 exponent $r_A = 1/6$ was adopted from the Manning–Strickler theoretical framework; and the configuration coefficient a_k was calibrated independently for each of the six barrier configurations from the full 82-point unsubmerged dataset. The resulting equation achieves an overall NSE of 0.853 and MAPE of 7.49% across all configurations, with Config 5 showing the best agreement (MAPE = 3.5%) and Configs I and 3 showing the highest scatter (MAPE ≈ 10%). The equation provides a physically interpretable, dimensionally consistent predictive tool for engineering estimation of Manning's n in channel-spanning leaky barriers operating in the unsubmerged regime.

5.4 Development of the Predictive Equation for Submerged Condition

5.4.1 Introduction

The unsubmerged equation derived in Section 5.3 governs Manning's *n* when the upstream water depth H_1 is less than the barrier height H_s, that is, when flow passes only through the porous barrier matrix and the full barrier height actively resists the flow. However, as discharge increases, H_1 can rise upto and exceed H_s, at which point the barrier becomes submerged — flow begins to overtop the barrier crest, bypassing part of its hydraulic resistance.

In the submerged regime ($H_1 \geq H_s$), the resistance mechanism changes fundamentally. The fraction of the flow cross-section actively obstructed by the barrier decreases as H_1 rises above H_s, and the hydraulic gradient across the barrier progressively reduces relative to the total upstream head. Consequently, Manning's *n* decreases as the degree of submergence increases. This behaviour cannot be captured by the unsubmerged power-law equation, which predicts a monotonically increasing *n* with H_1. A separate submerged flow model is therefore required to describe the post-submergence reduction in equivalent roughness.

This section presents the derivation of the submerged Manning's *n* equation, the determination of the submerged exponent *r*, and the assembly of the complete piecewise model that unifies both flow regimes into a single continuous framework applicable across the full range of upstream depths encountered in leaky barrier operation.

5.4.2 The Transition Point: Maximum Manning's n (n_max)

The link between the unsubmerged and submerged models is the Manning's *n* value at the exact moment of submergence onset that is, when $H_1 = H_s$. At this transition point, the full barrier height is still entirely active, so the unsubmerged equation remains valid, producing the maximum possible Manning's *n* for that configuration:

$$n_{\max} = a_k \cdot g^{-\frac{1}{3}} \cdot H_s^{\frac{1}{6}} \cdot \mathrm{CA}^{0.4364} \qquad (9)$$

a_k is the configuration-specific coefficient from Section 5.3 (Table 5.2), $g^{-1/3} = 0.4671\ \mathrm{m}^{-1/3}\mathrm{s}^{2/3}$, $H_s = 0.200$ m is the barrier height, and $\mathrm{CA}^{0.4364}$ uses the universal exponent from Step 1. This $n_{\max}$ value is the peak resistance the barrier can impose on the flow. Once H_1 exceeds H_s, Manning's n begins to decrease from this maximum as the barrier becomes progressively drowned.

Table 5.3 presents the computed n_{max} values for each of the six configurations. Config I has the highest n_{max} (0.2792) consistent with its highest CA (28.01 m^{-1}), while Config 5 has the lowest n_{max} (0.1317) reflecting its lowest CA (5.58 m^{-1}).

Table 5.3 Maximum Manning's n (n_max) at submergence transition for each configuration

Config	CA (m^{-1})	CA^{y}	a_k
I	28.01	4.281	0.1825
2	12.62	3.023	0.1405
3	11.08	2.856	0.2330
4	18.64	3.584	0.1836
5	5.58	2.117	0.1741
6	11.08	2.856	0.2038

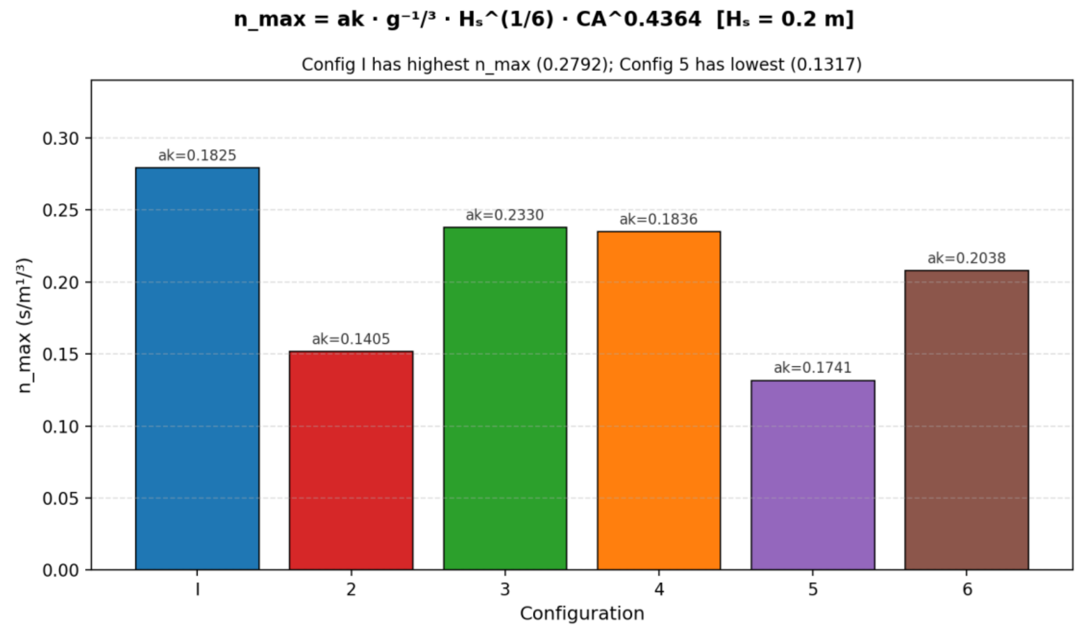

Figure 5.6 — n_{max} per configuration at the submergence transition

5.4.3 Formulation of the Submerged Manning's n Equation

In the submerged regime, Manning's n is modelled as a power-law decay from n_{max} as H_1 rises above H_s. The functional form adopted follows the Manning–Strickler submergence relationship used for weirs and porous structures:

$$n_{\text{sub}} = n_{\max} \cdot \left(\frac{H_1}{H_s}\right)^r \quad [H_1 \geq H_s] \tag{10}$$

where r is a negative exponent capturing the rate of resistance reduction with increasing submergence, and $H_1/H_s > 1$ is the submergence ratio. The negative exponent ensures that n decreases as H_1/H_s increases — physically representing the progressive drowning of the barrier as more water flows over the crest and bypasses the porous barrier zone.

The equation is linked at the transition point: when $H_1 = H_s$, $H_1/H_s = 1$, and $(H_1/H_s)^r = 1^r = 1$, so $n_{\text{sub}} = n_{\max}$, ensuring continuity with the unsubmerged model at the transition point.

5.4.4 Determination of the Submerged Exponent r

The submerged exponent r was determined by a log-linear regression of the observed submergence ratio against the normalised Manning's n. Taking logarithms of both sides of Equation (10):

$$\log_{10}\left(\frac{n_{\text{obs}}}{n_{\max}}\right) = r \cdot \log_{10}\left(\frac{H_1}{H_s}\right) \tag{11}$$

A linear regression of $\log_{10}(n_{\text{obs}}/n_{\max})$ against $\log_{10}(H_1/H_s)$ passing through the origin was performed using all submerged experimental data points. The slope of this regression yields the exponent r. The regression formula is:

$$r = \frac{\sum \log_{10}\left(\frac{H_1}{H_s}\right) \cdot \log_{10}\left(\frac{n_{\text{obs}}}{n_{\max}}\right)}{\sum \log_{10}\left(\frac{H_1}{H_s}\right)^2} \tag{12}$$

The regression yielded:

$$r = -1.2290 \quad (R^2 = 0.390) \tag{13}$$

The negative slope $r = -1.2290$ confirms that Manning's n decreases as the submergence ratio H_1/H_s increases, at a rate steeper than a simple inverse relationship ($r = -1$). The relatively modest $R^2 = 0.390$ reflects genuine scatter in the observed $n_{\text{obs}}/n_{\max}$ ratios, which comes from variability in the transition between unsubmerged and submerged behaviour across different configurations and flow conditions. Despite this scatter, the model captures the overall trend of decreasing resistance with increasing submergence, and the exponent $r = -1.2290$ was adopted for the final model as it minimises prediction error across all configurations.

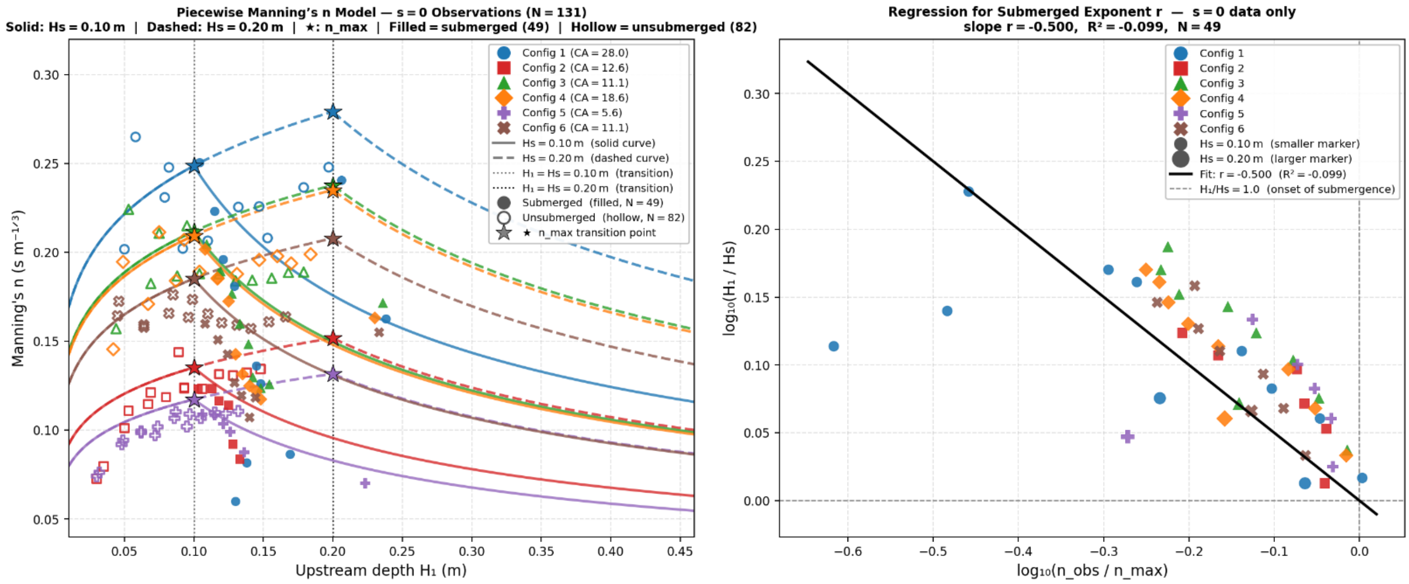

Figure 5.7 — Piecewise Manning's n model showing unsubmerged and submerged branches for all six configurations (left); submerged exponent regression (right).

5.4.5 Final Submerged Manning's n Equation

Substituting the calibrated exponent $r = -1.2290$, the final submerged Manning's n equation is:

$$n_{\text{sub}} = n_{\max} \cdot \left(\frac{H_1}{H_s}\right)^{(-1.2290)} \tag{14}$$

This equation is valid for $H_1 \geq H_s$. At the transition point $H_1 = H_s$, the equation reduces to $n = n_{\max}$, ensuring seamless continuity with the unsubmerged model (Equation 8). The negative exponent (−1.2290) causes n to decay faster than a simple inverse proportion: at $H_1/H_s = 1.5$, n has fallen to approximately 60% of $n_{\max}$, and at $H_1/H_s = 2.0$, to approximately 43% of $n_{\max}$. This relatively rapid decay shows the progressive drowning of the barrier as an increasing proportion of the upstream flow depth lies above the barrier crest.

5.4.6 Complete Piecewise Manning's n Model

Combining the unsubmerged equation (Section 5.3.5) and the submerged equation (Section 5.4.5), the complete piecewise Manning's *n* model for channel-spanning leaky barriers is:

Table 5.1 — Complete piecewise Manning's n model

Flow Regime	Equation	Physical Meaning	Ref.
Unsubmerged ($H_1 < H_s$)	$n = a_k \cdot g^{-1/3} \cdot H_1^{1/6} \cdot CA^{0.4364}$	n increases with H_1 and CA Full barrier active	Eq. (8)
Submerged ($H_1 \geq H_s$)	$n = n_{max} \cdot (H_1/H_s)^{(-1.2290)}$	n decreases as H_1 rises above H_s Barrier partially drowned out	Eq. (14)

Table 5.4. The complete piecewise Manning's n model. The unsubmerged equation governs $H_1 < Hs$; the submerged equation governs $H_1 \geq Hs$. Continuity is ensured at the transition point $H_1 = Hs$ where both equations give n = n_max.

The piecewise structure ensures that the model is physically consistent across the full range of upstream depths: Manning's *n* increases with H_1 in the unsubmerged regime (as more depth is exposed to the full porous matrix), reaches its peak at $H_1 = H_s$ (n_{max}), and then decreases in the submerged regime as the effective active fraction of the barrier diminishes. The model therefore captures both the pre-submergence and post-submergence hydraulic behaviour of leaky barriers in a unified, physically interpretable framework.

5.4.7 Submerged Manning's n Profiles by Configuration

Figure 5.8 presents the predicted submerged Manning's *n* as a function of submergence ratio H_1/H_s for each individual configuration. The submerged model predicts *n* values at H_1/H_s = 1.0, 1.5, and 2.0 for each configuration, illustrating the rate of resistance decay with increasing submergence.

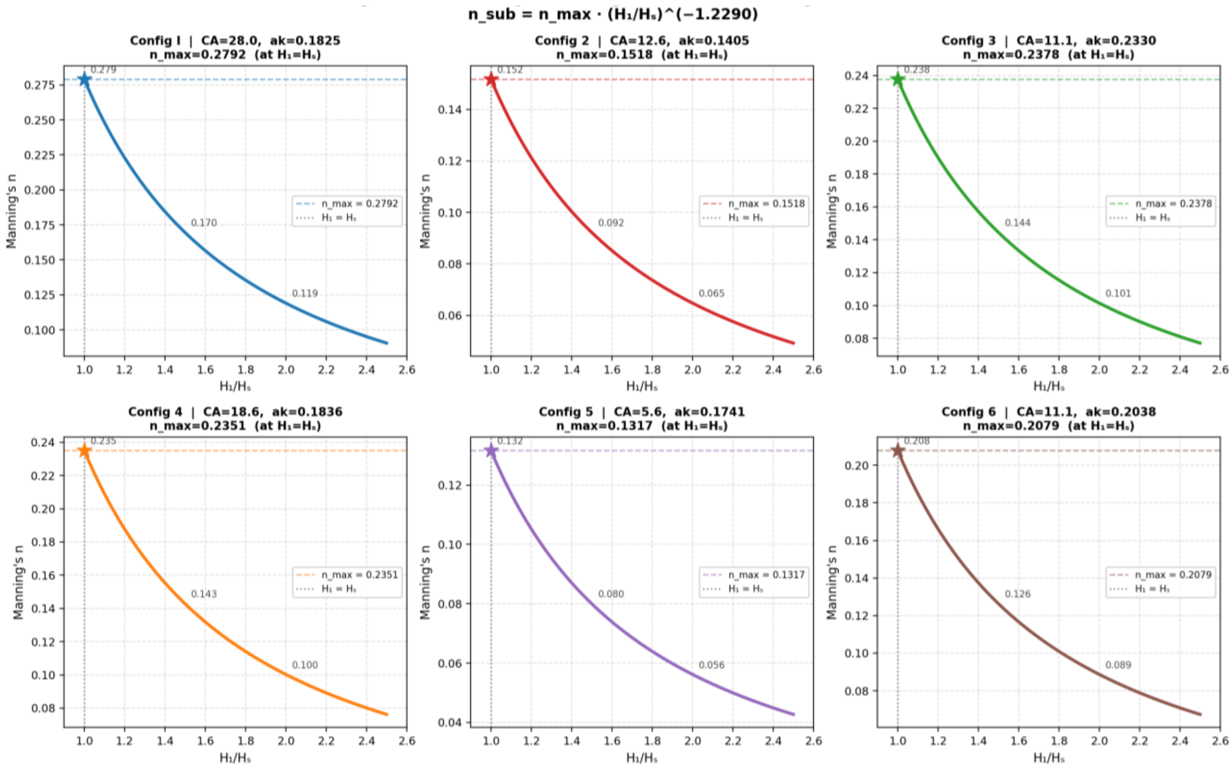

Figure 5.8 — Submerged Manning's n vs submergence ratio H_1/Hs for each configuration. n_max (marked ★) is the value at H_1 = Hs.

Config I (CA = 28.01, n_max = 0.2792) shows the highest absolute submerged *n* throughout the submergence range, decaying from 0.279 at H_1/H_s = 1.0 to 0.170 at H_1/H_s = 1.5 and 0.119 at H_1/H_s = 2.0. Its high n_{max} is driven by the highest CA of all configurations (28.01 m^{-1}), confirming that denser barriers maintain higher resistance even when submerged.

Config 5 (CA = 5.58, n_max = 0.1317) has the lowest n_{max} and lowest submerged *n* throughout. Despite its consistently low resistance, the relative rate of decay with submergence ratio is identical to all other configurations — determined by the universal exponent $r = -1.2290$ — confirming that the submergence sensitivity is a property of the barrier geometry in general, not of individual configurations.

Configs 3 and 6 (CA = 11.08 m⁻¹) share the same CA but have different a_k values (0.2330 vs 0.2038), resulting in different n_max (0.2378 vs 0.2079) and different submerged profiles. This demonstrates that even at the same CA, different arrangement geometries — captured by the configuration coefficient a_k — produce meaningfully different submerged resistance levels.

5.4.8 Results and Discussion

The submerged equation $n = n_{max} \cdot (H_1/H_s)^{(-1.2290)}$ has a clear physical basis. The submergence ratio H_1/H_s represents the total upstream depth relative to the barrier height — a dimensionless measure of how deeply submerged the barrier is. As this ratio increases, the proportion of the upstream flow cross-section that lies above the barrier crest grows, and an increasing volume of flow bypasses the barrier resistance entirely by overtopping. The active resistance fraction — the portion of the flow depth that is impeded by the porous barrier matrix — becomes a progressively smaller fraction of the total flow depth, directly reducing the effective Manning's n.

The exponent $r = -1.2290$ is steeper in magnitude than -1, indicating that the resistance decay with submergence is slightly super-linear: doubling the submergence ratio (H_1/H_s from 1.0 to 2.0) reduces Manning's n to approximately 43% of n_max rather than the 50% that a simple inverse relationship ($r = -1$) would predict. This steeper decay reflects the combined effect of the growing overtopping fraction and the reduction in barrier-induced turbulence intensity as the relative depth above the crest increases.

5.4.9 Continuity at the Transition Point

A key design feature of the piecewise model is its continuity at $H_1 = H_s$. Both branches of the model yield $n = n_{max}$ at this point, ensuring that there is no discontinuity or step-change in predicted Manning's n as the flow transitions between regimes. This is physically important because the transition from unsubmerged to submerged is not instantaneous — in practice, the onset of overtopping occurs gradually as H_1 approaches H_s. The smooth piecewise model appropriately represents this gradual transition without introducing artificial discontinuities that could cause numerical instability in HEC-RAS or CAESAR-Lisflood simulations.

5.4.10 Summary

A submerged Manning's n equation has been derived for the regime $H_1 \geq H_s$, in which Manning's n decays from its maximum value n_{max} as a power-law function of the submergence ratio H_1/H_s. The submerged exponent $r = -1.2290$ was determined by regression of $\log_{10}(n_{obs}/n_{max})$ against $\log_{10}(H_1/H_s)$, with $R^2 = 0.390$. Combined with the unsubmerged equation from Section 5.3.5, the complete piecewise model provides a physically consistent prediction of Manning's n across the full range of upstream depths observed in leaky barrier operation — from shallow unsubmerged flow through the porous matrix to deeply submerged conditions where the barrier is largely overtopped. The model is continuous at the transition point $H_1 = H_s$, where both branches yield $n = n_{max}$, ensuring numerical stability in downstream hydraulic simulations.

CHAPTER 6 CONCLUSIONS AND RECOMMENDATIONS

6.1 Introduction

This chapter draws together the principal findings of the research presented in this study. The chapter is organised into three parts: Section 6.2 summarises the key conclusions arising from the HEC-RAS calibration, the backwater rise model, and the piecewise Manning's n predictive equation; Section 6.3 discusses the practical incorporation of the derived Manning's n relationship into both one-dimensional (1D) and two-dimensional (2D) hydraulic models; and Section 6.4 sets out recommendations for future research.

6.2 Conclusions

The principal aim of this research was to investigate the hydraulic performance of channel-spanning leaky barriers and to develop a practical, physically grounded method for representing their resistance effects in hydraulic models, an aim substantially achieved through a combination of HEC-RAS 1D calibration, laboratory flume experimentation, and regression-based model development. First, calibration of HEC-RAS 1D steady-state models against 46 experimental runs drawn from three published datasets (Muhawenimana et al., 2021; Huang, 2022; Schalko, 2018/2019) confirmed that barrier-induced resistance, rather than bed friction, dominates the hydraulic response of channel-spanning leaky barriers. Calibrated Manning's *n* values ranged from 0.086 to 1.426, exceeding typical natural channel roughness by up to two orders of magnitude. Barrier height H_s was identified as the primary control on Manning's *n* between datasets, while the cumulative array parameter CA — when driven by structural density rather than barrier length — was identified as the dominant within-dataset control. This distinction between density-driven and length-driven CA is an important refinement, since the two mechanisms produce opposite trends in Manning's *n* despite both increasing the same parameter.

Second, the energy slope method provided an independent, non-iterative means of estimating Manning's *n* directly from measured upstream and downstream water depths, without requiring HEC-RAS calibration. Validation produced excellent agreement for the Schalko (NSE = 0.987) and Huang (NSE = 0.884) datasets, and weaker agreement for Muhawenimana (NSE = 0.344), traced to identifiable, dataset-specific causes — compound channel geometry, small absolute head drops relative to gauge precision, and a fixed downstream Froude number constraining the range of head loss — rather than to any deficiency in the formula itself. This confirms the method is reliable provided measurement conditions produce a sufficiently large head loss signal, a condition satisfied by the controlled rectangular geometry of the flume experiment conducted in the Waikato University lab used in Chapters 4 and 5.

Third, the backwater rise prediction framework, extended with an effective solid volume fraction correction (CA_{corr}) for barriers with a clear bed gap, achieved a combined Nash–Sutcliffe Efficiency of 0.932 across 308 observations spanning four datasets and two structural types. The correction proved essential for gapped barriers (submerged cases): uncorrected predictions for Huang and Muhawenimana were unusable (NSE of −1.97 and −8.55 respectively), whereas applying the correction recovered NSE values of 0.984 and 0.879, confirming that the proportion of barrier height occupied by the lower gap must be explicitly accounted for, and that a single uncorrected solid volume fraction term is insufficient for gapped barriers.

Fourth, and most centrally to the aim of this research, a piecewise predictive equation for Manning's *n* was developed and calibrated using 82 unsubmerged and 49 submerged observations from six different barrier configurations used in the lab experiment. In the unsubmerged regime ($H_1 < H_s$), Manning's *n* was shown to follow a power-law dependence on the upstream depth H_1 and the cumulative array parameter CA, with a CA exponent of 0.4364 and an H_1 exponent fixed at the theoretical Manning–Strickler value of 1/6. The resulting equation achieved an overall NSE of 0.853 and a mean absolute percentage error of 7.49% across all six configurations, indicating that the model explains the substantial majority of the variance in observed Manning's *n* using only measurable geometric and hydraulic quantities. In the submerged regime ($H_1 \geq H_s$), Manning's *n* was shown to decay from a maximum value n_{max} following a power law in the submergence ratio H_1/H_s, with a calibrated exponent of −1.2290. The two branches join continuously at the point of submergence onset, where both equations yield $n = n_{max}$, ensuring that the combined model behaves smoothly across the full range of upstream depths likely to be encountered in practice.

Taken together, these findings address the research gap identified in Chapter 1: the absence of a Manning's *n* relationship for leaky barriers that depends only on quantities known prior to a flood event — discharge, channel width, barrier height, lower-gap height, porosity, and barrier length — rather than on the downstream water depth or Froude number, which are typically unknown until after a model has already been run.

6.3 Incorporation of the Manning's n Model into 1D and 2D Hydraulic Models

A central practical outcome of this research is that the derived Manning's *n* relationship may directly compatible with the roughness-based representation already used by practitioners in both one-dimensional and two-dimensional hydraulic modelling software, meaning that no new structural element type or model code is required for its adoption.

In one-dimensional models such as HEC-RAS, leaky barriers are conventionally represented by locally elevating Manning's *n* within the cross-sections occupied by the barrier, as confirmed in the literature reviewed in Chapter 2. The equation developed in Chapter 5 may be applied directly within this existing workflow: for a given barrier geometry (H_s, b_0, L_s, porosity) and a given upstream flow depth H_1, the unsubmerged or submerged branch of the piecewise model returns an estimate of *n* that can be assigned to the relevant cross-sections without iterative calibration against observed water levels. Because H_1 itself depends on *n* through the backwater relationship, the most robust implementation couples the Manning's *n* equation with the backwater rise model of Chapter 4 in a short iterative loop — an initial estimate of H_1 is used to compute *n*, the updated *n* is used to recompute H_1, and the process is repeated until convergence, typically within two to three iterations given the relatively weak (1/6 power) dependence of *n* on H_1. This coupled procedure removes the dependence on engineering judgement or post-hoc calibration that was identified in Chapter 1 as a major limitation of current practice, and may allow a 1D model to be set up with a physically defensible roughness value before any flood event occurs, rather than only after one has been observed and gauged.

In two-dimensional and catchment-scale morphodynamic models such as CAESAR-Lisflood, leaky barriers are likewise commonly represented through localised roughness modification. Since the equation developed here expresses n in terms of the same physical quantities (barrier height, gap height, porosity, and barrier length via CA), it may similarly populate roughness grid cells at a barrier location, with local flow depth from the 2D solution substituted for H1. Because n depends on this local depth, such a model could update barrier roughness dynamically as flow conditions change, rather than using a single constant value.

6.4 Recommendations for Future Research

Based on the conclusions above and the limitations identified throughout Chapters 3 to 5, the following recommendations are made for future research.

First, the proposed coupling between the Manning's n equation and a 2D or catchment-scale model such as CAESAR-Lisflood should be implemented and tested directly, rather than left as a proposed pathway. This would involve assigning the piecewise n equation to barrier cells within a 2D domain and comparing the resulting water surface profiles and flood attenuation behaviour against either laboratory data at reach scale or field observations, to confirm that the relationship derived from flume-scale 1D calibration remains valid when applied within a depth-averaged 2D solver.

Second, the configuration-specific coefficient a_k in the unsubmerged equation currently requires calibration data from each individual barrier arrangement before it can be applied. Future work should investigate whether a_k can itself be related to measurable descriptors of barrier geometry, such as the dowel or log spacing ratio, arrangement pattern, or a secondary porosity-type parameter, so that the equation can be applied to a new, uncalibrated barrier configuration on the basis of its physical description alone.

Thirdly, the lower-than-expected energy slope agreement for the Muhawenimana dataset (NSE = 0.344) was attributed to compound channel geometry and small absolute head drops rather than to a fundamental limitation of the method. This explanation could be tested directly by repeating the energy slope validation on a dataset with a simple rectangular cross-section and larger head drops but otherwise similar barrier geometry, to confirm that the method's performance improves accordingly.

Finally, all the relationships developed in this research are derived from laboratory flume data at model scale. Field-scale validation against an installed leaky barrier or engineered log jam, where Manning's n could be back-calculated from observed flood event water levels and compared against the predictions of the piecewise model, would provide an important test of the equation's applicability beyond the controlled conditions of the laboratory, and would directly support its adoption in operational flood risk and Nature-Based Solution design practice.

REFERENCES

Altmann, M., Vanzo, D., Valero, D., & Schalko, I. (2024). A simple approach to simulate logjams in two-dimensional hydrodynamic models. *Journal of Hydraulic Engineering*, *150*(4), Article 04024007. https://doi.org/10.1061/JHEND8.HYENG-13713

Darzikolaei, S. A. M., Crowe Curran, J., & Liu, X. (2024). Erosion and deposition around porous engineered log jams: Flume experiments and improved predictive formulas. *Journal of Hydraulic Engineering*. https://doi.org/10.1061/JHEND8.HYENG-13983

Follett, E., Schalko, I., & Nepf, H. (2020). Momentum and energy predict the backwater rise generated by a large wood jam. *Geophysical Research Letters*, *47*(17), Article e2020GL089346. https://doi.org/10.1029/2020GL089346

Follett, E., Schalko, I., & Nepf, H. (2021). Logjams with a lower gap: Backwater rise and flow distribution beneath and through logjam predicted by two-box momentum balance. *Geophysical Research Letters*, *48*, Article e2021GL094279. https://doi.org/10.1029/2021GL094279

Follett, E., Schalko, I., & Nepf, H. (2024). Reply to comment by Poppema and Wüthrich on "Momentum and energy predict the backwater rise generated by a large wood jam." *Geophysical Research Letters*, *51*(8), Article e2024GL108808. https://doi.org/10.1029/2024GL108808

Follett, E., & Wohl, E. (2024). Channel-spanning logjams and reach-scale hydraulic resistance in mountain streams. *Geophysical Research Letters*, *51*, Article e2024GL110126. https://doi.org/10.1029/2024GL110126

Huang, R., Zeng, Y., Zha, W., & Yang, F. (2022). Investigation of flow characteristics in open channel with leaky barriers. *Journal of Hydrology*, *613*, Article 128328. https://doi.org/10.1016/j.jhydrol.2022.128328

Leakey, S., Hewett, C. J. M., Glenis, V., & Quinn, P. F. (2020). Modelling the impact of leaky barriers with a 1D Godunov-type scheme for the shallow water equations. *Water*, *12*(2), Article 371. https://doi.org/10.3390/w12020371

Muhawenimana, V., Wilson, C. A. M. E., Nefjodova, J., & Cable, J. (2021). Flood attenuation hydraulics of channel-spanning leaky barriers. *Journal of Hydrology*, *596*, Article 125731. https://doi.org/10.1016/j.jhydrol.2020.125731

Müller, S., Wilson, C. A. M. E., Ouro, P., & Cable, J. (2021). Experimental investigation of physical leaky barrier design implications on juvenile rainbow trout (*Oncorhynchus mykiss*) movement. *Water Resources Research*, *57*(8), Article e2021WR030111. https://doi.org/10.1029/2021WR030111

Munoth, P., & Goyal, R. (2019). Effects of DEM source, spatial resolution and drainage area threshold values on hydrological modeling. *Water Resources Management*, *33*, 3303–3319. https://doi.org/10.1007/s11269-019-02303-x

Poppema, D. W., & Wüthrich, D. (2024). Comment on “Momentum and energy predict the backwater rise generated by a large wood jam” by Follett, E., Schalko, I. and Nepf, H. *Geophysical Research Letters*, *51*(8), Article e2023GL106348. https://doi.org/10.1029/2023GL106348

Reddy, N. N., Reddy, K. V., Vani, J. S. L. S., Daggupati, P., & Srinivasan, R. (2018). Climate change impact analysis on watershed using QSWAT. *Spatial Information Research*, *26*(3), 253–259. https://doi.org/10.1007/s41324-017-0159-6

Schalko, I., Schmocker, L., Weitbrecht, V., & Boes, R. M. (2018). Backwater rise due to large wood accumulations. *Journal of Hydraulic Engineering*, *144*(9), Article 04018056. https://doi.org/10.1061/(ASCE)HY.1943-7900.0001501

Schalko, I., Lageder, C., Schmocker, L., Weitbrecht, V., & Boes, R. M. (2019). Laboratory flume experiments on the formation of spanwise large wood accumulations: I. Effect on backwater rise. *Water Resources Research*, *55*(6), 4854–4870. https://doi.org/10.1029/2018WR024649

Stout, T. L., Majerova, M., & Neilson, B. T. (2016). Impacts of beaver dams on channel hydraulics and substrate characteristics in a mountain stream. *Ecohydrology*, *10*(2), Article e1767. https://doi.org/10.1002/eco.1767

U.S. Army Corps of Engineers – Hydrologic Engineering Center. (2023). *HEC-RAS: Creating a terrain dataset to model a flume experiment* [Online documentation]. https://www.hec.usace.army.mil/confluence/rasdocs/hgt/latest

Vojinovic, Z., Alves, A., Gomez, J. P., Weesakul, S., Keerakamolchai, W., Meesuk, V., & Sanchez, A. (2021). Effectiveness of small- and large-scale nature-based solutions for flood mitigation: The case of Ayutthaya, Thailand. *Science of the Total Environment*, *789*, Article 147725. https://doi.org/10.1016/j.scitotenv.2021.147725

Webber, M. K., Mei, L., & Samaras, C. (2025). Bridging the gap: Riverine nature-based solutions for climate resilient transportation infrastructure in the United States. *npj Urban Sustainability*.

https://doi.org/10.1038/s42949-025-00215-x

Wolstenholme, J. M., Skinner, C. J., Milan, D. J., Thomas, R. E., & Parsons, D. R. (2025). Hydro-geomorphological modelling of leaky wooden dam efficacy from reach to catchment scale with CAESAR-Lisflood 1.9j. *Geoscientific Model Development*, *18*, 1395–1411. https://doi.org/10.5194/gmd-18-1395-2025

Zhuang, W., Ma, J., Mandania, R., & Chen, J. (2025). A review of flood mitigation performance and numerical representation of leaky barriers. *Water*, *17*(13), Article 2023. https://doi.org/10.3390/w17132023

APPENDIX A: LABORATORY EXPERIMENTAL DATA

This appendix presents the complete set of 264 laboratory flume experimental observations collected at the University of Waikato for six barrier configurations (Configurations 1–6) at two barrier heights (Hs = 0.10 m and Hs = 0.20 m) and two bed slopes (s = 0 and s = 0.02). For each run, the measured discharge Q, upstream depth H_1, downstream depth H_2, upstream face depth H_3, far-downstream depth H_4, friction slope Sf, observed Manning's n (n_obs), and cumulative array parameter CA are tabulated.

Table A.1: Experimental data — Configuration 1 — Hs = 0.10 m, s = 0

Barrier properties: Dowel count n = 396, Hs = 0.10 m, b_0 = 0.010 m, Ls = 0.45 m, porosity = 0.8600, CA = 28.0123 m^{-1}

Q (m^3/s)	H_1 (m)	H_2 (m)	H_3 (m)	H_4 (m)	Sf	n_obs	CA (m^{-1})
0.0003	0.0580	0.0230	0.0250	0.0250	0.07778	0.2650	28.0123
0.0006	0.0820	0.0310	0.0330	0.0330	0.11333	0.2478	28.0123
0.0008	0.1040	0.0360	0.0390	0.0400	0.15111	0.2505	28.0123
0.0011	0.1150	0.0380	0.0450	0.0450	0.17111	0.2233	28.0123
0.0014	0.1210	0.0440	0.0520	0.0500	0.17111	0.1961	28.0123
0.0017	0.1290	0.0400	0.0520	0.0550	0.19778	0.1809	28.0123
0.0019	0.1300	0.1250	0.0580	0.0600	0.01111	0.0601	28.0123
0.0022	0.1380	0.1270	0.0550	0.0650	0.02444	0.0816	28.0123
0.0025	0.1450	0.0970	0.0600	0.0670	0.10667	0.1362	28.0123
0.0028	0.1480	0.1000	0.0700	0.0750	0.10667	0.1262	28.0123
0.0028	0.1690	0.1570	0.1570	0.1570	0.02667	0.0865	28.0123

Table A.2: Experimental data — Configuration 1 — Hs = 0.10 m, s = 0.02

Barrier properties: Dowel count n = 396, Hs = 0.10 m, b_0 = 0.010 m, Ls = 0.45 m, porosity = 0.8600, CA = 28.0123 m^{-1}

Q (m^3/s)	H_1 (m)	H_2 (m)	H_3 (m)	H_4 (m)	Sf	n_obs	CA (m^{-1})
0.0003	0.0450	0.0110	0.0100	0.0100	0.07556	0.1573	28.0123
0.0006	0.0720	0.0140	0.0150	0.0150	0.12889	0.1848	28.0123
0.0008	0.0940	0.0220	0.0200	0.0190	0.16000	0.2030	28.0123
0.0011	0.1090	0.0230	0.0240	0.0230	0.19111	0.1962	28.0123
0.0014	0.1170	0.0330	0.0270	0.0270	0.18667	0.1821	28.0123
0.0017	0.1230	0.0410	0.0280	0.0250	0.18222	0.1674	28.0123
0.0019	0.1290	0.0920	0.0400	0.0290	0.08222	0.1382	28.0123
0.0022	0.1330	0.0920	0.0380	0.0290	0.09111	0.1300	28.0123
0.0025	0.1390	0.0900	0.0420	0.0320	0.10889	0.1290	28.0123
0.0028	0.1450	0.0980	0.0600	0.0350	0.10444	0.1219	28.0123
0.0028	0.1470	0.1000	0.0930	0.1100	0.10444	0.1243	28.0123

Table A.3: Experimental data — Configuration 1 — Hs = 0.20 m, s = 0

Barrier properties: Dowel count n = 792, Hs = 0.20 m, b₀ = 0.010 m, Ls = 0.45 m, porosity = 0.8600, CA = 28.0123 m⁻¹

Q (m^3/s)	H_1 (m)	H_2 (m)	H_3 (m)	H_4 (m)	Sf	n_obs	CA (m^{-1})
0.0003	0.0500	0.0210	0.0240	0.0250	0.06444	0.2018	28.0123
0.0006	0.0790	0.0280	0.0320	0.0340	0.11333	0.2309	28.0123
0.0008	0.0920	0.0330	0.0370	0.0390	0.13111	0.2022	28.0123
0.0011	0.1100	0.0360	0.0430	0.0430	0.16444	0.2065	28.0123
0.0014	0.1320	0.0400	0.0510	0.0500	0.20444	0.2255	28.0123
0.0017	0.1470	0.0440	0.0550	0.0550	0.22889	0.2258	28.0123
0.0019	0.1530	0.0490	0.0580	0.0590	0.23111	0.2081	28.0123
0.0022	0.1790	0.0540	0.0600	0.0650	0.27778	0.2365	28.0123
0.0025	0.1970	0.0650	0.0500	0.0690	0.29333	0.2479	28.0123
0.0028	0.2060	0.0710	0.0480	0.0710	0.30000	0.2407	28.0123
0.0028	0.2380	0.2180	0.2200	0.2220	0.04444	0.1628	28.0123

Table A.4: Experimental data — Configuration 1 — Hs = 0.20 m, s = 0.02

Barrier properties: Dowel count n = 792, Hs = 0.20 m, b₀ = 0.010 m, Ls = 0.45 m, porosity = 0.8600, CA = 28.0123 m⁻¹

Q (m^3/s)	H_1 (m)	H_2 (m)	H_3 (m)	H_4 (m)	Sf	n_obs	CA (m^{-1})
0.0003	0.0390	0.0090	0.0100	0.0100	0.06667	0.1188	28.0123
0.0006	0.0670	0.0150	0.0160	0.0140	0.11556	0.1642	28.0123
0.0008	0.0890	0.0200	0.0210	0.0190	0.15333	0.1834	28.0123
0.0011	0.1060	0.0260	0.0240	0.0230	0.17778	0.1892	28.0123
0.0014	0.1220	0.0320	0.0270	0.0270	0.20000	0.1947	28.0123
0.0017	0.1400	0.0370	0.0320	0.0310	0.22889	0.2059	28.0123
0.0019	0.1550	0.0410	0.0370	0.0320	0.25333	0.2101	28.0123
0.0022	0.1710	0.0460	0.0420	0.0350	0.27778	0.2174	28.0123
0.0025	0.1850	0.0530	0.0470	0.0330	0.29333	0.2215	28.0123
0.0028	0.1990	0.0610	0.0530	0.0390	0.30667	0.2261	28.0123
0.0028	0.2290	0.2100	0.2170	0.2200	0.04222	0.1521	28.0123

Table A.5: Experimental data — Configuration 2 — Hs = 0.10 m, s = 0

Barrier properties: Dowel count n = 220, Hs = 0.10 m, b₀ = 0.010 m, Ls = 0.45 m, porosity = 0.9222, CA = 12.6210 m⁻¹

Q (m^3/s)	H_1 (m)	H_2 (m)	H_3 (m)	H_4 (m)	Sf	n_obs	CA (m^{-1})
0.0003	0.0350	0.0290	0.0280	0.0240	0.01333	0.0796	12.6210
0.0006	0.0530	0.0300	0.0310	0.0310	0.05111	0.1110	12.6210
0.0008	0.0670	0.0350	0.0390	0.0390	0.07111	0.1146	12.6210
0.0011	0.0890	0.0400	0.0460	0.0460	0.10889	0.1438	12.6210
0.0014	0.0930	0.0470	0.0520	0.0510	0.10222	0.1236	12.6210
0.0017	0.1030	0.0520	0.0560	0.0550	0.11333	0.1231	12.6210
0.0019	0.1130	0.0580	0.0610	0.0610	0.12222	0.1237	12.6210
0.0022	0.1180	0.0610	0.0630	0.0650	0.12667	0.1165	12.6210
0.0025	0.1250	0.0650	0.0620	0.0690	0.13333	0.1142	12.6210

Q (m^3/s)	H_1 (m)	H_2 (m)	H_3 (m)	H_4 (m)	Sf	n_obs	CA (m^{-1})
0.0028	0.1280	0.0950	0.0670	0.0730	0.07333	0.0923	12.6210
0.0028	0.1330	0.1110	0.1100	0.1110	0.04889	0.0838	12.6210

Table A.6: Experimental data — Configuration 2 — Hs = 0.10 m, s = 0.02

Barrier properties: Dowel count n = 220, Hs = 0.10 m, b_0 = 0.010 m, Ls = 0.45 m, porosity = 0.9222, CA = 12.6210 m^{-1}

Q (m^3/s)	H_1 (m)	H_2 (m)	H_3 (m)	H_4 (m)	Sf	n_obs	CA (m^{-1})
0.0003	0.0250	0.0200	0.0090	0.0090	0.01111	0.0442	12.6210
0.0006	0.0460	0.0300	0.0150	0.0160	0.03556	0.0822	12.6210
0.0008	0.0610	0.0350	0.0200	0.0180	0.05778	0.0954	12.6210
0.0011	0.0750	0.0450	0.0230	0.0210	0.06667	0.1027	12.6210
0.0014	0.0880	0.0500	0.0280	0.0280	0.08444	0.1103	12.6210
0.0017	0.0980	0.0550	0.0330	0.0300	0.09556	0.1112	12.6210
0.0019	0.1060	0.0550	0.0360	0.0320	0.11333	0.1106	12.6210
0.0022	0.1140	0.0510	0.0420	0.0330	0.14000	0.1109	12.6210
0.0025	0.1190	0.0800	0.0450	0.0370	0.08667	0.0973	12.6210
0.0028	0.1230	0.0900	0.0520	0.0370	0.07333	0.0874	12.6210
0.0028	0.1280	0.1040	0.1050	0.1080	0.05333	0.0825	12.6210

Table A.7: Experimental data — Configuration 2 — Hs = 0.20 m, s = 0

Barrier properties: Dowel count n = 440, Hs = 0.20 m, b_0 = 0.010 m, Ls = 0.45 m, porosity = 0.9222, CA = 12.6210 m^{-1}

Q (m^3/s)	H_1 (m)	H_2 (m)	H_3 (m)	H_4 (m)	Sf	n_obs	CA (m^{-1})
0.0003	0.0300	0.0200	0.0200	0.0200	0.02222	0.0727	12.6210
0.0006	0.0500	0.0220	0.0310	0.0310	0.06222	0.1010	12.6210
0.0008	0.0690	0.0350	0.0280	0.0400	0.07556	0.1211	12.6210
0.0011	0.0800	0.0400	0.0470	0.0450	0.08889	0.1185	12.6210
0.0014	0.0930	0.0450	0.0520	0.0510	0.10667	0.1240	12.6210
0.0017	0.1060	0.0670	0.0580	0.0560	0.08667	0.1232	12.6210
0.0019	0.1180	0.0660	0.0620	0.0610	0.11556	0.1315	12.6210
0.0022	0.1280	0.0750	0.0660	0.0610	0.11778	0.1307	12.6210
0.0025	0.1380	0.0800	0.0630	0.0700	0.12889	0.1324	12.6210
0.0028	0.1480	0.0850	0.0700	0.0740	0.14000	0.1343	12.6210
0.0028	0.2450	0.2450	0.2450	0.2450	0.00000	0.0000	12.6210

Table A.8: Experimental data — Configuration 2 — Hs = 0.20 m, s = 0.02

Barrier properties: Dowel count n = 440, Hs = 0.20 m, b_0 = 0.010 m, Ls = 0.45 m, porosity = 0.9222, CA = 12.6210 m^{-1}

Q (m^3/s)	H_1 (m)	H_2 (m)	H_3 (m)	H_4 (m)	Sf	n_obs	CA (m^{-1})
0.0003	0.0300	0.0100	0.0120	0.0110	0.04444	0.0746	12.6210
0.0006	0.0480	0.0220	0.0170	0.0150	0.05778	0.0937	12.6210
0.0008	0.0620	0.0250	0.0210	0.0190	0.08222	0.0999	12.6210
0.0011	0.0720	0.0450	0.0250	0.0230	0.06000	0.0943	12.6210

Q (m³/s)	H_1 (m)	H_2 (m)	H_3 (m)	H_4 (m)	Sf	n_obs	CA (m⁻¹)
0.0014	0.0860	0.0470	0.0300	0.0280	0.08667	0.1067	12.6210
0.0017	0.0980	0.0410	0.0330	0.0300	0.12667	0.1136	12.6210
0.0019	0.1090	0.0620	0.0390	0.0320	0.10444	0.1143	12.6210
0.0022	0.1200	0.0650	0.0420	0.0340	0.12222	0.1191	12.6210
0.0025	0.1300	0.0780	0.0490	0.0360	0.11556	0.1185	12.6210
0.0028	0.1380	0.0820	0.0540	0.0390	0.12444	0.1183	12.6210
0.0028	0.2170	0.2150	0.2150	0.2180	0.00444	0.0485	12.6210

Table A.9: Experimental data — Configuration 3 — Hs = 0.10 m, s = 0

Barrier properties: Dowel count n = 198, Hs = 0.10 m, b_0 = 0.010 m, Ls = 0.45 m, porosity = 0.9300, CA = 11.0764 m⁻¹

Q (m³/s)	H_1 (m)	H_2 (m)	H_3 (m)	H_4 (m)	Sf	n_obs	CA (m⁻¹)
0.0003	0.0530	0.0210	0.0210	0.0200	0.07111	0.2242	11.0764
0.0006	0.0750	0.0275	0.0300	0.0290	0.10556	0.2108	11.0764
0.0008	0.0950	0.0380	0.0380	0.0360	0.12667	0.2150	11.0764
0.0011	0.1090	0.0410	0.0430	0.0420	0.15111	0.2047	11.0764
0.0014	0.1190	0.0600	0.0490	0.0480	0.13111	0.1896	11.0764
0.0017	0.1270	0.0630	0.0520	0.0535	0.14222	0.1769	11.0764
0.0019	0.1330	0.0767	0.0530	0.0590	0.12511	0.1601	11.0764
0.0022	0.1390	0.0850	0.0530	0.0620	0.12000	0.1484	11.0764
0.0025	0.1420	0.0970	0.0560	0.0660	0.10000	0.1300	11.0764
0.0028	0.1480	0.1030	0.0670	0.0720	0.10000	0.1239	11.0764
0.0028	0.1540	0.1140	0.1030	0.1100	0.08889	0.1261	11.0764

Table A.10: Experimental data — Configuration 3 — Hs = 0.10 m, s = 0.02

Barrier properties: Dowel count n = 198, Hs = 0.10 m, b_0 = 0.010 m, Ls = 0.45 m, porosity = 0.9300, CA = 11.0764 m⁻¹

Q (m³/s)	H_1 (m)	H_2 (m)	H_3 (m)	H_4 (m)	Sf	n_obs	CA (m⁻¹)
0.0003	0.0450	0.0130	0.0090	0.0080	0.07111	0.1603	11.0764
0.0006	0.0700	0.0250	0.0150	0.0140	0.10000	0.1857	11.0764
0.0008	0.0870	0.0350	0.0210	0.0200	0.11556	0.1840	11.0764
0.0011	0.1040	0.0480	0.0250	0.0220	0.12444	0.1889	11.0764
0.0014	0.1140	0.0550	0.0290	0.0250	0.13111	0.1768	11.0764
0.0017	0.1220	0.0550	0.0330	0.0200	0.14889	0.1661	11.0764
0.0019	0.1300	0.0680	0.0350	0.0230	0.13778	0.1568	11.0764
0.0022	0.1350	0.0780	0.0400	0.0240	0.12667	0.1436	11.0764
0.0025	0.1400	0.0970	0.0480	0.0270	0.09556	0.1258	11.0764
0.0028	0.1440	0.1070	0.0480	0.0310	0.08222	0.1124	11.0764
0.0028	0.1440	0.1050	0.0920	0.1010	0.08667	0.1143	11.0764

Table A.11: Experimental data — Configuration 3 — Hs = 0.20 m, s = 0

Barrier properties: Dowel count n = 396, Hs = 0.20 m, b₀ = 0.010 m, Ls = 0.45 m, porosity = 0.9300, CA = 11.0764 m⁻¹

Q (m^3/s)	H_1 (m)	H_2 (m)	H_3 (m)	H_4 (m)	Sf	n_obs	CA (m^{-1})
0.0003	0.0440	0.0250	0.0250	0.0250	0.04222	0.1571	11.0764
0.0006	0.0690	0.0320	0.0320	0.0320	0.08222	0.1825	11.0764
0.0008	0.0880	0.0450	0.0400	0.0400	0.09556	0.1867	11.0764
0.0011	0.1040	0.0520	0.0450	0.0450	0.11556	0.1880	11.0764
0.0014	0.1180	0.0550	0.0480	0.0500	0.14000	0.1880	11.0764
0.0017	0.1300	0.0650	0.0540	0.0550	0.14444	0.1840	11.0764
0.0019	0.1420	0.0650	0.0580	0.0600	0.17111	0.1844	11.0764
0.0022	0.1560	0.0850	0.0620	0.0650	0.15778	0.1855	11.0764
0.0025	0.1680	0.0850	0.0670	0.0700	0.18444	0.1887	11.0764
0.0028	0.1790	0.0900	0.0690	0.0740	0.19778	0.1889	11.0764
0.0028	0.2360	0.2130	0.2160	0.2150	0.05111	0.1716	11.0764

Table A.12: Experimental data — Configuration 3 — Hs = 0.20 m, s = 0.02

Barrier properties: Dowel count n = 396, Hs = 0.20 m, b₀ = 0.010 m, Ls = 0.45 m, porosity = 0.9300, CA = 11.0764 m⁻¹

Q (m^3/s)	H_1 (m)	H_2 (m)	H_3 (m)	H_4 (m)	Sf	n_obs	CA (m^{-1})
0.0003	0.0370	0.0140	0.0100	0.0070	0.05111	0.1134	11.0764
0.0006	0.0600	0.0240	0.0170	0.0110	0.08000	0.1411	11.0764
0.0008	0.0800	0.0350	0.0220	0.0180	0.10000	0.1587	11.0764
0.0011	0.0950	0.0450	0.0290	0.0220	0.11111	0.1611	11.0764
0.0014	0.1150	0.0550	0.0370	0.0280	0.13333	0.1795	11.0764
0.0017	0.1250	0.0600	0.0400	0.0280	0.14444	0.1726	11.0764
0.0019	0.1380	0.0720	0.0440	0.0300	0.14667	0.1736	11.0764
0.0022	0.1500	0.0780	0.0490	0.0300	0.16000	0.1750	11.0764
0.0025	0.1650	0.0900	0.0550	0.0330	0.16667	0.1811	11.0764
0.0028	0.1790	0.1000	0.0580	0.0370	0.17556	0.1857	11.0764
0.0028	0.2300	0.2020	0.2150	0.2160	0.06222	0.1814	11.0764

Table A.13: Experimental data — Configuration 4 — Hs = 0.10 m, s = 0

Barrier properties: Dowel count n = 297, Hs = 0.10 m, b₀ = 0.010 m, Ls = 0.45 m, porosity = 0.8950, CA = 18.6403 m⁻¹

Q (m^3/s)	H_1 (m)	H_2 (m)	H_3 (m)	H_4 (m)	Sf	n_obs	CA (m^{-1})
0.0003	0.0490	0.0220	0.0220	0.0220	0.06000	0.1947	18.6403
0.0006	0.0750	0.0290	0.0310	0.0310	0.10222	0.2114	18.6403
0.0008	0.0930	0.0370	0.0380	0.0380	0.12444	0.2070	18.6403
0.0011	0.1080	0.0440	0.0440	0.0440	0.14222	0.2019	18.6403
0.0014	0.1170	0.0500	0.0500	0.0490	0.14889	0.1856	18.6403
0.0017	0.1250	0.0600	0.0540	0.0550	0.14444	0.1726	18.6403
0.0019	0.1300	0.0900	0.0550	0.0600	0.08889	0.1429	18.6403
0.0022	0.1350	0.0950	0.0600	0.0640	0.08889	0.1318	18.6403
0.0025	0.1400	0.0980	0.0550	0.0700	0.09333	0.1250	18.6403

Q (m³/s)	H_1 (m)	H_2 (m)	H_3 (m)	H_4 (m)	Sf	n_obs	CA (m⁻¹)
0.0028	0.1450	0.0980	0.0570	0.0760	0.10444	0.1219	18.6403
0.0028	0.1480	0.1100	0.1040	0.1110	0.08444	0.1176	18.6403

Table A.14: Experimental data — Configuration 4 — Hs = 0.10 m, s = 0.02

Barrier properties: Dowel count n = 297, Hs = 0.10 m, b_0 = 0.010 m, Ls = 0.45 m, porosity = 0.8950, CA = 18.6403 m^{-1}

Q (m³/s)	H_1 (m)	H_2 (m)	H_3 (m)	H_4 (m)	Sf	n_obs	CA (m⁻¹)
0.0003	0.0450	0.0170	0.0110	0.0100	0.06222	0.1645	18.6403
0.0006	0.0680	0.0270	0.0170	0.0150	0.09111	0.1773	18.6403
0.0008	0.0880	0.0320	0.0210	0.0200	0.12444	0.1870	18.6403
0.0011	0.1050	0.0470	0.0260	0.0230	0.12889	0.1922	18.6403
0.0014	0.1140	0.0520	0.0300	0.0270	0.13778	0.1773	18.6403
0.0017	0.1210	0.0600	0.0330	0.0280	0.13556	0.1628	18.6403
0.0019	0.1260	0.0650	0.0390	0.0280	0.13556	0.1490	18.6403
0.0022	0.1300	0.0960	0.0400	0.0300	0.07556	0.1190	18.6403
0.0025	0.1360	0.0970	0.0500	0.0320	0.08667	0.1174	18.6403
0.0028	0.1400	0.0950	0.0550	0.0340	0.10000	0.1147	18.6403
0.0028	0.1410	0.1010	0.0970	0.1100	0.08889	0.1119	18.6403

Table A.15: Experimental data — Configuration 4 — Hs = 0.20 m, s = 0

Barrier properties: Dowel count n = 594, Hs = 0.20 m, b_0 = 0.010 m, Ls = 0.45 m, porosity = 0.8950, CA = 18.6403 m^{-1}

Q (m³/s)	H_1 (m)	H_2 (m)	H_3 (m)	H_4 (m)	Sf	n_obs	CA (m⁻¹)
0.0003	0.0420	0.0180	0.0120	0.0120	0.05333	0.1455	18.6403
0.0006	0.0670	0.0230	0.0170	0.0170	0.09778	0.1710	18.6403
0.0008	0.0870	0.0350	0.0220	0.0200	0.11556	0.1840	18.6403
0.0011	0.1040	0.0440	0.0260	0.0250	0.13333	0.1891	18.6403
0.0014	0.1170	0.0450	0.0310	0.0290	0.16000	0.1854	18.6403
0.0017	0.1310	0.0560	0.0350	0.0330	0.16667	0.1879	18.6403
0.0019	0.1470	0.0650	0.0390	0.0340	0.18222	0.1957	18.6403
0.0022	0.1600	0.0650	0.0420	0.0340	0.21111	0.1979	18.6403
0.0025	0.1700	0.0800	0.0460	0.0360	0.20000	0.1938	18.6403
0.0028	0.1840	0.0870	0.0500	0.0400	0.21556	0.1989	18.6403
0.0028	0.2300	0.2080	0.2050	0.2050	0.04889	0.1633	18.6403

Table A.16: Experimental data — Configuration 4 — Hs = 0.20 m, s = 0.02

Barrier properties: Dowel count n = 594, Hs = 0.20 m, b_0 = 0.010 m, Ls = 0.45 m, porosity = 0.8950, CA = 18.6403 m^{-1}

Q (m³/s)	H_1 (m)	H_2 (m)	H_3 (m)	H_4 (m)	Sf	n_obs	CA (m⁻¹)
0.0003	0.0330	0.0120	0.0110	0.0120	0.04667	0.0906	18.6403
0.0006	0.0590	0.0230	0.0170	0.0170	0.08000	0.1366	18.6403
0.0008	0.0780	0.0350	0.0210	0.0200	0.09556	0.1517	18.6403
0.0011	0.0950	0.0420	0.0370	0.0190	0.11778	0.1614	18.6403

Q (m³/s)	H_1 (m)	H_2 (m)	H_3 (m)	H_4 (m)	Sf	n_obs	CA (m⁻¹)
0.0014	0.1160	0.0580	0.0330	0.0270	0.12889	0.1816	18.6403
0.0017	0.1280	0.0620	0.0350	0.0300	0.14667	0.1796	18.6403
0.0019	0.1400	0.0720	0.0390	0.0330	0.15111	0.1783	18.6403
0.0022	0.1530	0.0800	0.0430	0.0330	0.16222	0.1808	18.6403
0.0025	0.1670	0.0830	0.0450	0.0340	0.18667	0.1872	18.6403
0.0028	0.1800	0.0950	0.0510	0.0350	0.18889	0.1894	18.6403
0.0028	0.2240	0.2100	0.2130	0.2130	0.03111	0.1289	18.6403

Table A.17: Experimental data — Configuration 5 — Hs = 0.10 m, s = 0

Barrier properties: Dowel count n = 110, Hs = 0.10 m, b_0 = 0.010 m, Ls = 0.45 m, porosity = 0.9611, CA = 5.5753 m^{-1}

Q (m³/s)	H_1 (m)	H_2 (m)	H_3 (m)	H_4 (m)	Sf	n_obs	CA (m⁻¹)
0.0003	0.0300	0.0190	0.0220	0.0220	0.02444	0.0741	5.5753
0.0006	0.0480	0.0280	0.0310	0.0310	0.04444	0.0919	5.5753
0.0008	0.0620	0.0330	0.0390	0.0380	0.06444	0.0994	5.5753
0.0011	0.0720	0.0400	0.0460	0.0440	0.07111	0.0970	5.5753
0.0014	0.0870	0.0420	0.0510	0.0500	0.10000	0.1103	5.5753
0.0017	0.0950	0.0600	0.0570	0.0560	0.07778	0.1020	5.5753
0.0019	0.1060	0.0600	0.0620	0.0600	0.10222	0.1091	5.5753
0.0022	0.1150	0.0680	0.0650	0.0650	0.10444	0.1086	5.5753
0.0025	0.1210	0.0750	0.0690	0.0700	0.10222	0.1038	5.5753
0.0028	0.1260	0.0800	0.0700	0.0750	0.10222	0.0992	5.5753
0.0028	0.1360	0.1130	0.1150	0.1150	0.05111	0.0878	5.5753

Table A.18: Experimental data — Configuration 5 — Hs = 0.10 m, s = 0.02

Barrier properties: Dowel count n = 110, Hs = 0.10 m, b_0 = 0.010 m, Ls = 0.45 m, porosity = 0.9611, CA = 5.5753 m^{-1}

Q (m³/s)	H_1 (m)	H_2 (m)	H_3 (m)	H_4 (m)	Sf	n_obs	CA (m⁻¹)
0.0003	0.0280	0.0170	0.0120	0.0090	0.02444	0.0656	5.5753
0.0006	0.0450	0.0230	0.0160	0.0150	0.04889	0.0828	5.5753
0.0008	0.0550	0.0320	0.0210	0.0200	0.05111	0.0788	5.5753
0.0011	0.0700	0.0350	0.0270	0.0230	0.07778	0.0933	5.5753
0.0014	0.0800	0.0420	0.0300	0.0290	0.08444	0.0944	5.5753
0.0017	0.0900	0.0500	0.0350	0.0310	0.08889	0.0960	5.5753
0.0019	0.0960	0.0530	0.0390	0.0310	0.09556	0.0923	5.5753
0.0022	0.1060	0.0570	0.0430	0.0370	0.10889	0.0963	5.5753
0.0025	0.1150	0.0650	0.0440	0.0370	0.11111	0.0976	5.5753
0.0028	0.1220	0.0730	0.0540	0.0410	0.10889	0.0958	5.5753
0.0028	0.1250	0.1010	0.1050	0.1100	0.05333	0.0800	5.5753

Table A.19: Experimental data — Configuration 5 — Hs = 0.20 m, s = 0

Barrier properties: Dowel count n = 220, Hs = 0.20 m, b_0 = 0.010 m, Ls = 0.45 m, porosity = 0.9611, CA = 5.5753 m^{-1}

Q (m^3/s)	H_1 (m)	H_2 (m)	H_3 (m)	H_4 (m)	Sf	n_obs	CA (m^{-1})
0.0003	0.0320	0.0240	0.0240	0.0230	0.01778	0.0763	5.5753
0.0006	0.0490	0.0300	0.0310	0.0310	0.04222	0.0944	5.5753
0.0008	0.0620	0.0350	0.0390	0.0390	0.06000	0.0986	5.5753
0.0011	0.0740	0.0410	0.0450	0.0450	0.07333	0.1019	5.5753
0.0014	0.0860	0.0470	0.0520	0.0490	0.08667	0.1067	5.5753
0.0017	0.0970	0.0550	0.0560	0.0550	0.09333	0.1091	5.5753
0.0019	0.1050	0.0610	0.0590	0.0600	0.09778	0.1067	5.5753
0.0022	0.1150	0.0650	0.0620	0.0650	0.11111	0.1098	5.5753
0.0025	0.1230	0.0700	0.0640	0.0700	0.11778	0.1094	5.5753
0.0028	0.1320	0.0760	0.0680	0.0730	0.12444	0.1107	5.5753
0.0028	0.2230	0.2190	0.2180	0.2180	0.00889	0.0703	5.5753

Table A.20: Experimental data — Configuration 5 — Hs = 0.20 m, s = 0.02

Barrier properties: Dowel count n = 220, Hs = 0.20 m, b_0 = 0.010 m, Ls = 0.45 m, porosity = 0.9611, CA = 5.5753 m^{-1}

Q (m^3/s)	H_1 (m)	H_2 (m)	H_3 (m)	H_4 (m)	Sf	n_obs	CA (m^{-1})
0.0003	0.0300	0.0160	0.0130	0.0120	0.03111	0.0763	5.5753
0.0006	0.0450	0.0250	0.0180	0.0180	0.04444	0.0822	5.5753
0.0008	0.0560	0.0290	0.0240	0.0200	0.06000	0.0827	5.5753
0.0011	0.0700	0.0360	0.0280	0.0230	0.07556	0.0931	5.5753
0.0014	0.0790	0.0430	0.0330	0.0250	0.08000	0.0919	5.5753
0.0017	0.0900	0.0450	0.0380	0.0290	0.10000	0.0973	5.5753
0.0019	0.0980	0.0500	0.0410	0.0290	0.10667	0.0967	5.5753
0.0022	0.1070	0.0560	0.0440	0.0320	0.11333	0.0983	5.5753
0.0025	0.1180	0.0600	0.0500	0.0340	0.12889	0.1037	5.5753
0.0028	0.1250	0.0670	0.0530	0.0350	0.12889	0.1023	5.5753
0.0028	0.2110	0.2110	0.2110	0.2150	0.00000	0.0000	5.5753

Table A.21: Experimental data — Configuration 6 — Hs = 0.10 m, s = 0

Barrier properties: Dowel count n = 198, Hs = 0.10 m, b_0 = 0.010 m, Ls = 0.45 m, porosity = 0.9300, CA = 11.0764 m^{-1}

Q (m^3/s)	H_1 (m)	H_2 (m)	H_3 (m)	H_4 (m)	Sf	n_obs	CA (m^{-1})
0.0003	0.0460	0.0190	0.0210	0.0210	0.06000	0.1725	11.0764
0.0006	0.0640	0.0300	0.0290	0.0290	0.07556	0.1592	11.0764
0.0008	0.0820	0.0380	0.0360	0.0360	0.09778	0.1658	11.0764
0.0011	0.0990	0.0440	0.0420	0.0430	0.12222	0.1735	11.0764
0.0014	0.1080	0.0560	0.0480	0.0490	0.11556	0.1599	11.0764
0.0017	0.1170	0.0660	0.0580	0.0530	0.11333	0.1509	11.0764
0.0019	0.1240	0.0700	0.0580	0.0580	0.12000	0.1428	11.0764
0.0022	0.1290	0.0850	0.0590	0.0630	0.09778	0.1269	11.0764
0.0025	0.1340	0.0890	0.0620	0.0670	0.10000	0.1198	11.0764

Q (m³/s)	H_1 (m)	H_2 (m)	H_3 (m)	H_4 (m)	Sf	n_obs	CA (m⁻¹)
0.0028	0.1400	0.1040	0.0660	0.0760	0.08000	0.1072	11.0764
0.0028	0.1440	0.1000	0.1120	0.1100	0.09778	0.1185	11.0764

Table A.22: Experimental data — Configuration 6 — Hs = 0.10 m, s = 0.02

Barrier properties: Dowel count n = 198, Hs = 0.10 m, b_0 = 0.010 m, Ls = 0.45 m, porosity = 0.9300, CA = 11.0764 m⁻¹

Q (m³/s)	H_1 (m)	H_2 (m)	H_3 (m)	H_4 (m)	Sf	n_obs	CA (m⁻¹)
0.0003	0.0420	0.0160	0.0140	0.0120	0.05778	0.1445	11.0764
0.0006	0.0600	0.0250	0.0180	0.0160	0.07778	0.1413	11.0764
0.0008	0.0800	0.0340	0.0220	0.0220	0.10222	0.1587	11.0764
0.0011	0.0950	0.0420	0.0260	0.0250	0.11778	0.1614	11.0764
0.0014	0.1100	0.0550	0.0320	0.0290	0.12222	0.1657	11.0764
0.0017	0.1140	0.0590	0.0340	0.0300	0.12222	0.1463	11.0764
0.0019	0.1200	0.0650	0.0380	0.0340	0.12222	0.1361	11.0764
0.0022	0.1270	0.0740	0.0400	0.0300	0.11778	0.1292	11.0764
0.0025	0.1320	0.0950	0.0440	0.0320	0.08222	0.1109	11.0764
0.0028	0.1320	0.1010	0.0490	0.0370	0.06889	0.0942	11.0764
0.0028	0.1380	0.1040	0.1090	0.1080	0.07556	0.1032	11.0764

Table A.23: Experimental data — Configuration 6 — Hs = 0.20 m, s = 0

Barrier properties: Dowel count n = 396, Hs = 0.20 m, b_0 = 0.010 m, Ls = 0.45 m, porosity = 0.9300, CA = 11.0764 m⁻¹

Q (m³/s)	H_1 (m)	H_2 (m)	H_3 (m)	H_4 (m)	Sf	n_obs	CA (m⁻¹)
0.0003	0.0450	0.0250	0.0260	0.0250	0.04444	0.1643	11.0764
0.0006	0.0640	0.0340	0.0340	0.0330	0.06667	0.1579	11.0764
0.0008	0.0850	0.0420	0.0400	0.0390	0.09556	0.1761	11.0764
0.0011	0.0960	0.0480	0.0470	0.0450	0.10667	0.1635	11.0764
0.0014	0.1100	0.0560	0.0510	0.0500	0.12000	0.1654	11.0764
0.0017	0.1200	0.0600	0.0550	0.0560	0.13333	0.1604	11.0764
0.0019	0.1310	0.0680	0.0600	0.0600	0.14000	0.1591	11.0764
0.0022	0.1410	0.0750	0.0640	0.0640	0.14667	0.1571	11.0764
0.0025	0.1540	0.0850	0.0720	0.0700	0.15333	0.1610	11.0764
0.0028	0.1660	0.0930	0.0740	0.0740	0.16222	0.1637	11.0764
0.0028	0.2330	0.2140	0.2190	0.2180	0.04222	0.1552	11.0764

Table A.24: Experimental data — Configuration 6 — Hs = 0.20 m, s = 0.02

Barrier properties: Dowel count n = 396, Hs = 0.20 m, b_0 = 0.010 m, Ls = 0.45 m, porosity = 0.9300, CA = 11.0764 m⁻¹

Q (m³/s)	H_1 (m)	H_2 (m)	H_3 (m)	H_4 (m)	Sf	n_obs	CA (m⁻¹)
0.0003	0.0350	0.0160	0.0110	0.0090	0.04222	0.1030	11.0764
0.0006	0.0530	0.0200	0.0150	0.0150	0.07333	0.1118	11.0764
0.0008	0.0710	0.0260	0.0190	0.0210	0.10000	0.1272	11.0764
0.0011	0.0900	0.0380	0.0240	0.0260	0.11556	0.1467	11.0764

Q (m^3/s)	H_1 (m)	H_2 (m)	H_3 (m)	H_4 (m)	Sf	n_obs	CA (m^{-1})
0.0014	0.1020	0.0460	0.0280	0.0290	0.12444	0.1462	11.0764
0.0017	0.1140	0.0550	0.0320	0.0320	0.13111	0.1473	11.0764
0.0019	0.1250	0.0660	0.0370	0.0330	0.13111	0.1465	11.0764
0.0022	0.1350	0.0750	0.0400	0.0350	0.13333	0.1449	11.0764
0.0025	0.1450	0.0820	0.0430	0.0380	0.14000	0.1447	11.0764
0.0028	0.1560	0.0950	0.0460	0.0360	0.13556	0.1443	11.0764
0.0028	0.2220	0.2100	0.2130	0.2140	0.02667	0.1188	11.0764